AN EXPERIMENTAL AND NUMERICAL INVESTIGATION OF WARPAGE BEHAVIOR OF SILICON SUBSTRATES AT CRYOGENIC TEMPERATURES

A THESIS SUBMITTED TO
THE GRADUATE SCHOOL OF NATURAL AND APPLIED SCIENCES
OF
MIDDLE EAST TECHNICAL UNIVERSITY

EYÜP CAN BALOĞLU

IN PARTIAL FULFILLMENT OF THE REQUIREMENTS
FOR
THE DEGREE OF MASTER OF SCIENCE
IN
MECHANICAL ENGINEERING

SEPTEMBER 2016

Approval of the thesis:

AN EXPERIMENTAL AND NUMERICAL INVESTIGATION OF WARPAGE BEHAVIOR OF SILICON SUBSTRATES AT CRYOGENIC TEMPERATURES

submitted by **EYÜP CAN BALOĞLU** in partial fulfillment of the requirements for the degree of **Master of Science in Mechanical Engineering Department, Middle East Technical University** by,

Prof. Dr. Gülbin DURAL ÜNVER
Dean, Graduate School of **Natural and Applied Sciences** _____

Prof. Dr. Tuna BALKAN
Head of Department, **Mechanical Engineering** _____

Assoc. Prof. Dr. Tuba OKUTUCU ÖZYURT
Supervisor, **Mechanical Engineering Department, METU** _____

Prof. Dr. Zafer DURSUNKAYA
Co-supervisor, **Mechanical Engineering Department, METU** _____

Examining Committee Members:

Prof. Dr. Serkan DAĞ
Mechanical Engineering Department, METU _____

Assoc. Prof. Dr. Tuba OKUTUCU ÖZYURT
Mechanical Engineering Department, METU _____

Prof. Dr. Zafer DURSUNKAYA
Mechanical Engineering Department, METU _____

Asst. Prof. Dr. Özgür BAYER
Mechanical Engineering Department, METU _____

Assoc. Prof. Dr. Ali BOZBEY
Electrical and Electronics Engineering Department, TOBB ETÜ _____

Date: _____

I hereby declare that all information in this document has been obtained and presented in accordance with academic rules and ethical conduct. I also declare that, as required by these rules and conduct, I have fully cited and referenced all material and results that are not original to this work.

Name, Last Name: EYÜP CAN BALOĞLU

Signature :

ABSTRACT

AN EXPERIMENTAL AND NUMERICAL INVESTIGATION OF WARPAGE BEHAVIOR OF SILICON SUBSTRATES AT CRYOGENIC TEMPERATURES

BALOĞLU, Eyüp Can
M.S., Department of Mechanical Engineering
Supervisor : Assoc. Prof. Dr. Tuba OKUTUCU ÖZYURT
Co-Supervisor : Prof. Dr. Zafer DURSUNKAYA

September 2016, 109 pages

Surface deformations and thermal stress behavior of microelectronic devices that operate at cryogenic temperatures (less than 120 K) and under vacuum conditions are important phenomena that affect the reliability requirements of such components. Excessive deformation and thermal stress on these devices may result in interconnect failure, performance degradation or other direct mechanical failure of one or more components. To obtain reliable products, surface deformations, named as warpage most widely, and thermal stresses should be optimized. The sources of the warpage and thermal stresses are large differences between the operation and storage temperatures of such devices, and the existence of thermal mismatch caused by materials having different thermal expansion coefficients. In this study, an experimental setup is utilized to measure out of plane surface deformations of integrated assemblies at cryogenic temperatures as well as at room temperature. The test setup is equipped with a phase shifting Fizeau laser interferometer system. To reach cryogenic temperatures liquid nitrogen is used. Four different measurement error sources are defined and con-

tribution of each source is determined by experimental methods, analytical solutions or by using finite element analysis. Optical path change due to the difference between optical window temperatures at the initial and final states causes 61.3 nm difference. Natural surface topology of optical window (BK7) changes the peak to valley (PV) difference value of a sample by an amount of 27.2 nm. The effect of optical window tilt angle on PV is determined as 30 nm by testing the same sample at three different optical window tilt angles. Finally the PV difference of a sample caused by the deflection of the optical window related to pressure difference on top and bottom surfaces is determined as 15 nm. According to the results of a parametric finite element analysis on a ceramic-epoxy-silicon trimaterial assembly, a minimum warpage with a value of 0.13 μm exists for layer thicknesses of 1.27 mm ceramic, 0.075 mm epoxy and 0.1 mm silicon due to a temperature change between room temperature and 80 K whereas a maximum warpage of 20.60 μm exists for layer thicknesses of 0.63 mm ceramic, 0.5 mm epoxy and 0.1 mm silicon. Moreover, it is observed that increasing the ceramic thickness or decreasing the silicon thickness by keeping other layer thicknesses constant decreases the warpage. A total number of eight samples with different ceramic and silicon thicknesses are experimentally studied. In some cases, a whole field fringe formation is not observed for the silicon surface because of excessive deformation of the sample. In these cases, a spherical bending is assumed and the radius of curvature value of the sample is determined at 80 K. An extrapolation of observed results is used to determine 80 K warpage value of such samples. The remaining sample results can be obtained directly from measurements. For the integrated structure that contains 0.1 mm thick silicon, successful warpage measurement could not be obtained even at room temperature due to excessive deformation of the sample. For all of the remaining seven cases, the difference between the finite element analysis and experimental results is within 12.0%.

Keywords: Warpage measurements, cryogenic applications, phase shifting Fizeau laser interferometer, trimaterial assembly

ÖZ

KRİYOJENİK SICAKLIKLARDA SİLİSYUM ALTTAŞ YÜZEY BÜKÜLME DAVRANIŞLARININ DENEYSEL VE SAYISAL İNCELENMESİ

BALOĞLU, Eyüp Can
Yüksek Lisans, Makina Mühendisliği Bölümü
Tez Yöneticisi : Assoc. Prof. Dr. Tuba OKUTUCU ÖZYURT
Ortak Tez Yöneticisi : Prof. Dr. Zafer DURSUNKAYA

Eylül 2016 , 109 sayfa

Kriyojenik sıcaklıklarda (120 K'den daha düşük) ve vakum altında çalışan mikroelektronik aygıtların yüzey bükülme ve ısıl gerilim davranışları aygıt güvenilirliğinin sağlanmasında önemli parametrelerdir. Cihaz bileşenleri üzerinde oluşan aşırı yüzey bükülmeleri ve yüksek ısıl gerilimler, bağlantı arayüzlerinde bozulmaya, performans düşüşüne ya da yapı üzerinde direkt mekanik bozulmaya yol açabilir. Güvenilir ürünler elde edebilmek için genellikle "warpage" olarak adlandırılan yüzey bükülmeleri ve ısıl gerilimler optimize edilmelidir. Bu aygıtların operasyon ve depolama durumları arasındaki büyük sıcaklık farkları ve kullanılan farklı ısıl genleşme katsayısına sahip malzemelerin yarattığı ısıl genleşme uyumsuzluğu yüzey bükülmelerinin ve ısıl gerilimlerin ana kaynağıdır. Bu çalışma ile entegre malzeme yapıları üzerinde oluşan düzlem dışı bükülmeleri hem kriyojenik sıcaklıklarda hem de oda sıcaklığında ölçebilecek bir test düzeneği hazırlanmıştır. Bu düzenekte faz değiştiricili Fizeau lazer interferometre sistemi kullanılmıştır. Kriyojenik sıcaklıklara erişebilmek için test düzeneğinde sıvı azot

kullanılmaktadır. Dört farklı ölçüm hatası kaynağı belirlenmiş ve her kaynağın etkisi deneysel yöntemlerle, analitik çözümlerle ya da sonlu elemanlar analizi yöntemiyle belirlenmiştir. Bu sonuçlara göre, optik pencerenin ilk ve son sıcaklıkları arasındaki fark yüzünden değişen optik yolun neden olduğu hata 61,3 nm olarak belirlenmiştir. Optik pencerenin (BK7) yüzey topolojisinden kaynaklı olarak doruk koyak değeri (PV) 27,2 nm değişkenlik göstermiştir. Optik pencerenin eğiklik açısının etkisi ise üç farklı açıda optik pencere kullanılarak test edilmiş ve doruk koyak değerinde 30 nm farklılık tespit edilmiştir. Son olarak alt ve üst yüzeylerinde oluşan basınç farklılığı nedeniyle deforme olan optik pencerenin neden olduğu hata 15 nm olarak belirlenmiştir. Seramik-epoksi-silisyum üç katmanlı entegre yapı üzerinde gerçekleştirilen parametrik sonlu elemanlar analizi sonuçlarına göre 0,13 μm'lik minimum yüzey bükülmesi 1,27 mm seramik, 0,075 mm epoksi ve 0,1 mm silisyum malzeme kalınlıkları için elde edilmiştir. Maksimum yüzey bükülmesi ise 20,63 μm değerinde olup 0,63 mm seramik, 0,5 mm epoksi ve 0,1 mm silisyum malzemeleri için gerçekleşmiştir. Diğer katman kalınlıklarını sabit tutmak şartı ile artan seramik kalınlığı ve azalan silisyum kalınlığının yüzey bükülme değerini azalttığı gözlemlenmiştir. Farklı seramik ve silisyum kalınlıklarında toplam sekiz örnek deneysel olarak test edilmiştir. Bazı örneklerde yüksek deformasyona bağlı olarak tüm silisyum yüzeyi için girişim deseni oluşmadığı gözlemlenmiştir. Bu durumda bulunan örnekler için küresel bükülmenin geçerli olduğu kabul edilmiş ve 80 K sıcaklığında eğrilik yarıçapı ölçülerek tüm örneğin yüzey bükülme değeri hesaplanmıştır. Geri kalan tüm örnekler için direkt ölçüm sonuçları alınabilmiştir. Silisyum malzeme kalınlığının 0,1 mm olduğu test örneğinde oda sıcaklığında dahi yüzey bükülme değeri yüksek deformasyon nedeniyle ölçülememiştir. Geri kalan yedi örnek için sonlu elemanlar analizi ve deneysel sonuçlar arasındaki hata değeri %12'yi geçmemiştir.

Anahtar Kelimeler: Yüzey bükülmesi ölçümleri, kriyojenik uygulamalar, faz değiştiricili Fizeau lazer interferometre, üç katmanlı entegre yapı



ad

ACKNOWLEDGMENTS

First and foremost, I would like express my sincerest grattitude to my advisor Assoc. Prof. Tuba Okutucu Özyurt and my co-advisor Prof. Zafer Dursunkaya who have supported me throughout this master of science study and research with their patience, motivation and vast knowledge. Without their collaborate, encouragement and effort, this thesis would not have been completed or written. I am also thankful to my advisor and co-advisor for providing the invaluable graduate school experience by demanding new ideas and high quality of work.

I also would like to thank the rest of my thesis committee: Prof. Serkan Dağ, Asst. Prof. Özgür Bayer and Assoc. Prof. Ali Bozbey, for their time and invaluable comments.

I am deeply thankful to Aselsan Inc. for their equipment and facility support in experimental studies. I am also grateful to Serkan Karaca and Erkin Utku Turgut for the preparation of measurement lab and contributions during sample measurements.

I must also acknowledge Cemile Duygu Öztürk Selçuk, Esin Akça, Dr. Hasan Çakmak, İsmail Soyalp and Seçkin Cimbar for their patience and endless effort for sample processing. Without their effort, this study would not be completed. Additionally, I would like to thank my colleagues Burkan Kaplan, Dr. Çağla Akgün and managers Ümid Tümkaya and Dr. Selçuk Özer for their endless support and worthwhile technical comments and suggestions.

Last but not the least, I would like to thank my family: my parents Sultan and Ali İhsan, my grandmother Nazlı for supporting me spiritually throughout this study and my life.

TABLE OF CONTENTS

ABSTRACT v

ÖZ vii

ACKNOWLEDGMENTS x

TABLE OF CONTENTS xi

LIST OF TABLES xv

LIST OF FIGURES xvii

LIST OF ABBREVIATIONS xxii

CHAPTERS

1 INTRODUCTION 1

1.1 Introduction 1

1.2 Literature Review 8

1.2.1 Analytical Solutions for Warpage and Thermal Stress in Electronic Packaging 8

1.2.2 Warpage and Thermal Stress Predictions on Cooled IR Sensors 14

1.2.3 Interferometer Equipped Warpage Measurements in Electronic Packaging 22

1.3 Analytical Model vs Finite Element Model 31

1.4 Objective of Thesis 33

1.5 Outline 34

2 FINITE ELEMENT ANALYSIS 35

2.1 Finite Element Model 35

2.2 Meshing: Solid 186 Element vs Solid 187 Element 36

2.2.1 Solid 186 element 37

2.2.1.1 Epoxy element size 38

2.2.1.2 Ceramic and silicon element size 39

2.2.2 Solid 187 element 39

2.2.2.1 Epoxy element size 40

2.2.2.2 Ceramic and silicon element size 40

2.3 Parametric Analysis 42

2.3.1 0.5 mm silicon thickness 43

2.3.2 0.4 mm silicon thickness 45

2.3.3 0.3 mm silicon thickness 47

2.3.4 0.2 mm silicon thickness 47

2.3.5 0.1 mm silicon thickness 49

3 TEST SETUP 55

3.1 Test Method 55

3.2 Test Setup Design 57

3.2.1 First Design of Test Setup 57

3.2.2 Second Design of Test Setup 59

3.2.3 Measurement Error Sources 61

3.2.3.1 Effect of change in optical path, (Effect 1) 61

3.2.3.2 Effect of surface topology of optical window, (Effect 2) 65

3.2.3.3 Effect of optical window tilt angle, (Effect 3) 67

3.2.3.4 Effect of different pressures on top and bottom surfaces of optical window, (Effect 4) 68

3.2.3.5 Overall assessment of measurement error sources 69

4 EXPERIMENTAL STUDIES 75

4.1 Experimental Procedure 75

4.1.1 Preparation of trimaterial assembly 75

4.1.2 Construction of the test setup 77

4.2 Measured Samples and Warpage Results 79

4.2.1 Measurements on Sample 1 80

4.2.2 Measurements on Sample 2 82

4.2.3 Measurements on Sample 3 82

4.2.4 Measurements on Sample 4 85

4.2.5 Measurements on Sample 5 88

4.2.6 Measurements on Sample 6 91

4.2.7 Measurements on Sample 7 92

4.2.8 Measurements on Sample 8 93

4.2.9 Comparison of warpage measurements 96

4.3 Grinding Effect on Warpage 96

4.4 Comparison of Numerical and Experimental Results 97

5 CONCLUSIONS AND FUTURE WORK 103

5.1 Summary and Conclusions 103

5.2 Recommendations for Future Work 105

REFERENCES 107

APPENDICES

LIST OF TABLES

TABLES

Table 1.1 Infrared radiation spectrum 1

Table 1.2 Applications of IR imaging systems 4

Table 1.3 Cryocooled vs Uncooled Microbolometer Imagers 4

Table 1.4 von Mises stress for different substrate thicknesses [1] 16

Table 1.5 Thermal stresses by adding different cushions [2] 17

Table 1.6 Material properties of die-substrate assembly 31

Table 2.1 Material properties 36

Table 2.2 Highest and lowest warpage cases of 0.5 mm thick silicon 44

Table 2.3 Highest and lowest warpage cases of 0.4 mm thick silicon 45

Table 2.4 Highest and lowest warpage cases of 0.3 mm thick silicon 47

Table 2.5 Highest and lowest warpage cases of 0.2 mm thick silicon 48

Table 2.6 Highest and lowest warpage cases of 0.1 mm thick silicon 49

Table 3.1 PV values for different orientations of the optical window 67

Table 3.2 PV results for different tilt angles of optical flat 67

Table 3.3 Error contributions of each effect for the two setup designs 72

Table 4.1 Sample dimensions in mm 79

Table 4.2 Experimental warpage results 96

Table 4.3 Updated FEA results 98

Table 4.4 Revised FEM results versus experimental results 98

Table 4.5 Equivalent maximum stress on the silicon 101

LIST OF FIGURES

FIGURES

Figure 1.1 Reflected radiation vs self radiation 2

Figure 1.2 Infrared imaging scheme 3

Figure 1.3 Vacuum envelope structure 5

Figure 1.4 Representative FPA structure of an infrared sensor 7

Figure 1.5 Themostat components 9

Figure 1.6 Cross sectional view 10

Figure 1.7 Flip chip ball grid array (FCBGA) 12

Figure 1.8 FCBGA assembly 12

Figure 1.9 Quarter of the package [3] 13

Figure 1.10 Representative structure of IRFPA 15

Figure 1.11 Long linear MCT array structure 16

Figure 1.12 FEM results for different thicknesses of ceramic board 17

Figure 1.13 InSb FPA structure analyzed in [4] 18

Figure 1.14 Crack types on InSb FPA (adopted from [4]) 18

Figure 1.15 Indirect integration of IRFPA 21

Figure 1.16 The distance, *d*, between the silicon ROIC and the sensor chip . . 21

Figure 1.17 Fizeau laser interferometer 23

Figure 1.18 Michelson interferometer 24

Figure 1.19 Twyman Green interferometer 25

Figure 1.20 Shadow Moiré interferometer 26

Figure 1.21 Package structure 27

Figure 1.22 Representative outline of flip chip package 28

Figure 1.23 Cold region of vacuum envelope 29

Figure 1.24 Silicon epoxy silicon integrated structure in liquid nitrogen bath . . 30

Figure 1.25 Die substrate assembly 31

Figure 1.26 Die thickness versus effective warpage 32

Figure 1.27 Substrate thickness versus effective warpage 32

Figure 2.1 Analyzed three materials of cold region 35

Figure 2.2 Defined supports in FEA 37

Figure 2.3 Representative deformed trimaterial assembly 37

Figure 2.4 Epoxy mesh size effect with Hex 20 elements 38

Figure 2.5 Ceramic and silicon mesh size effect with Hex 20 elements 39

Figure 2.6 Epoxy mesh size effect with Tet 10 elements 40

Figure 2.7 Ceramic and silicon mesh size effect with Tet 10 elements 41

Figure 2.8 Comparison of Solid 186 and Solid 187 elements in epoxy meshing . 41

Figure 2.9 Comparison of Solid 186 and Solid 187 elements in ceramic and silicon meshing 42

Figure 2.10 Definition of warpage [5] 43

Figure 2.11 Warpage behavior of silicon, $t_{silicon}$ = 0.5 mm 43

Figure 2.12 The effect of epoxy layer thickness on warpage of silicon, $t_{silicon} = 0.4$ mm 45

Figure 2.13 Warpage behavior of silicon, $t_{silicon}$ = 0.4 mm 46

Figure 2.14 Warpage behavior of silicon, $t_{silicon}$ = 0.3 mm 48

Figure 2.15 Warpage behavior of silicon, $t_{silicon} = 0.2$ mm 49

Figure 2.16 Warpage behavior of silicon, $t_{silicon} = 0.1$ mm 50

Figure 2.17 Critical thickness ratio, $TR = \frac{t_{ceramic}}{t_{silicon}}$ 51

Figure 2.18 A closer look for critical thickness ratio, $TR = \frac{t_{ceramic}}{t_{silicon}}$ 52

Figure 2.19 The effect of the silicon thickness on warpage 53

Figure 3.1 Representation of warpage 56

Figure 3.2 Phase shifting Fizeau laser interferometer system 56

Figure 3.3 Fringe pattern 57

Figure 3.4 First design of the test setup 58

Figure 3.5 Second design of the test setup 60

Figure 3.6 Test setup 60

Figure 3.7 Simplified model of test setup 1 62

Figure 3.8 Boundary conditions for the first design 63

Figure 3.9 Optical window temperature distribution for the first test setup . . 64

Figure 3.10 BK7 mesh sensitivity of temperature output 65

Figure 3.11 Test structure for testing optical window effect,top view 66

Figure 3.12 Test structure for testing optical window effect,side view 66

Figure 3.13 Optical window positions 67

Figure 3.14 Warpage characteristics of different orientations of optical window . 68

Figure 3.15 Pressure difference on optical window 69

Figure 3.16 Simplified model of test setup 2 70

Figure 3.17 Boundary conditions for the second design of test setup 71

Figure 3.18 Temperature distribution on optical window for the second design . 71

Figure 4.1 Removing of epoxy bubbles in a vacuum chamber 76

Figure 4.2 Cleaning of individual components 77

Figure 4.3 Final cleaning of silicon surface and BK7 glass 78

Figure 4.4 Test chamber and providing vacuum environment 79

Figure 4.5 Warpage measurement result at room temperature for $t_{\text{silicon}} = 0.1$ mm 80

Figure 4.6 Diagonal dicing of the sample and cross sectional view 81

Figure 4.7 SEM images of Sample 1 81

Figure 4.8 Warpage of silicon at room temperature for Sample 2 82

Figure 4.9 Temperature dependent PV values for Sample 2 83

Figure 4.10 SEM images of Sample 2 83

Figure 4.11 Warpage of silicon at room temperature for Sample 3 84

Figure 4.12 Temperature dependent PV values for Sample 3 84

Figure 4.13 SEM images of Sample 3 85

Figure 4.14 Warpage of silicon at room temperature for Sample 4 85

Figure 4.15 Temperature dependent fringe structures on Sample 4 86

Figure 4.16 Fringe pattern of the objective lens that has 2350 mm radius of curvature 87

Figure 4.17 Surface topology and radius of curvature data taken from a limited portion of Sample 4 at 80 K 88

Figure 4.18 Temperature dependent PV values for Sample 4 88

Figure 4.19 SEM images of Sample 4 89

Figure 4.20 Warpage of silicon at room temperature for Sample 5 89

Figure 4.21 Temperature dependent fringe structures on Sample 5 90

Figure 4.22 Surface topology and radius of curvature data taken from a limited portion of Sample 5 at 80 K 90

Figure 4.23 Temperature dependent PV values for Sample 5 91

Figure 4.24 Temperature dependent fringe structures on Sample 6 91

Figure 4.25 Warpage of silicon at room temperature for Sample 6 92

Figure 4.26 Warpage of silicon at room temperature for Sample 7 93

Figure 4.27 Warpage of silicon at 80 K for Sample 7 93

Figure 4.28 Warpage of silicon at room temperature for Sample 8 94

Figure 4.29 Temperature dependent fringe structures on Sample 8 94

Figure 4.30 Temperature dependent PV values of Sample 8 95

Figure 4.31 Ungrinded silicon surface topology at room temperature 97

Figure 4.32 Grinded samples with measured warpage values at room temperature 97

Figure 4.33 Warpage results of Samples 2, 3, 4, 5 99

Figure 4.34 Warpage results for $t_{\text{silicon}} = 0.5$ mm, Samples 5, 6 and 8 101

LIST OF ABBREVIATIONS

IR	Infrared
NIR	Near Infrared
SWIR	Short Wavelength Infrared
MWIR	Mid Wavelength Infrared
LWIR	Long Wavelength Infrared
FIR	Far Infrared
NETD	Noise Equivalent Temperature Difference
FPA	Focal Plane Array
ROIC	Readout Integrated Circuit
BGA	Ball Grid Array
FCBGA	Flip Chip Ball Grid Array
IRFPA	Infrared Focal Plane Array
MCT	Mercury Cadmium Telluride, HgCdTe
FEA	Finite Element Analysis
FEM	Finite Element Method
BK7	Borosilicate Glass
PV	Peak to Valley
OPD	Optical Path Difference
OPL	Optical Path Length
PCB	Printed Circuit Board
MTTF	Mean Time To Failure
u	Longitudinal displacement
α	Coefficient of thermal expansion / illuminaton angle
υ	Poisson's ratio
E	Elastic modulus
$q(x)$	Shearing force per unit length
M	Bending moment
D	Flexural rigidity

ρ	Radius of curvature
τ	Shear stress
σ	Normal stress
n	Refractive index

CHAPTER 1

INTRODUCTION

1.1 Introduction

Infrared-imaging systems are often used to observe objects in poor visibility (foggy or snowy) or nighttime conditions. There are civil, military, scientific and industrial applications of infrared imaging systems. The spectral region of infrared radiation covers wavelengths in the range from 0.75 μm to 1000 μm.

Table1.1: Infrared radiation spectrum

Division Name	**Abbreviation**	**Wavelength [μm]**
Near Infrared	NIR	0.75 – 1.40
Short-wavelength Infrared	SWIR	1.4 – 3.0
Mid-wavelength Infrared	MWIR	3.0 – 8.0
Long-wavelength Infrared	LWIR	8.0 – 15.0
Far Infrared	FIR	15.0 – 1000

Infrared sensors detect the radiation which is coming from an observed object. This radiation is not the reflected radiation from the sun or any other source. It is the radiation caused by observed object itself as seen in Figure 1.1 which is called the self-radiation. All of the objects which have a temperature above 0 K (absolute zero) have self radiation. The self-radiation is dependent on temperature and surface characteristics of the object. To display an infrared image, equipments should work in coherence with the sensor. A representative schematic is given in Figure 1.2. According to Figure 1.2, a special lens or lens system focuses the incoming infrared light from all of the targets in view. Focused infrared light generates electrical signals on the detection layer of the infrared sensor. The electrical signals should be processed

via a signal processing unit to display the data. There exist two types of infrared

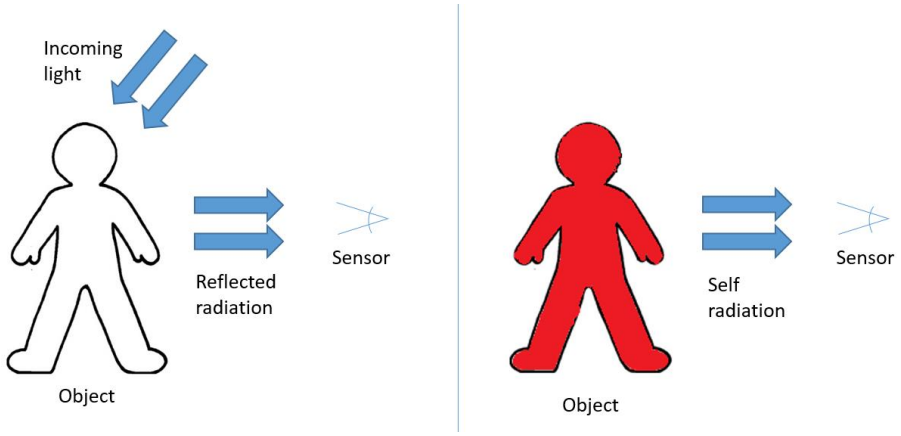

Figure 1.1: Reflected radiation vs self radiation

sensors which are thermal detectors and photon detectors. Both of these devices take incoming infrared radiation as an input. However, their responsivity for incoming radiation is different. For thermal detectors, the incident radiation causes a temperature change (heating) which results in change of mechanical and electrical properties of the detection material. In a thermal detector, changes in these properties are measured by an external circuit. Thermal detectors' response rate is slow, because there is a finite time needed for the incoming radiation to heat up the detection layer. After that, the external circuit can detect the material property changes. Bolometer, thermopile and pyroelectric sensors are few examples of thermal detectors [6]. Incoming photons cause moving electrons in the detection layer for photon detectors. The moving electrons change electrical properties of detection layer which is measured by an external circuit. Because time required for the existence of moving electrons is short, the response rate of photon detectors are fast. Moreover there is no need to heat up the detection layer. According to their operating temperatures, infrared sensors can be divided into two categories as cooled sensors and uncooled sensors, both of which should operate under high vacuum conditions.

Uncooled sensors can operate around room temperature whereas cooled sensors must operate at cryogenic temperatures. As a part of physics, cryogenics deals with obtaining lower temperatures than room temperature ($<$ 120 K) and measuring these temperatures [7]. When an infrared sensor is cooled to cryogenic temperatures, there

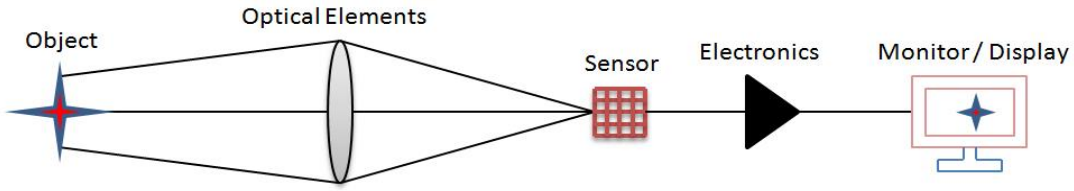

Figure 1.2: Infrared imaging scheme

exists a great temperature difference between the observed object and the sensor which increases sensor sensitivity. HgCdTe (MCT), GaAs, InSb materials are the most commonly used materials in the detection layer of cooled infrared sensors. Different types of cryocoolers [8] [9] are used to achieve cryogenic temperatures. There are some drawbacks for cooled infrared sensors. For example, a long cooldown time (more than a few minutes) is required to reach the operation condition. Large power consumption and low mean time to failure (MTTF) are other drawbacks which are mainly caused by cryocooler's requirements and limits. Generally, MTTF for a cryocooler is on the order of a few thousand hours. In spite of these drawbacks, cooled infrared sensors are used when high performance is required. Uncooled sensors, on the contrary, do not have to be cooled to cryogenic temperatures. Thermo-electric coolers are commonly used to obtain temperature stabilization. For uncooled sensors, a low power consumption is required. Moreover, they have smaller physical dimensions and are lighter than cooled sensors. These advantages of uncooled sensors make them the first option for hand-held cameras or mobile device applications. Uncooled sensors such as microbolometers cannot be used in multispectrum of high speed infrared applications. Furthermore, the resolution of the uncooled microbolometers has not been able to match cooled sensors'. Uncooled sensors have generally higher noise than cooled semiconductor sensors.

There exists various application areas for IR sensors such as atmosphere and space, military, medical and industrial applications. Some of these applications are given in Table 1.2. In addition to these, there are many other application areas of IR sensors in daily life, e.g. infrared security cameras in airports and parking sensors in automotive industry. In Table 1.3, a brief comparison is given for cryocooled IR sensors and uncooled microbolometer detectors. The detection layer material is different for the

two cases. Moreover noise equivalent temperature difference (NETD) value is smaller in cooled sensors. Simply, NETD indicates the sensitivity of the detector for thermal radiation. It defines the amount of radiation which produces an output signal equal to internal system noise. NETD is approximately given as 50—200 mK for uncooled microbolometers whereas 5-–25mK for cooled MCT sensors [10].

Table1.2: Applications of IR imaging systems

Scientific	**Military**	**Medical**	**Industry**
Satellite earth observation	Night vision devices	Early detection and	Petroleum exploration
Space telescopes	Search - Track	determination of cancer	Gas analyzing
Convective storm detection	Missile guidance	Determination of blood	Rail safety
Infrared Astronomy	Artillery control systems	vessel blockage	Moisture analyzing

Table1.3: Cryocooled vs Uncooled Microbolometer Imagers

	Cryocooled Imager	**Uncooled Microbolometer Imager**
Typical detector temperature	100 K	Room temperature
Sensor material	MCT, InSb, GaAs/AlGaAs	a-Silicon, VOx, YBaCuO
Typical NETD	10 mK	50 mK
Applications	Military and industry applications	Military, scientific, medical and industry applications

Cooled sensors such as MCT, InSb or GaAs/AlGaAs have to operate at cryogenic temperatures. Cryocooling of the sensor improves signal to noise ratio. In this way, the detectability of the objects with slight temperature differences increases. If this type of sensors would not be cooled during operation, the sensor would be probably flooded by its own radiation or it could detect only the objects which are significantly warmer than itself.

Cooled sensor structure will be briefly explained to have a better understanding of the problem that will be mentioned in Chapter 2.

Operating temperature of the cooled sensors is close to liquid nitrogen temperature, 77K. Some detector materials like GaAs/AlGaAs should operate at lower temperatures. On the other hand, there exist some other applications of MCT detectors for which the operating temperature is around 100K. When lower operating temperatures are desired, physical dimensions and power consumption of cryocooler may signifi-

cantly increase. To reach cryogenic temperatures with the minimum cooling power, all of possible heat losses must be minimized during the design phase. A high vacuum environment (10^{-6} to 10^{-9} Torr) is generally provided for cryocooled structures. This way, the convection mode of heat transfer is eliminated. Moreover, radiation and conduction losses should also be taken into account while designing the vacuum envelope structures of infrared sensors which is named as dewar.

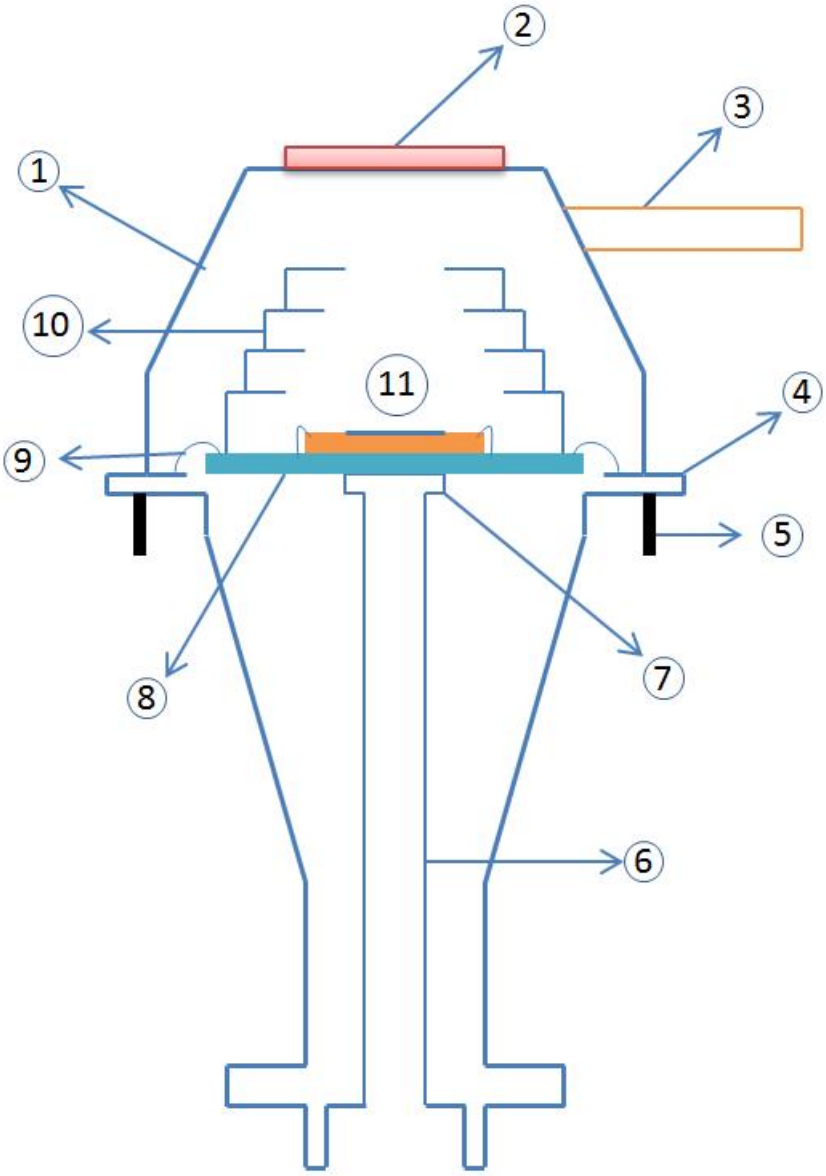

Figure 1.3: Vacuum envelope structure

In Figure 1.3, the main components of a vacuum envelope are given. Definitions of the individual components are as follows:

1. Dewar outer body is composed of metal materials. Different metals can be used for the outer body. Inner surface of this structure stands under high vacuum conditions whereas outer surface of it is at atmospheric pressure.

2. Optical window is the first component on vacuum envelope structure that encounters infrared radiation. The optical window should have high transmittance for the desired wavelength.

3. Vacuum port stands on the dewar outer body. It is used for pumping out the gas inside dewar and this tube should be closed without breaking inside vacuum for operation.

4. Electrical connection ceramic has electrical connection pads on it which are used to transmit electrical signals from vacuum environment to outer world.

5. Pins or connectors are used to transmit electrical signals from the vacuum envelope module to the next module. They form electrical interface of the dewar structure.

6. Cold finger is a hollow cylinder which is an interface component between the vacuum envelope and the cryocooler. The wall thickness of this tube is very effective on conduction losses of the vacuum envelope.

7. Cap is another metal part that is integrated with the cold finger. The same or similar materials for the cold finger may be used as a cap material.

8. Carrier ceramic is a ceramic component. Infrared sensor is placed on top of it. On the carrier ceramic, there exists electrical connection pad which transfers electrical signal in radial direction through the electrical connection ceramic.

9. Wirebond is a way of making interconnection between carrier ceramic and electrical ceramic. They are also used between the sensor and the carrier ceramic. Wire diameters are in the order of tens of micrometers for infrared applications. Gold, silver, aluminum and copper can be used as wirebond materials.

10. Cold shield is an important equipment to protect the sensor from undesired IR radiations that are coming from outside of optical field of view. It has key surface properties such as low emissivity and high reflectivity.

11. Sensor can be defined as a hybrid structure that is composed of an active detection layer which is made of a semiconductor material for cooled IR sensors and an external circuit which is used to detect incoming electrical signals from detection layer. This external circuit is named as readout integrated circuit (ROIC).

Another important term Focal Plane Array (FPA) should also be defined in the light of sensor definition. A common definition for FPA (also named as starring array of focal plane) is an image sensing device which consists of two dimensional rectangular arrays. The arrays are composed of infrared sensing pixels which are located at the focus plane of a lens in the imaging system. For infrared sensors, the construction material of infrared light sensing pixels cannot be used to measure or transmit output signal of each pixel. To perform these functions, the detection layer is hybridized with ROIC via flip chip bumps which are commonly made of indium material. For infrared sensors, this hybridized structure assembly is called as FPA. A representative structure of FPA is given in Figure 1.4.

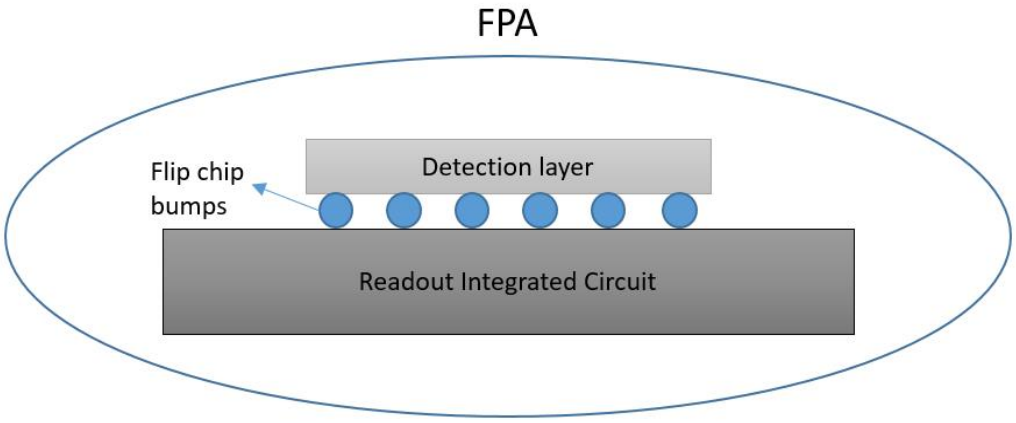

Figure 1.4: Representative FPA structure of an infrared sensor

The structure given in Figure 1.4 represents not only a part of the hybridized infrared sensor structure but also a generic electronic package in which flip chip bonding is used to integrate chip and substrate. Although the different operation conditions should be satisfied for each structure, mechanically similar geometries exist for infrared sensor structure as well as a generic electronic flip chip package. With the changing temperature on the device and existence of different materials such as epoxy, ceramic or semiconductor materials, which are integrated on each other, thermal stress and surface

deformations may arise on the chip or sensor as well as on the other subcomponents. This problem may affect the reliability or performance of the device. Hence, these two structural phenomena must be controlled during the design phase. In the next section, the literature search on three different subsections all of which are related to surface deformation predictions and measurements on a electronic package and on an infrared sensor is provided.

1.2 Literature Review

1.2.1 Analytical Solutions for Warpage and Thermal Stress in Electronic Packaging

In electronic packaging, the necessity of controlling thermal stress and surface deformations is obvious. These two phenomena are directly related to reliability and yield issues. The magnitude and distribution of thermal stresses and surface deformations caused by uniform heating and cooling are problematic in electronic packaging e.g. for infrared sensor packaging.

Analytical models which are commonly used nowadays to determine thermal stress and surface deformations are based on bending of plates. Timeshenko's theory of bimetal thermostats (1925) determines only the maximum normal stresses in strips. This theory has been widely used in engineering applications for a long time. In 1986, Suhir proposed an extension over Timoshenko's theory. Evaluating normal stresses in thermostat plates as well as shearing and peeling stresses at the interfaces are possible with this theory.

According to this theory, the bi-metal plate given in Figure 1.5 whose components can be soldered, brazed together is subjected to uniform heating or cooling. Assume that coefficient of thermal expansion of the top layer is lower than the bottom layer, $\alpha_1 < \alpha_2$. Elastic material properties, elastic modulus and Poisson's ratio are represented by E and υ respectively. The thicknesses of the strips are h_1 and h_2 and b is the plate width. The longitudinal displacements $u_1(x)$ and $u_2(x)$ are given as follows [11].

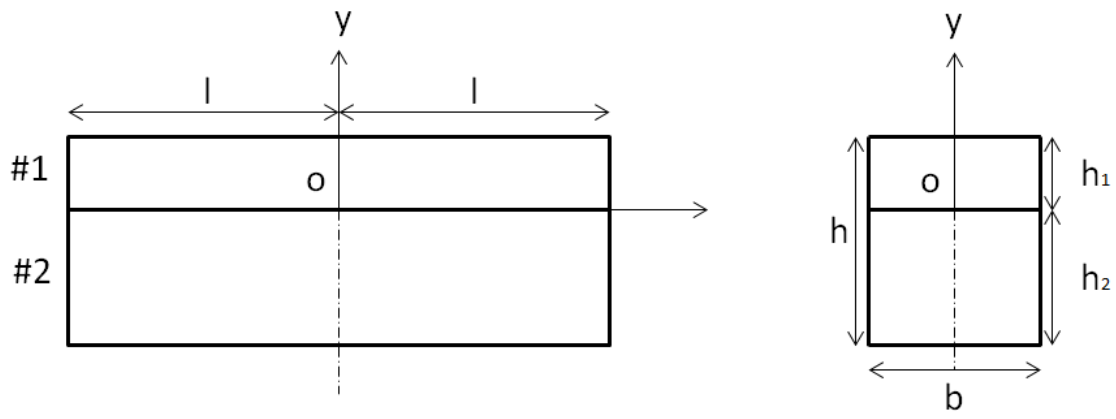

Figure 1.5: Themostat components

$$u_1(x) = \alpha_1 \Delta t x - \frac{1-\upsilon_1^2}{E_1 h_1 b}\int_0^x Q(\xi)d(\xi) + \kappa_1 q(x) + \frac{h_1}{2}\int_0^x \frac{d\xi}{\rho(\xi)} \tag{1.1}$$

$$u_2(x) = \alpha_2 \Delta t x - \frac{1-\upsilon_2^2}{E_2 h_2 b}\int_0^x Q(\xi)d(\xi) + \kappa_2 q(x) + \frac{h_2}{2}\int_0^x \frac{d\xi}{\rho(\xi)} \tag{1.2}$$

In equations 1.1 and 1.2, Δt is the temperature difference between initial and final states, x is the distance from the neutral axis, κ is the coefficient of interfacial compliance, Q is shearing force and $q(x)$ is the shearing force per unit length. The first terms in equation 1.1 and 1.2 are due to thermal expansions of the strips. The second terms are due to the forces $Q(x)$ and they are calculated by assuming these forces are uniformly distributed over the strip thickness and there does not exist a displacement in the direction of the plate width. The third terms are related to actual nonuniform distribution of the forces $Q(x)$. They take into account the shearing force only in the given cross section. The last terms are due to bending. The coefficients of interfacial compliance, κ [11] are given in equations 1.3.

$$\kappa_1 = \frac{2(1+\upsilon_1)}{3E_1} \times \frac{h_1}{b}, \quad \kappa_2 = \frac{2(1+\upsilon_2)}{3E_2} \times \frac{h_2}{b} \tag{1.3}$$

The forces acting on the cross section at x are shown in Figure 1.6. Shearing force per unit length is given as $q(x)$. $Q(x)$, the force at x cross section is defined as,

$$Q(x) = \int_{-l}^{x} q(\xi)d\xi \tag{1.4}$$

and the displacement consistency condition $u_1(x) = u_2(x)$ leads to

$$\kappa q(x) - \left(\frac{1-\upsilon_1^2}{E_1 h_1} + \frac{1-\upsilon_2^2}{E_2 h_2}\right)\int_0^x Q(\xi)d\xi + \frac{bh}{2}\int_0^x \frac{d(\xi)}{\rho(\xi)} = b\Delta\alpha\ \Delta t\ x \tag{1.5}$$

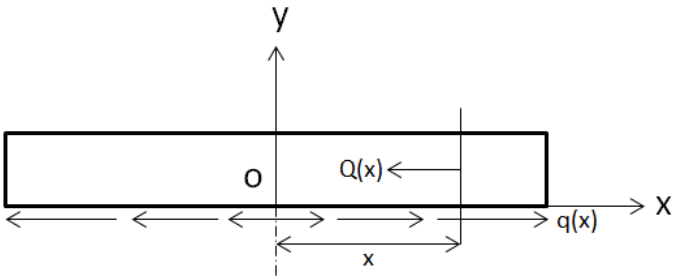

Figure 1.6: Cross sectional view

where ρ is the radius of curvature and

$$h = h_1 + h_2, \quad \Delta\alpha = \alpha_2 - \alpha_1, \quad \kappa = b(\kappa_1 + \kappa_2) = \frac{2(1+\upsilon_1)}{3E_1}h_1 + \frac{2(1+\upsilon_2)}{3E_2}h_2 \quad (1.6)$$

The equation of equilibrium for a portion of the plate is given as,

$$M_1(x) + M_2(x) - \frac{h}{2}Q(x) = 0 \quad (1.7)$$

where

$$M_1(x) = \frac{bD_1}{\rho(x)}, \quad M_2(x) = \frac{bD_2}{\rho(x)} \quad (1.8)$$

are bending moments and

$$D_1 = \frac{E_1 \times h_1^3}{12(1-\upsilon_1^2)}, \quad D_2 = \frac{E_2 \times h_2^3}{12(1-\upsilon_2^2)} \quad (1.9)$$

are flexural rigidities. From Equations 1.7 and 1.8

$$\frac{1}{\rho(x)} = \frac{h}{2bD}Q(x), \quad D = D_1 + D_2 \quad (1.10)$$

After substituting equation 1.10 in equation 1.5 and applying boundary conditions $q(0) = 0$ and $Q(l) = 0$, the shearing force per unit length can be found as

$$q(x) = \frac{b\Delta\alpha\Delta t}{k\kappa\cosh(kl)}\sinh(kx) \quad (1.11)$$

and shearing stress is

$$\tau(x) = \frac{q(x)}{b} = \frac{\Delta\alpha\Delta t}{k\kappa\cosh(kl)}\sinh(kx) \quad (1.12)$$

where

$$k^2 = \frac{\lambda}{\kappa}, \quad \lambda = \frac{1}{12}\left(\frac{h_1^2}{D_1} + \frac{h_2^2}{D_2} + \frac{3h^2}{D}\right) \quad (1.13)$$

According to shear stress formula, maximum shear stress exists at the ends of the plate. Shear stress drops exponentially with the decrease in x. When equation 1.11 is combined with equation 1.4, Q(x) is obtained as,

$$Q(x) = -\frac{b\Delta\alpha\Delta t}{\lambda}\chi(x) \tag{1.14}$$

where the function

$$\chi(x) = 1 - \frac{\cosh(kx)}{\cosh(kl)} \tag{1.15}$$

defines how the forces $Q(x)$ and normal stresses will be distributed over plate length.When equation 1.10 is rewritten by substituting $Q(x)$ from equation 1.14, the plate curvature is found as

$$\frac{1}{\rho(x)} = -\frac{h\Delta\alpha\Delta t}{2\lambda D}\,\chi(x) \tag{1.16}$$

and the bending moment equations turns out to be

$$M_1(x) = -\frac{bh\Delta\alpha\Delta t}{2\lambda D}D_1\chi(x), \quad M_2(x) = -\frac{bh\Delta\alpha\Delta t}{2\lambda D}D_2\chi(x) \tag{1.17}$$

The normal stresses caused by forces $Q(x)$ and moments $M_1(x)$ and $M_2(x)$ are given as follows;

$$\sigma_1(x) = \frac{\Delta\alpha\Delta t}{\lambda h_1} \times \big[1 + \frac{3hD_1}{h_1 D}\big]\chi(x), \tag{1.18}$$

$$\sigma_2(x) = \frac{\Delta\alpha\Delta t}{\lambda h_2} \times \big[1 + \frac{3hD_2}{h_2 D}\big]\chi(x) \tag{1.19}$$

In 1986, Suhir's study covered stresses in bi-metal thermostats. However this study with Timoshenko's theory of bimetallic thermostat created the infrastructure of commonly used predictions of thermal stresses and surface deformations in today's electronic packaging. Vujosevic [3] analyzed thermally induced deformation in die-substrate assembly by using Plate Theory and Suhir's solution for stresses in a tri-material assembly. In this study, the deformations on Flip Chip Ball Grid Array(FCBGA) package shown in Figure 1.7 are determined analytically and the results are compared with those of finite element analysis (FEA).

In an analytical model, definition of a BGA structure is not possible. Underfill epoxy and solder interconnects are modeled as a single layer of underfill material. In FCBGA

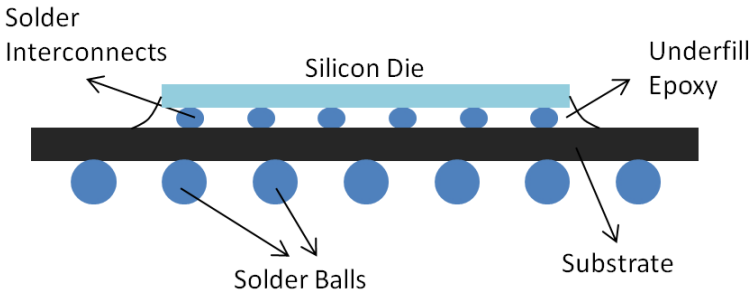

Figure 1.7: Flip chip ball grid array (FCBGA)

packages, warpage is an important factor for reliability. When bending of the package is too large, two possible consequences can be observed according to this study:

1. Solder balls cannot satisfy proper contact with the board which results in open circuit;

2. If a low pitch size is used in the BGA structure, during the extension of balls, they may contact each other which results in short circuit.

To improve the reliability of FCBGA packages, warpage behavior is discussed with analytical methods. A trimaterial assembly is defined in Figure 1.8 with material properties elastic modulus, coefficient of thermal expansion and Poisson's ratio, represented by E_i, α_i, υ_i where $i = 1, 2, 3$ for die, underfill and substrate materials, respectively.

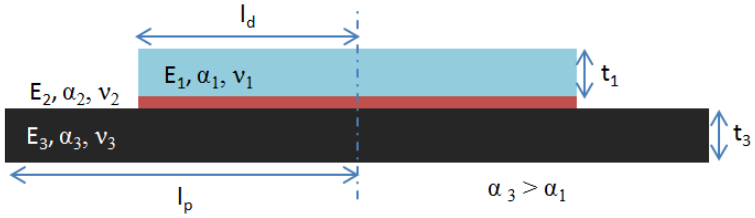

Figure 1.8: FCBGA assembly

Suhir's analytical model is based on small deflection plate theory [12], [13] linear elastic isotropic material behavior and the following assumptions:

- adhesive material thickness is very small with respect to the thickness of the die and the substrate materials;
- compliance of the die and substrate materials is significantly lower than adhesive material compliance;
- a perfect surface to surface bonding is assumed between interfaces;

- each layer of the assembly acts as a spherically bent plate.

The normal stresses on the die and the substrate, shear stress on the adhesive layer has been provided in this study. The coefficient of thermal expansion of the adhesive material was not included in the stress expressions because of very small thickness and / or low modulus of elasticity of this material. However the major interest of the present study is warpage predictions on the defined assembly. To determine the deflections of the substrate, existence of small displacements and spherical bending have been assumed.

In spherical bending, the curvature in O-A-B-C region which is shown in Figure 1.9 is constant and it is related to bending moment. The curvature along the path O-A is given as

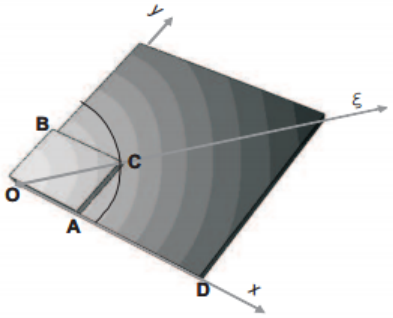

Figure 1.9: Quarter of the package [3]

$$\frac{1}{\rho(x)} = \frac{t\Delta\alpha\Delta T}{2\lambda D}\left(1 - \frac{\cosh(kx)}{\cosh(kl_d)}\right) \tag{1.20}$$

where

$$\lambda = \frac{1-\upsilon_1}{E_1 t_1} + \frac{1-\upsilon_3}{E_3 t_3} + \frac{t^2}{4D} \tag{1.21}$$

is the axial compliance of the assembly,

$$D = D_1 + D_2 + D_3 \tag{1.22}$$

$$D_i = \frac{E_i t_i^3}{12(1-\upsilon_i)} \tag{1.23}$$

$$\tag{1.24}$$

D_i (material i, $i = 1, 2, 3$) is the flexural rigidity of an individual plate,

$$k = \sqrt{\frac{\lambda}{K}} \tag{1.25}$$

represents the longitudinal compliance and

$$K = \frac{t_1}{3G_1} + \frac{2t_2}{3G_2} + \frac{t_3}{3G_3} \tag{1.26}$$

is the interface compliance. G_i represents the shear modulus of material ($i = 1, 2, 3$, respectively). Through the integration, the out of plane displacement along the x axis in the region O-A are obtained as

$$w(x) = \frac{t\Delta\alpha\Delta T}{2\lambda D}\left(\frac{x^2}{2} - \frac{\cosh(kx) - 1}{k^2\cosh(kl_d)}\right) \tag{1.27}$$

The out of plane deflections increase towards to the tips. To determine the maximum out of plane deflection, the deflection along the diagonal path C -E is defined as

$$w(\xi) = \frac{t\Delta\alpha\Delta T}{2\lambda D}\left(l_d^2 - \frac{2}{k^2} + \frac{2}{k^2\cosh(kl_d)} + (l_d - \frac{\tanh(kl_d)}{k})(\xi - l_d)\sqrt{2}\right) \tag{1.28}$$

The peak warpage (maximum out of plane deformation) occurs when $\xi = l_p\sqrt{2}$,

$$w_{max} = \frac{t\Delta\alpha\Delta T}{2\lambda D}\left(l_d^2 - \frac{2}{k^2} + \frac{2}{k^2\cosh(kl_d)} + (l_d - \frac{\tanh(kl_d)}{k})(l_p - l_d)\sqrt{2}\right) \tag{1.29}$$

By using this developed model, the warpage behavior of the trimaterial assembly has been investigated with different geometrical and material parameters. Analyses have been performed for different material properties such as the coefficient of thermal expansion values of the die and the substrate, glass transition temperature of the underfill and elastic properties of constituents. Then, the effect of geometrical parameters such as thicknesses and planar dimensions of die and substrate on warpage of the assembly has been analyzed.

Moreover, Tsai *et al.* [14] also used Suhir's solution to predict the warpage of FCBGA packages with low and high glass transition temperature underfill materials. In another study, Tsai *et al.* [15] studied the curing effect of adhesive material on warpage in electronic packaging by using analytical predictions and FEM.

1.2.2 Warpage and Thermal Stress Predictions on Cooled IR Sensors

Cooled IR sensors suffer from thermal stresses caused by large differences between operation and storage temperatures. To improve the reliability of the sensor, warpage and thermal stress predictions have previously been carried out. However, limited

published data exist in the literature.

In the study of Haiyan and Huajie [16], the two failure modes of Infrared Focal Plane Array(IRFPA) under thermal stress are mentioned. The performance degradation is reported to be mainly due to the change in the forbidden gap of the MCT film under stress. For crack formation in the die, the exerted stress on epitaxial wafer should exceed the ultimate strength of the material. IRFPA assembly composed of sapphire electrical lead board, glue, silicon ROIC, indium bumps, MCT and substrate layers as it is shown in Figure 1.10. In their FEA, temperature changed from 300 K to 77 K uniformly on the whole assembly. The thermal stress sustained by substrate and MCT layer has been analyzed. The von Mises stress found for different substrate thicknesses are given in Table 1.4. According to given results, the thermal stress on MCT layer

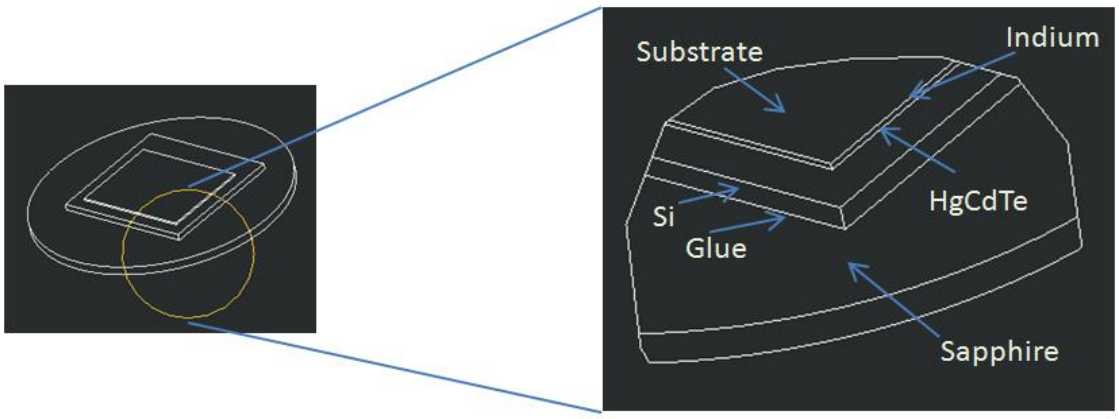

Figure 1.10: Representative structure of IRFPA

decreases with increasing substrate thickness. However, as the substrate gets thicker, thermal stress on the substrate diminishes at first, then it increases. Hence, the optimal thickness of the substrate yielding minimum stress is defined to be about 50 – 100 μm. Another research on the thermal management of cooled infrared MCT sensor was performed by Wu *et al.* [2]. The two failure modes of the IRFPA caused by the mismatch in the coefficient of thermal expansions have also been discussed for long linear MCT arrays (Figure 1.11) in this study.

Table1.4: von Mises stress for different substrate thicknesses [1]

Substrate Thickness (μm)	0	5	10	20	50	100	200	300	500
Mises MCT (MPa)	45	45	45	42	41	40	35	30-40	28-37
Mises Substrate (MPa)	NA	14-37	8-35	5-30	1-31	3-35	4-40	4-49	5-63

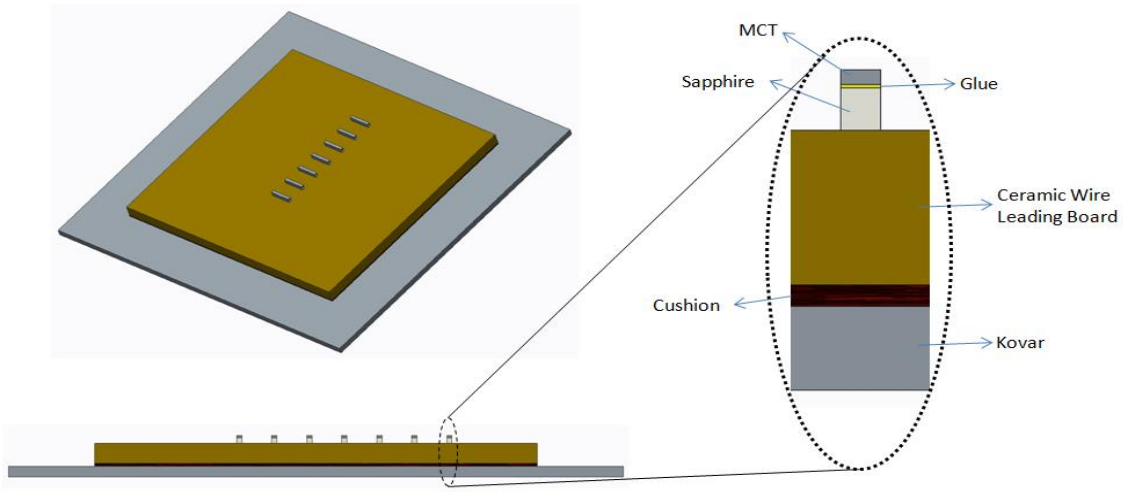

Figure 1.11: Long linear MCT array structure

According to performed FEA, Wu *et al.* [2] claimed that there exist two major factors which introduce thermal stresses: first one is the sapphire substrate thickness and the second one is the material parameters such as the elastic modulus or Poisson's ratio of various materials. To reduce thermal stresses, two different parameters were analyzed in this study: the first one was adding a metal cushion into the assembly; the second one was analyzing the effec of ceramic board thickness on the thermal stress. In the range of these parameters, thermal stress is optimized. Modeling only one glue layer which stands below the MCT layer was an important aspect. Although the glue was also used between some other layers, they were not modeled. The thickness of MCT layer was comparable with the thickness below the glue layer. However, the other glue layers were thought to be too thin to be modeled in the FEA. As a result, the other glue layers were ignored. Although the temperature dependant material properties need to be used in the analysis, because of difficulties in obtaining cryogenic temperature material properties, room temperature properties were used as inputs for the FEA.

In Wu *et al.*'s study [2], firstly, the thermal stress was analyzed by adding different

metal cushions under the ceramic board. Without any cushion, the maximum stress was found as 64.7 MPa at the bottom of MCT layer. Totally six candidate materials were analyzed for cushion integration and the obtained maximum stress values are given in Table 1.5.

Table1.5: Thermal stresses by adding different cushions [2]

Cushion Material	Mo	Steel Rolling	Invar	Cu - Alloy	Bronze(Cu 11000)
Max Mises Stress (MPa)	54.1	44.9	44.2	53.5	44.9

Secondly, the thickness of the ceramic board was analyzed for six different values 1 mm, 2 mm, 3.5 mm, 3.7 mm, 4 mm and 5 mm. According to the FEA results shown in Figure 1.12, the thermal stress was minimum (44.5 MPa) for 3.5 mm and 3.7 mm thick ceramic boards. According to the mentioned two analyses, it was predicted that the

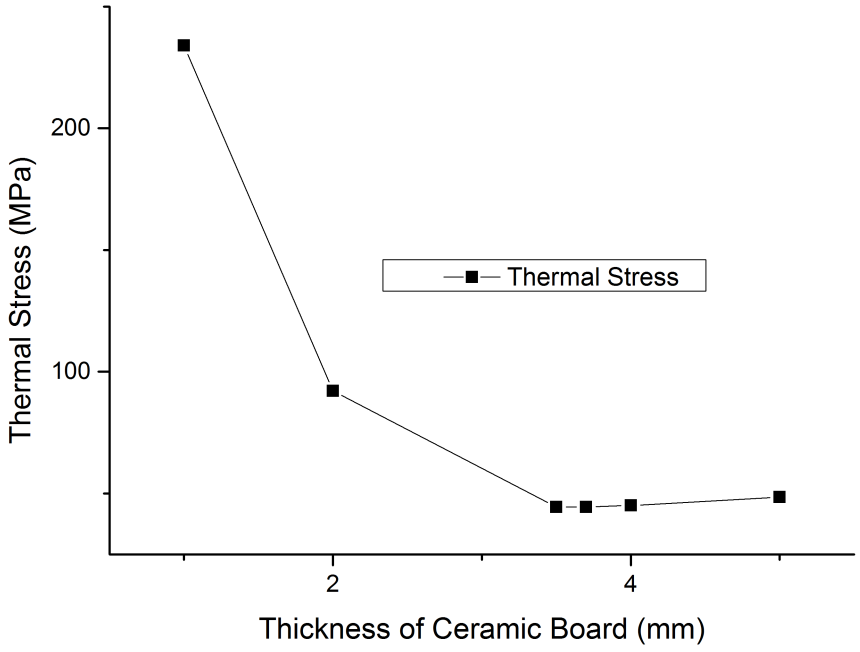

Figure 1.12: FEM results for different thicknesses of ceramic board

minimum stress could be achieved by using 3.7 mm ceramic board with Invar cushion material. A final FEA proved this providence with 42.6 MPa maximum thermal stress. MCT material has been widely studied among cooled IR sensors. The brittle nature

of very thin MCT may cause critical reliability issues during operation. Hence design optimization is a critical part of constructing a MCT sensor structure.

Indium antimonide (InSb) is a III – V group semiconductor material. It is also used as an IR detector material. The InSb sensors are very sensitive in a narrow band gap, 1 – 5 μm. In the literature, there are a few studies for the thermal management considerations of InSb infrared sensor. In one of these studies, a fracture analysis of InSb focal plane has been performed by Geng *et al* [4]. In this study, the authors claimed that thermal shock during cryocooling causes fracture of chips which was the main factor of InSb FPA chip failure. In this study, two main causes of InSb chip fracture were found as the process damage and thermal stresses. The analyzed structure was composed of InSb chip, indium bumps and silicon ROIC (Figure 1.13).

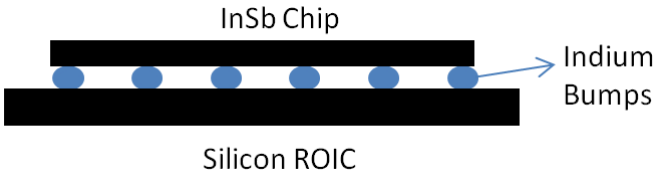

Figure 1.13: InSb FPA structure analyzed in [4]

A special test equipment was used in the mentioned study to apply thermal shock on the InSb FPA structure. Liquid nitrogen was used on this test setup to achieve cryogenic temperatures. The temperature of the InSb chip was reduced from ambient temperature to 77 K in 10 minutes which is even a longer time than some cooled IR sensor applications. In Figure 1.14a, a crack moves through the edge without

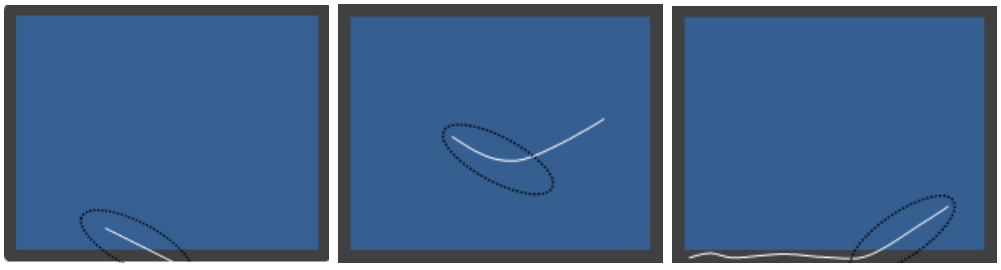

(a) Type 1 (b) Type 2 (c) Type 3

Figure 1.14: Crack types on InSb FPA (adopted from [4])

changing its direction. It is an example for thermal stress originated cracks. The

thermal mismatch between underfill, indium bumps, silicon ROIC and InSb layer may cause this type of cracks. The stress distributed in the indium bumps are transferred to InSb chip. When the InSb layer is thinned beyond some critical limit, this stress may start a crack which extends along the lowest binding energy plane. From Figure 1.14a, the crack propagation plane goes along the edge. In Figure 1.14b, crack originates at one side of the FPA chip and it is not observed on the other side. During the polishing process of InSb, particles come in contact with InSb surface causing a contact pressure on the surface. When relatively big particles are not cleaned periodically, grooves may originate as well. If this process is continued by a chemical polishing process, as it was performed in this study, material defects can cause difference in the etching speed in some areas during wet etching. This can easily result in crack propagation during thermal shock and thermal cycling. This type of crack is shown in Figure 1.14b.

Figure 1.14c indicates clearly a different history for this FPA. The crack started to propagate from the edge and it elongated till the middle of the chip. After InSb arrays were prepared, dicing was performed to have individual FPAs from wafer. During dicing process, wire saws are used to cut individual pieces. Because of the cutting impact, edge breakage may occur on the InSb chip. This edge breakage originates a crack which propagates during thermal shock.

To improve the yield of InSb chips, these three sources of crack initiation and propagation have been optimized. Firstly, the underfill material optimization was performed and minimizing the thermal stresses was aimed. The effect of degassing and curing processes on thermal stress were determined. Secondly, the backside thinning process was optimized such as determining rotational speed of wheel and periodically removing large polishing particles are removed periodically. Finally, the dicing process was optimized by determining the right feed rate and control precision of wire saws [4].

One out of three reasons of crack initiation and propagation in InSb chips is directly related to thermal stress management of the sensor. The remaining parameters are related to sensor construction parameters. Even though, these remaining parameters seem to be out of the scope of this thesis, they are very important for experimental studies of warpage determination. Because even the same test setup is used for measuring warpage of two different IR sensors, if the process parameters such as the

wire saw cutting feed rate, backside thinning feed rate etc. are different for these two, additional deflection behavior may be introduced on the sensor structure.

In all of the IRFPA thermal stress analyses until this point, linear elastic material properties have been defined. However, Meng *et al.* [17] defined viscoplastic constitutive model to describe behavior of indium bump material [18, 19]. In this study, very similar structure to that given in Figure 1.13 was used. The silicon ROIC, the InSb chip, the indium bumps and underfill materials were modeled. Underfill material was defined with viscoelastic, time and temperature dependent, material properties for 8×8 InSb array. However, stress dependency of different indium bump sizes was not obvious under mentioned circumstances. For 32×32 InSb array, underfill material was defined with linear elastic material properties. For both structures, the indium bumps were considered to have viscoplastic material properties. According to Meng *et al.* [17], the indium bump deformation was strongly temperature and time dependant and associated with the irreversible, temperature and rate dependent inelastic characteristics, which are known to be viscoplastic [17, 20].

Chen *et al.* [21] analyzed a MCT IR sensor structure with indirect hybridization. Unlike direct hybridization, the MCT detection layer and silicon ROIC are integrated separately on an electrical lead board via flip chip bonding in indirect hybridization. On the other hand, IR sensor array is directly integrated on silicon ROIC in direct hybrid IRFPA detectors. The coefficient of thermal expansion (CTE) value of sensor material is three or four times the coefficient of thermal expansion of silicon in the temperature range of 300 K to 77 K. However, CTE values of the detection layer and the electrical lead board are close to each other. Hence, indirect hybrid IRFPAs had higher thermal cycling reliability [21]. The effects of three parameters on warpage and thermal stress were discussed in this study. The effect of distance "*d*" between the silicon and the detection material on warpage was the first investigated parameter. As the distance d increased, both warpage and thermal stress on sensor chip decreased. Warpage and thermal stress on the sensor chip was mainly caused by thermal mismatch between the silicon ROIC and the sapphire electrical lead board. When the distance d was increased, the influence of thermal mismatch reduced. Secondly, the effect of electrical lead board thickness on warpage and thermal stress was determined. When the sapphire electrical lead board thickness was raised from 0.5 mm to 2.0 mm, the

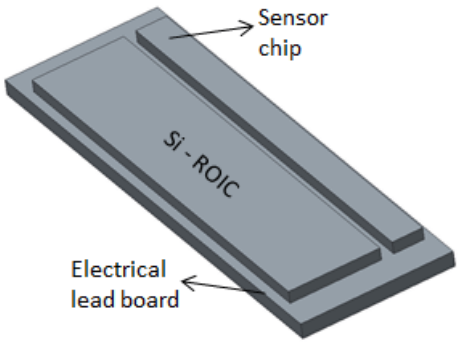

Figure 1.15: Indirect integration of IRFPA

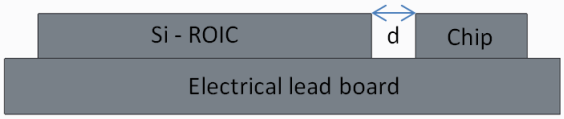

Figure 1.16: The distance, d, between the silicon ROIC and the sensor chip

thermal stress and warpage decreased. Finally, the electrical lead board material properties such as the CTE and Young's modulus were changed and their behavior of warpage and thermal stress were acquired. As Young's modulus increased, thermal stress dramatically increased at the beginning and then it reached a constant value. When the CTE of the electrical lead board was increased, thermal stress continuously decreased whereas warpage increased. It was reported that the results obtained from these analyses can easily be used to improve the thermal cycling reliability of indirect hybrid IRFPA structures.

Chen *et al.* [22] analyzed an IRFPA assembly model in terms of warpage and thermal stress behavior. In this study, MCT was used as the detection layer and GaAs was used as the substrate material. Warpage predictions were performed by both FEA and analytical predictions. Layer thicknesses of the assembly were adjusted to optimize the thermal stress distribution and warpage of the assembly. Homogeneous isotropic and linear elastic material models were used in the FEA. A uniform temperature distribution on the assembly was assumed. Theoretical calculations for out of plane deformations of the assembly were also performed. The theoretical calculations were based on bending theory which assumes pure bending and uniform expansion across the entire assembly [22].

By changing the sapphire electrical lead board, GaAs optical substrate and silicon

ROIC, thermal stress and warpage were mnimized. Von Mises Stress in the MCT layer was decreased from 41 MPa to 29 MPa whereas the warpage of the assembly was decreased from -10.2 μm to -5.5 μm.

In all of these studies, there existed some common outcomes which are itemized as follows;

• In IRFPAs, thermal stress and warpage are caused by great temperature changes and different CTE values of the layers;
• Warpage and the thermal stress on the sensor chip must be under control by optimizing the IRFPA structure design. This way the yield and temperature cycling reliability of these sensors can be improved;
• To predict warpage and thermal stress, FEM is widely used for IRFPAs;
• In all of the mentioned studies, homogeneous isotropic and linear elastic material properties have been used. Only in a single study [17], linear elastic and viscoplastic material models have been used in the FEA.
• Modeling glue layer is not strictly required if the glue thickness is not comparable with the bonded layers;
• In addition to prediction of warpage and thermal stresses for IRFPAs assembly, experimental verification of these outputs is rarely performed. Even for the experimental results mentioned fır the confirmation of FEM predictions, a clear experimental procedure and measurement method of warpage are not provided in the literature.

1.2.3 Interferometer Equipped Warpage Measurements in Electronic Packaging

Optical interferometers enable precise distance measurements by making the use of interference phenomena produced by laser light. Besides ease of application and good measurement sensitivity, optical interferometers are alternative non contact measurement devices which are commonly used in electronic packaging. Interferometers can be divided into two groups as two-beam interferometers or multiple beam interferometers according to the number of interfering beams. The most commonly used two beam interferometers are the Fizeau, the Michelson, the Mach – Zehnder interferometers, the

best known multiple beam interferometer is the Fabry – Perot interferometer [23], [24]. Some commonly used interferometer structures are described next.

• The Fizeau Interferometer:

A schematic for the Fizeau interferometer is given in Figure 1.17. Two flat surfaces are used in these interferometers. The first one is a reference flat surface, the second one is the test surface. The fringe pattern obtained due to the interference of the beams reflected from the reference and the test surfaces defines the profile of the test surface. Fizeau interferometers can also be used to test concave or convex surfaces when they are modified.

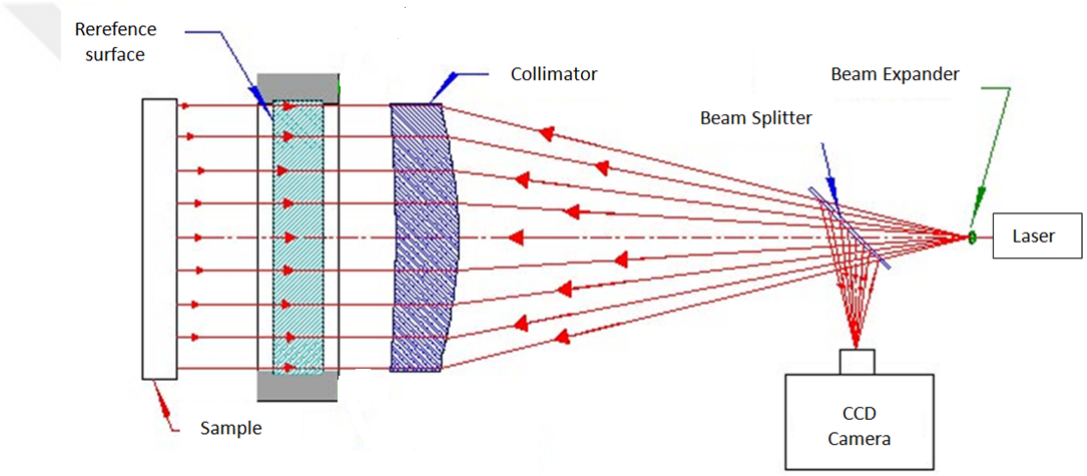

Figure 1.17: Fizeau laser interferometer

• The Michelson Interferometer:

The Michelson interferometer schematic is schematically shown in Figure 1.18. From the laser source, the incoming laser through the beam splitter is divided into two laser beams; one passes through the beam splitter, the other is reflected towards the compensating plate. The compensating plate is used to compensate the effect of the thickness of beam splitter on the first beam. It is used to equalize optical paths in glass. Note that one of the beams traverses beam splitter three times whereas the other one traverses only once.

There exists more than twenty types of interferometers including Shadow Moiré, Martin Puplett, Twyman Green, Rayleigh, Sagnac interferometers and many others [23].

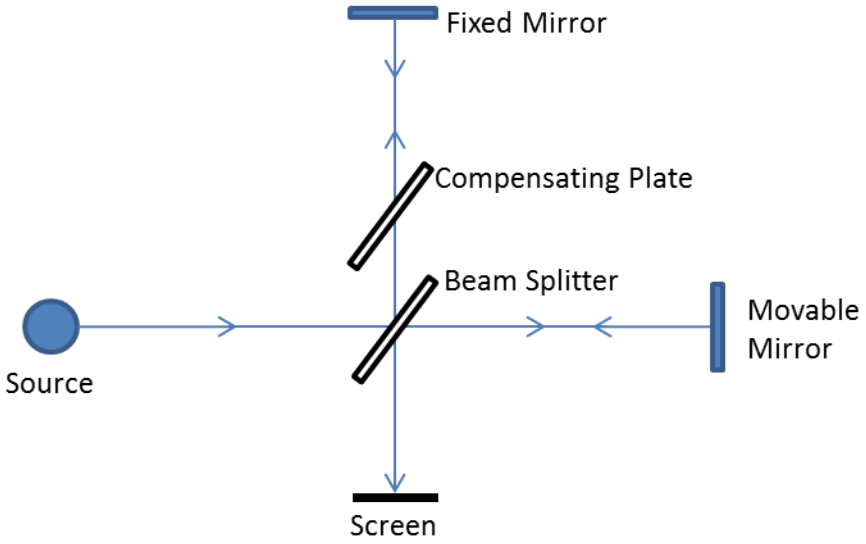

Figure 1.18: Michelson interferometer

In electronic packaging, thermal warpage analysis is commonly performed by using Tywman – Green interferometry, Shadow Moiré interferometry and Far Infrared (FIR) Fizeau interferometry.

• Twyman – Green Interferometer:

Twyman – Green interferometers can measure out of plane displacements with submicron sensitivity. A specular (mirror – like) surface is highly required for the operation of Twyman – Green interferometers. In addition to out of plane displacements, in plane strains can also be measured by combining Moiré interferometry with Twyman – Green interferometers. In Figure 1.19, the incoming laser is divided into two beams by the beam splitter. There exist two reflections: one is from the specimen surface which has surface profile information of specimen, the other is from the reference mirror which represents a perfectly flat surface of the reference mirror. These two beams meet again at the beam splitter and a portion of each move through the camera. By the interference of these two beams at the camera, the out of plane displacement of the specimen surface can be identified as

$$W(x,y) = \frac{\lambda}{2} \times N_z(x,y) \tag{1.30}$$

where N_z is defined as the fringe order at each point in the fringe pattern and λ is the wavelength of the laser. When He – Ne laser is employed ($\lambda = 633$ nm), the counter

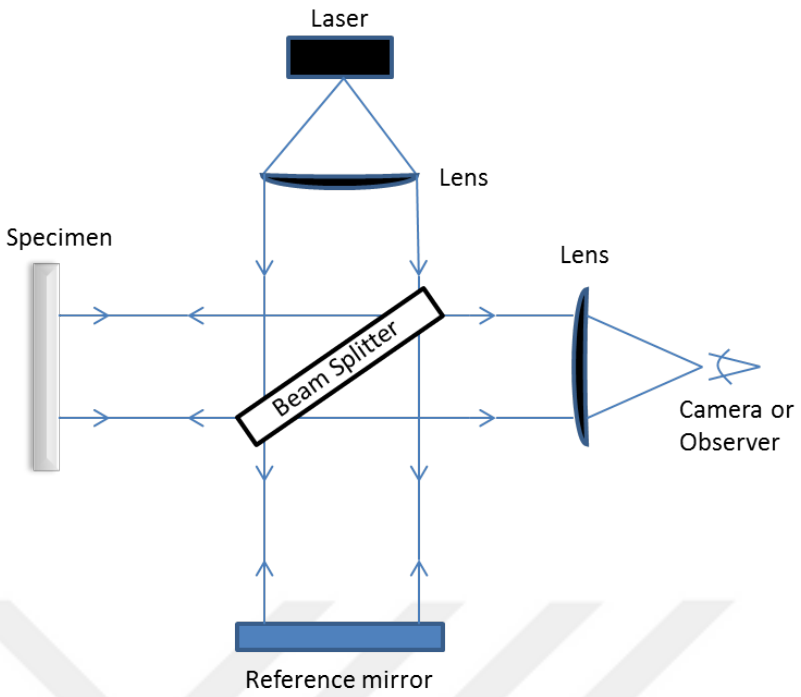

Figure 1.19: Twyman Green interferometer

interval of the fringe pattern is 316.5 nm per fringe order.

• Shadow Moiré Interferometer:

This interferometer shown in Figure 1.31 also provides measurement of out of plane displacements for the entire test surface, however, with a relatively lower sensitivity. For the measurements, having mirror like surface of test piece is not required. Its ability to measure rough surfaces and defined sensitivity (typically 25 to 50 μm per fringe order) make this method suitable for use in warpage measurements of printed circuit board (PCB) and most of the chip carrier packages [25]. In this method, there exists a grating in front of the tested specimen. The grating which is simply black bars and clear spaces on a flat glass plate has a shadow on the specimen. The grating and its shadows on the specimen create interference fringes. The out of plane displacement is found by

$$W(x,y) = \frac{N \cdot p}{tan\alpha + tan\beta} \times N_z(x,y) \tag{1.31}$$

where α represents the illumination angle, β is the observation angle and N is the fringe order and p is the grating pitch.

• Far infrared Fizeau interferometer

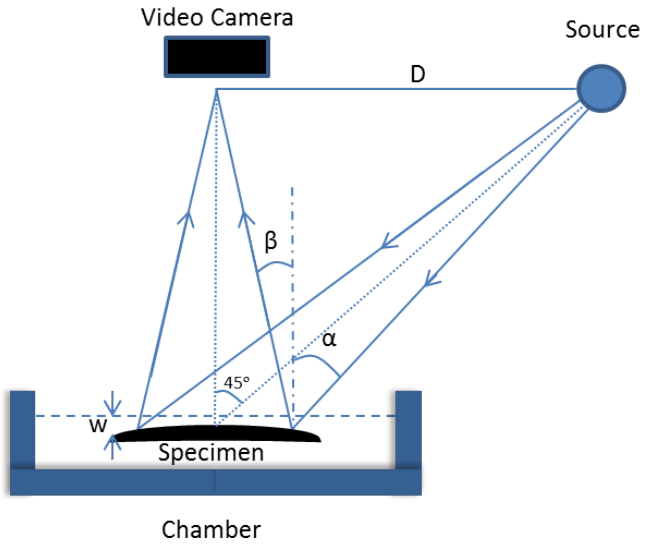

Figure 1.20: Shadow Moiré interferometer

To use FIR Fizeau interferometry, the surface should be specular reflecting just as in the case of Twyman - Green interferometer. The sensitivity of this method is a fraction of a micron which is very high for general electronic packaging warpage measurements. A sensitivity value on the order of micrometers is enough for warpage measurements of FCBGA packages. Although shadow Moiré method has enough sensitivity to measure warpage of FCBGA packages, the requirement for a special surface preparation, typically white matte paint on the specimen which can be considered as a destructive testing, is major disadvantage of this method. Moreover, because of very small distance between the grating and the specimen in shadow Moiré method, chip and substrate cannot be viewed simultaneously. By increasing wavelength or the angle of incidence, specular component of reflected light increases. This way, surfaces with high optical roughness can behave like a specular surface due to longer wavelength incidence. In contrast to Fizeau interferometry which uses visible light, FIR Fizeau interferometry uses long wavelengths such as 10.6 μm wavelength of CO_2 laser. The displacement can be determined by

$$W(x,y) = \frac{\lambda}{2 \times cos\theta} \times N_z(x,y) \tag{1.32}$$

where N is the fringe order at each point in the fringe pattern, θ is the angle of incidence, λ is laser wavelength [26].

Verma and Han [27], used FIR Fizeau interferometry to observe thermally induced

flip chip package. In this study, shadow Moiré, projection Moiré methods are classified as low sensitivity measurement methods. It is mentioned that surface preparation should be performed in these. The authors measured optically rough surfaces with a relatively good sensitivity 10.6 μm wavelength with 4° angle of incidence. It is mentioned that 5.31 μm displacement per fringe order meets the sensitivity requirements. The package and assembly structures which are given in Figure 1.21 were subjected to 180°C temperature difference from 140°C to −40°C. The warpage of the assembly and package showed nearly the same behavior for the chip area. The warpage of the substrate continued with a similar slope to that for the package configuration. On the other hand, the warpage value of the assembly does not change beyond the chip outline.

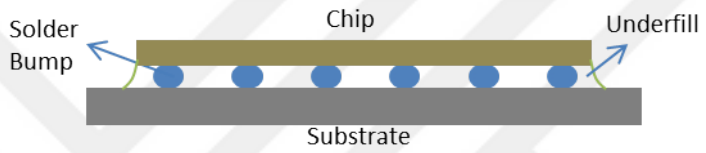

Figure 1.21: Package structure

Tsai *et al.* [28], worked on flip chip PBGA packages. FEM and Suhir's analytical solution [11] were used to predict the CTE mismatch based warpage of the substrate and the chip during thermal heating and cooling conditions. The package consisted of a die, a substrate and die attach materials. A total number of four packages were examined between temperatures of 260°C and 25°C. The warpage and die stress of FCBGA package which were formed during manufacturing of the assembly, and thermal cycling, and the warpage formed by the underfill effects were studied experimentally by Shadow Moiré interferometry. For the defined parameters in equation 1.31, g was approximately 25.4 μm, the values of α and β were 45° and 36.5°, respectively in the tests. The sensitivity of the system was 15 μm per fringe. The package outline was equivalent to 35mm ×35mm ×2.1mm with a 0.775 mm thick die, a 1.2 mm thick substrate and 0.122 mm thick underfill adhesive. Before testing the samples, a baking procedure took place at 125°C for at least 2 hours to get rid of effects of moisture. For different packages, there were different zero warpage temperatures. On the other hand, they had similar warpage rates. The difference of zero warpage temperature resulted in different maximum warpage values of the samples. The slope of the warpage changed

with changing temperature as a result of change in material properties for different temperatures. The warpage values were found as approximately 50 μm and -125 μm at 260°C and 25°C, respectively. One out of four packages was further analyzed by FEM and theoretical methods. The results showed good coherence so that it was noted that FEM and Suhir's model can be used to predict warpage of an FCBGA package.

Shadow Moire interferometry has been widely used in determining in-situ warpage of electronic packages [29], [30]. For example, Wen and Ku [31] used Shadow Moire method to measure in-situ, full field out of plane displacement of flip chip package under various temperature steps. They discussed the effect of six parameters including the dimensions of the substrate, thickness of substrate core, dispensing length of underfill, type of underfill, bump height and the thickness of silicon die for the flip chip package structure in Figure 1.22.

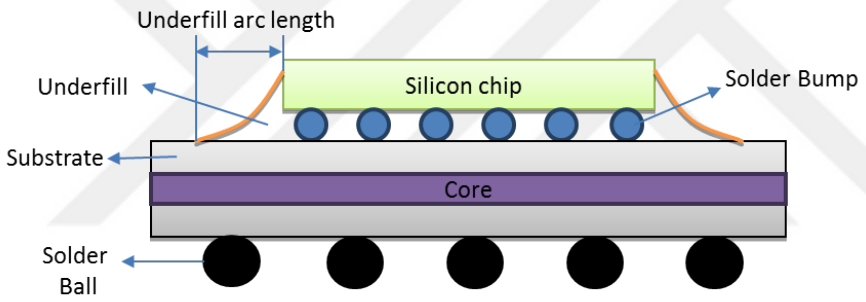

Figure 1.22: Representative outline of flip chip package

According to results of FEM analysis and experimental studies in [31];

• Underfill arc length is an important parameter that affects package warpage. Shorter underfill length results in smaller package warpage;

• Experimental results obtained by shadow Moire interferometry show good coherence with the FEA results.

• At high temperatures, substrate and core layers have more impact on warpage. However, manufacturing tolerance of these layers is also high. Controlling thee warpage by underfill arc length seems to be an easier solution.

Detailed schematic of the cold region materials is given in Figure 1.23. The cold shield

is excluded in this schematic because it is not relevant with the scope of the problem. At the top, there exists a detection layer which is a product of a series of micro

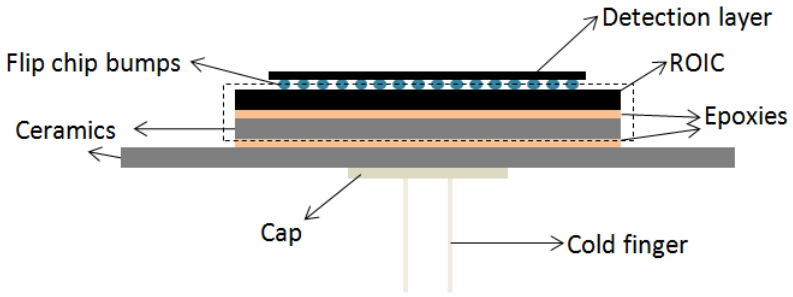

Figure 1.23: Cold region of vacuum envelope

fabrication processes of semiconductor materials. The output electrical signals are transferred from the detection layer to ROIC via flip chip bumps. It means that there is one flip chip bump for each and every pixel of the detection layer. A ROIC is built on silicon material, most commonly. Hybridization of the semiconductor detection layer and ROIC is performed by flip chip bonding process [32], [33]. A type of epoxy material named as underfill is applied between flip chip bumps in such a way that it fills the gap between the detection layer and the ROIC. This way, the underfill improves mechanical stability of the detection layer on ROIC. The silicon ROIC device is also made via micro fabrication processes which are beyond the scope of this thesis. The hybridized detection layer is called sensor which is integrated on a substrate using epoxy layers. Ceramics are widely used substrate materials. Depending on the design of the cold region, there may be one or more than one ceramic layers. All of these individual layers are integrated on top of each other using epoxy. Components 6–11 in Figure 1.3 which are named as cold region materials cool down during the operation condition. At idle state, the temperatures of these components are equal to ambient temperature. For the remaining components which are numbered as 1–5, the temperatures are slightly lowered during operation whereas it is equal to the ambient temperature at the idle state.

Semiconductor materials, ceramic materials, metal parts (cap and cold finger) and epoxies comprise a part of cold region materials. Different materials with different material properties such as elastic modulus, coefficient of thermal expansion and Poisson's ratio are integrated on top of each other. These materials are exposed to huge tem-

perature differences between operating and idle states. Due to mismatch in coefficient of thermal expansion of materials and huge temperature differences, surface deformations and thermal stresses arise on the structure. When excessive surface deformation or thermal stress develops on the integrated structure, performance degradation or direct mechanical failure can be observed on the detection material. If thermal stress on detection layer exceeds a certain limit at cryogenic temperatures, direct mechanical failure can be observed on the structure so that sustaining infrared imaging is impossible after that point.

Even if a mechanical failure does not occur on the detection layer, flip chip bump interconnects may suffer due to thermal mismatch. The output electrical signal of the detection layer cannot be transferred and analyzed by the ROIC in case of a breakdown in interconnects. This leads to non formation of infrared image on some pixels. There are also examples of mechanical failure of integrated structures which are composed of epoxy and silicon materials, when they are exposed to cryogenic temperature shock (Figure 1.24). For reliability purposes, surface deformations and thermal stresses on

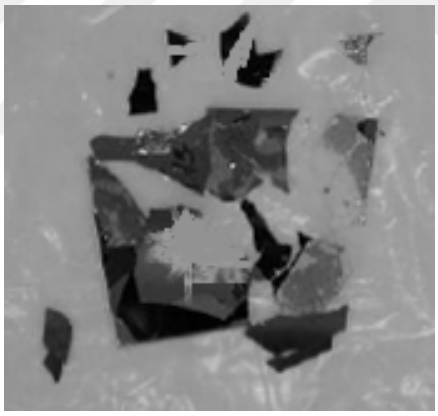

Figure 1.24: Silicon epoxy silicon integrated structure in liquid nitrogen bath

the detection layer should be optimized during design phase of this structure. According to studies in the literature, thermal stress and surface deformations are commonly controlled by changing the geometrical dimensions of individual components, or replacing / adding some parts on cold region materials. To analyse the deformation and thermal stress characteristics of a microelectronic device, finite element modelling is widely used as well as analytical modelling. However, experimental testing methodology and test setup details are not provided for cryogenic applications in the literature even if experimental results are given in some of the published studies.

1.3 Analytical Model vs Finite Element Model

Warpage predictions in electronic packaging structures can be performed using analytical and numerical models. However, analytical models for warpage and thermal stress prediction [11] are based on assumptions. One of them assumes that thickness of the adhesive layer is very small with respect to the thickness of the adherents. This assumption may restrict estimation of the warpage behavior for extreme thicknesses. To validate this idea a comparison between analytical and numerical modelling has been performed. For the analytical model, Vujosevic's [3] effective warpage formulation is used as analytical model output and it is based on the equation 1.29. The effective warpage is defined as

$$W_{\text{eff}} = \frac{W \times 10^3}{\Delta\alpha \ \Delta T} \tag{1.33}$$

where $W = w_{\max}$ in equation 1.29, $\Delta\alpha$ is the difference between coefficient of thermal expansion values of die and substrate which are given in Figure 1.25 and ΔT is the temperature difference that the assembly is exposed to.



Figure 1.25: Die substrate assembly

The material properties of the die-substrate assembly is given in Table 1.6. The planar dimension of all parts is defined as 15 mm × 15 mm.

Table1.6: Material properties of die-substrate assembly

Material	α $[ppm/K]$	E $[GPa]$	υ
Die	2.5	130	0.28
Adhesive	31	8.3	0.30
Substrate	14.3	16.4	0.20

The finite element analysis (FEA) and analytical solution is performed with different die and substrate thickness. For the FEA, linear homogeneous isotropic material behavior is assumed for all of the materials. A temperature difference of 145°C is

applied uniformly on the assembly. The effective warpage results for the FEA and analytical solution are given in Figures 1.26 and 1.27 For all analyses, adhesive layer

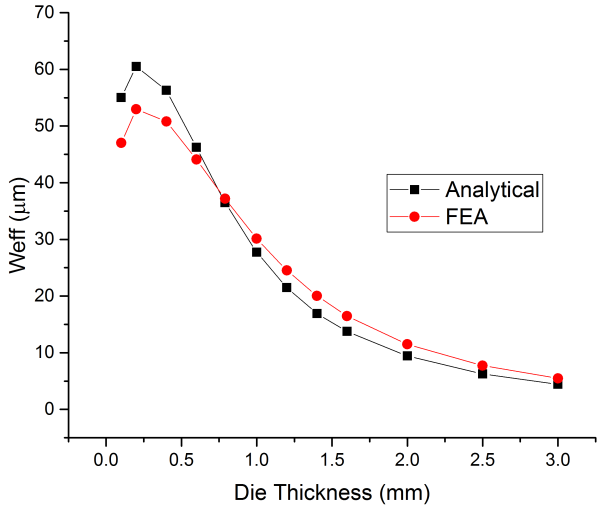

Figure 1.26: Die thickness versus effective warpage

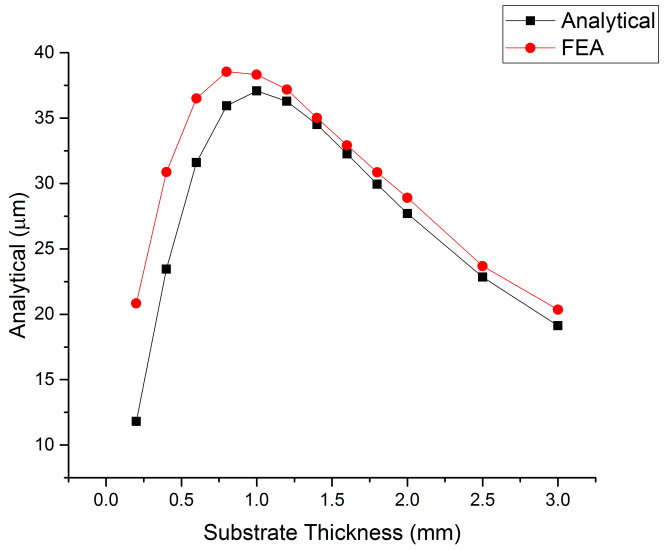

Figure 1.27: Substrate thickness versus effective warpage

thickness has been kept constant with a value of 0.085 mm. In Figure 1.26, analytical solution and FEA results show coherent trends for all parameters. However, when the die thickness is smaller than 0.5 mm, it has been observed that the gap between FEA and analytical results expands. A similar trend has also been observed in Figure 1.27. When the substrate thickness is greater than 1.00 mm, the FEA and analytical results

showed almost same quantities of effective warpage. If a smaller substrate thickness is analyzed, a clear gap has been observed between FEA and analytical results. It should be noted that for both cases of comparison of effective warpage, the FEA and analytical method showed the same trend.

As a result of the performed comparison between analytical and FEA solutions, both of the models may be used to predict warpage of a trimaterial assembly, if the assembly geometry is not complex. However, observing the warpage behavior of the assembly with very thin adherent thicknesses may deteriorate one of the assumptions in analytical model. This assumption says that the adhesive material thickness is very small with respect to the thickness of the die and the substrate materials. Another difference between the FEA and analytical solution is usage of coefficient of thermal expansion values of the adhesive layer. The analytical model does not use this material property whereas it must be given in the FEA.

In this study, FEA is preferred to determine the warpage of a trimaterial assembly. Hence, the warpage predictions will be performed with thin adherent layers.

1.4 Objective of Thesis

In this thesis, the main objectives are establishing a custom design test setup with a proper measurement method to measure micron level out of plane deformations, performing a FEA to determine surface deformations of materials, and verifying FEA results using experiments. Moreover, measurement errors and error sources regarding the test setup are defined. The FEA and experimental studies are performed on ceramic adhesive silicon integrated trimaterial structure. A part of the sensor or chip structure by excluding the flip chip bumps, underfill and detection layer is examined with numerical and experimental methods. In-situ measurements of out of plane deformations should be obtained at room temperature as well as at cryogenic temperatures. A phase shifting Fizeau laser interferometer system equipped test setup is utilized to perform the experimental studies. After having reliable experimental data with the constructed setup, the samples which are previously defined as a result of FEA are tested experimentally.

1.5 Outline

In Chapter 1, an introduction to infrared sensors and flip chip electronic packaging is given. Literature search data for surface deformation and thermal stress predictions in electronic packaging are also provided in this chapter. Possible measurement methods of measuring out of plane deformations of chip structure are determined as a part of literature search. After that the objective of the thesis is defined in Section 1.4. In the next chapter, finite element model is shared and performed parametric analyses results are discussed. Determined test method and two designs for test setup are given in Chapter 3. In the last section of this chapter, possible measurement error sources are determined and contribution of each source is analysed. Next chapter covers experimental procedure related to preparation of samples and construction of te test setup as well as measurement results on eight different samples. The effects of grinding process on warpage is analysed and comparison between numerical and experimental results is provided at the end of this chapter. Summary and recommendations for future work are given in the last chapter.

CHAPTER 2

FINITE ELEMENT ANALYSIS

2.1 Finite Element Model

A FEA has been performed on a part of the cold region materials. The detection layer, flip chip bumps and the underfill material have been excluded for both FEA and experimental verification. Only a three material of silicon as a ROIC material, adhesive epoxy and ceramic part has been considered as shown in Figure 2.1.

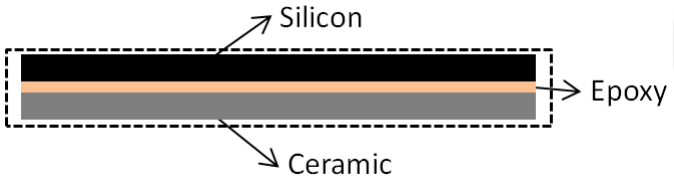

Figure 2.1: Analyzed three materials of cold region

To determine the out of plane deformations of this assembly, a linear static structural analysis has been performed on ANSYS Workbench. In the analysis, a linear elastic material behavior has been assumed and small deflection plate theory which is very suitable for our case has been employed. In all analyses, a time dependent load has not been applied on the materials. Thermal load caused by temperature change of the assembly and different thermal expansion coefficients of the materials drives the problem.

Homogeneous isotropic and linear elastic material properties have been used in the FEA. The elastic modulus, Poisson's ratio and coefficient of thermal expansion data for the three materials have been provided as input data. Although these properties

change with temperature in the range of 295 K to 80 K, it was not possible to find whole field temperature dependent properties in the literature. Luckily, the average values for the coefficient of thermal expansion of silicon and ceramic material in 300 K to 77 K range is obtained from the literature. Hence, these values are used for silicon and ceramic materials. Unfortunately, adhesive material properties and some properties of ceramic and silicon materials in the range of 295 K to 80 K could not be obtained. The linear elastic material properties used in the FEA are given in Table 2.1.

Table2.1: Material properties

Material	α $[ppm/K]$	E $[GPa]$	υ
Silicon	1.14	112.4	0.280
Epoxy	45.28	7.1	0.350
Ceramic	3.23	392.5	0.228

In Table 2.1, α represents the coefficient of thermal expansion, E is Young's modulus and υ is Poisson's ratio.

In the FEA, out of plane deformations of the silicon layer is defined as the only output. All three components have the same planar dimensions, 10×10 mm. Due to symmetry, a quarter of the structure has been modeled. The initial material thicknesses have been defined as 0.63 mm, 0.05 mm and 0.5 mm for ceramic, epoxy and silicon materials, respectively.

A uniform thermal load has been applied on trimaterial assembly. The initial and final temperatures of the assembly have been defined as 295.15 K and 80 K, respectively. A uniform temperature distribution on individual layers has been assumed. No other load has been applied on the assembly. For the boundary conditions, symmetry surfaces have been defined as frictionless supports and the bottom node of the central axis has been defined as a fixed support (Figure 2.2).

2.2 Meshing: Solid 186 Element vs Solid 187 Element

To determine the out of plane surface deformations of the silicon layer, two types of elements have been used in the FEA. Solid 186 element and Solid 187 element which

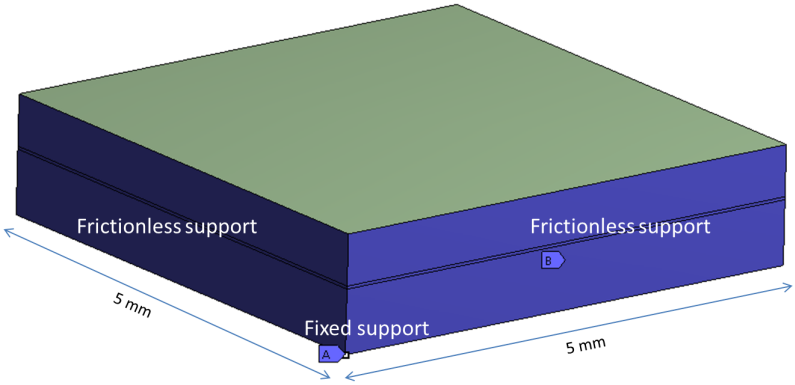

Figure 2.2: Defined supports in FEA

are commonly used in ANSYS Workbench have been defined in the model and the mesh dependency of the results for these two cases, have been compared. The element size of the materials have been determined according to defined material thicknesses in the FEA. The negative deflection value indicates that the surface has a convex shape. If the deflection named as warpage is given with a positive value that means the surface is concave. This situation is valid for all of the given warpage results.

In Figure 2.3, two conditions of the trimaterial assembly are shown. One shows the undeformed model of trimaterial assembly whereas the other represents the warpage behavior of the assembly when it is subjected to cryogenic cooling.

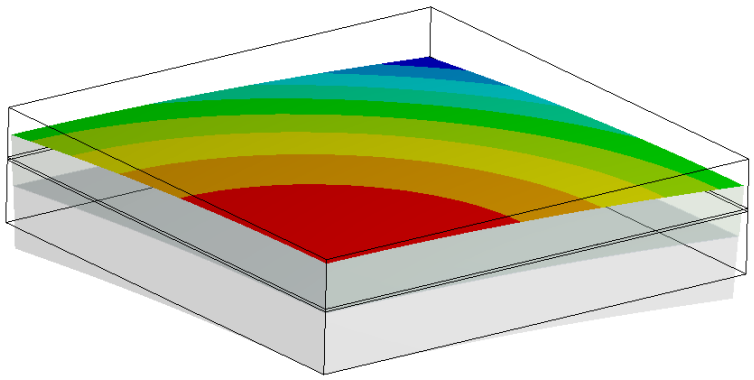

Figure 2.3: Representative deformed trimaterial assembly

2.2.1 Solid 186 element

Solid 186 element which is named as "Hex 20" by ANSYS Workbench is a 20 node hexahedral element. In the first step, only Hex 20 elements have been used in meshing.

2.2.1.1 Epoxy element size

At this step, the mesh density effect on the surface deformation of silicon has been assessed. At first, the size effect of the epoxy element has been determined in the range of 50 to 500 μm element size. The directional deformation of silicon with respect to changing Hex 20 epoxy element size is given in Figure 2.4.

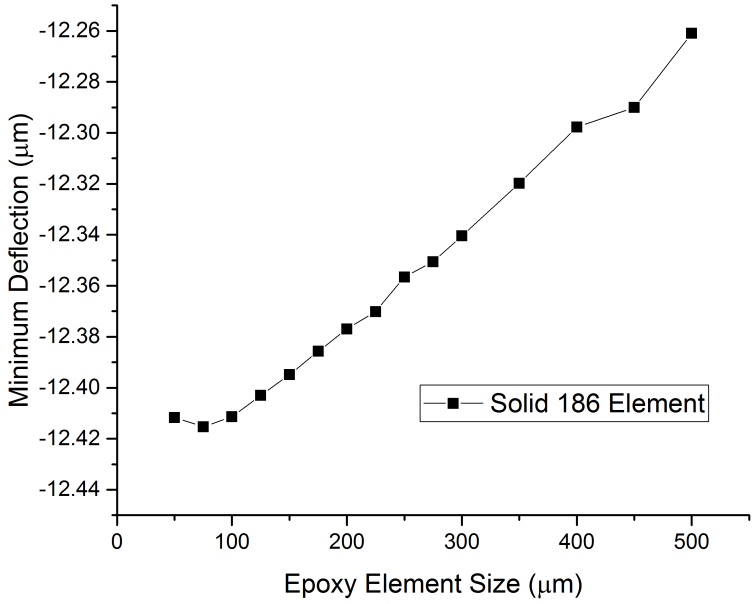

Figure 2.4: Epoxy mesh size effect with Hex 20 elements

According to the results, the maximum out of plane deflection of silicon surface is not effected by Hex 20 element size and it is -1.493 μm for all of cases. However, the minimum deflection differs in the range of -12.415 μm to -12.261 μm and it decreases with decreasing element size. The last three results imply that the minimum deflection reached a steady value. According to Figure 2.4, 75 μm mesh size can be used for the epoxy material. Note that the y axis in Figure 2.4 spans a 0.5 μm displacement range, starting from -12.0 μm and ending at -12.5 μm. If the axis is started from 0, the results appear to fall on a straight line and Hex 20 element size effect can be concluded as negligible. To represent small changes in deformation behavior, the results are printed in the given range.

2.2.1.2 Ceramic and silicon element size

At this stage, the element size of ceramic and silicon have been changed simultaneously and out of plane deformation of silicon has been recorded.

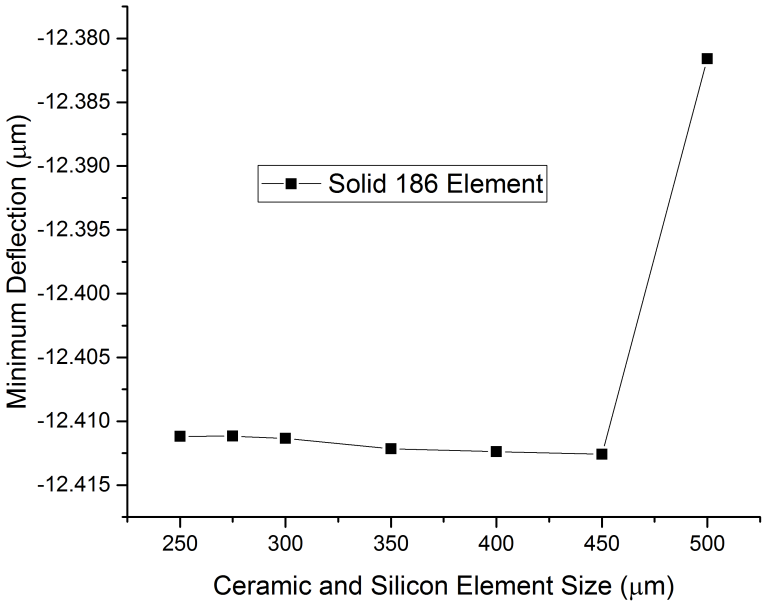

Figure 2.5: Ceramic and silicon mesh size effect with Hex 20 elements

Similar to the previous case, the y axis represents the minimum out of plane deformation of silicon in the range of -12.0 μm to -12.5 μm. The same maximum deformation value of -1.493 μm has been found with changing element thicknesses of ceramic and silicon layers. The element size changed between 250 μm and 500 μm and the directional deformations have been recorded again (Figure 2.5). In this range of the element size, the largest displacement difference was found to be 30 nm. The hexagonal element size of 300 μm has been used for ceramic and silicon layers for future analysis.

2.2.2 Solid 187 element

Solid 187 element which is named as "Tet 10" by ANSYS Workbench is a 10 node tetrahedral element. Only Tet 10 elements have been used in meshing in this subsection.

2.2.2.1 Epoxy element size

The tetrahedral mesh density effect of epoxy material on out of plane surface deformation of silicon has been investigated. The element size parameter changed from 50μm to 500μm as in Hex 20 case. The directional deformation behavior of silicon was very similar to that with the Solid 186 element.

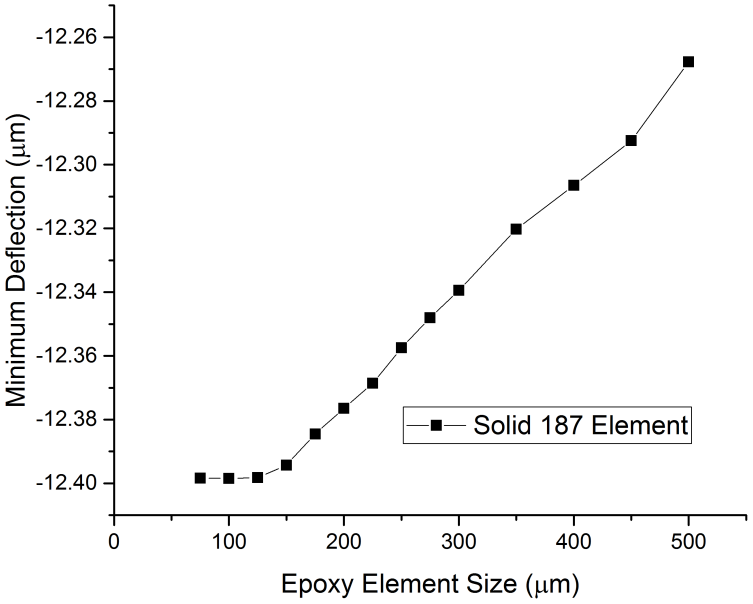

Figure 2.6: Epoxy mesh size effect with Tet 10 elements

The directional deformation of silicon surface reaches a steady state value around 100 μm Tet 10 element size (Figure 2.6).

2.2.2.2 Ceramic and silicon element size

Element sizes of ceramic and silicon materials are changed simultaneously in the range from 250μm to 500μm. Although the results do not seem to be converging, there exists 19 nm deflection difference between seven different element sizes. Figure 2.7 represents the directional deflection behavior of silicon.

As may be observed from Figure 2.8, there does not exist a clear difference between Hex 20 and Tet 10 elements for epoxy meshing especially when the element size is

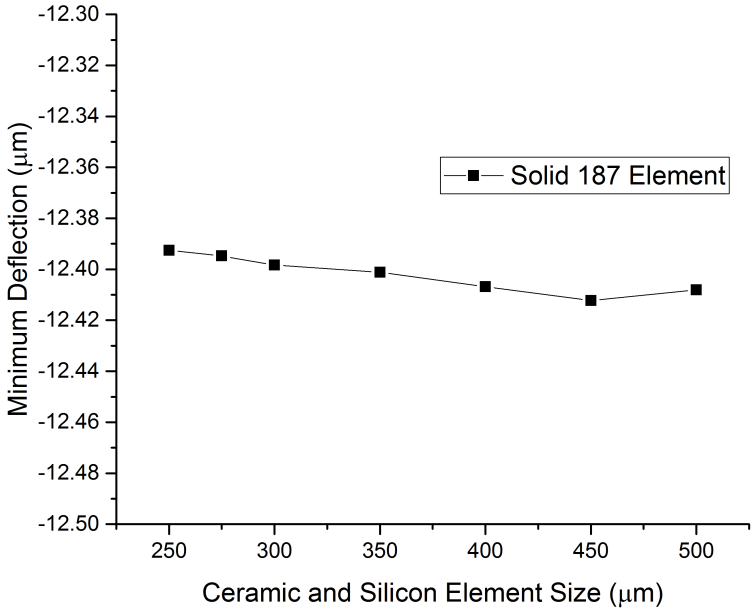

Figure 2.7: Ceramic and silicon mesh size effect with Tet 10 elements

bigger than 100 μm. For ceramic and silicon meshing, Hex 20 and Tet 10 elements show very small difference result, in Figure 2.9.

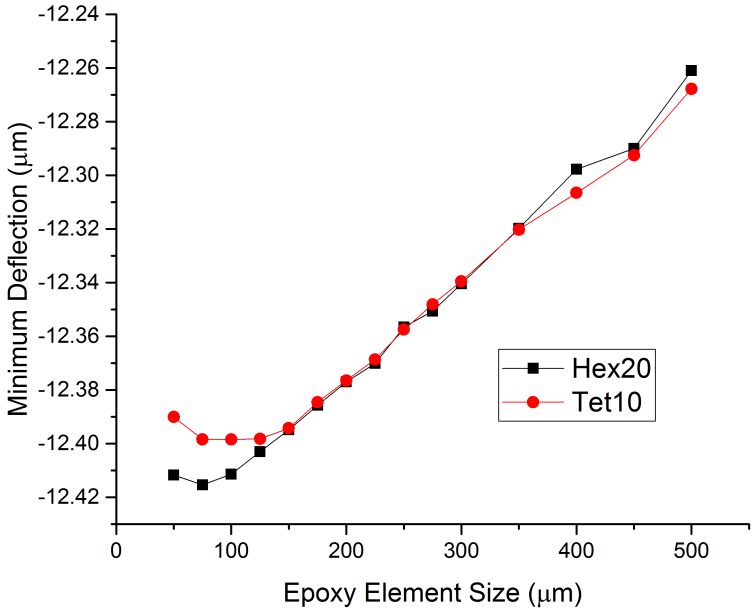

Figure 2.8: Comparison of Solid 186 and Solid 187 elements in epoxy meshing

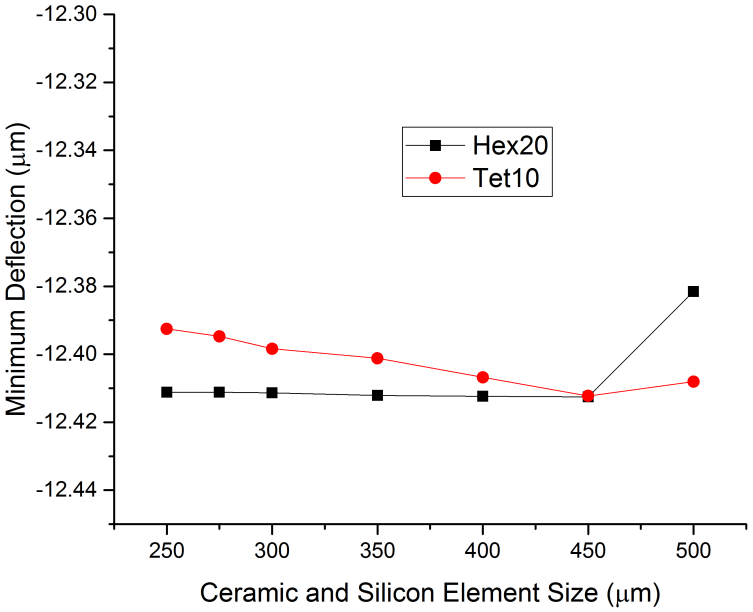

Figure 2.9: Comparison of Solid 186 and Solid 187 elements in ceramic and silicon meshing

Based on these results, Hex 20 element has been used in the FEA with 300 μm element size for silicon and ceramic parts and 75 μm element size for epoxy.

2.3 Parametric Analysis

After defining the element type and size which are used in the analyses, a parametric analysis has been performed. In this part, the effect of each layer's thickness on warpage has been examined. The planar dimensions of the materials have been kept constant as 10×10 mm. Four different thicknesses of ceramic namely, 0.63 mm, 0.8 mm, 1.00 mm and 1.27 mm have been analyzed. The effect of epoxy thickness has been discussed using twelve parameters in the range from 25 μm to 500 μm whereas the silicon thickness has been defined as 0.1 mm and increasing with 0.1 mm increments to 0.5 mm material thickness. According to this structure, a total number of 240 analyses have been performed. In all these analyses, the out of the plane deformation of silicon material which is named as warpage (Figure 3.1) is the only output. The

letter "w" defines the warpage which is the minimum distance between two parallel planes covering the upper surface of silicon.



Figure 2.10: Definition of warpage [5]

The warpage results are provided for each increment of silicon thickness.

2.3.1 0.5 mm silicon thickness

The PV value in Figure 2.11 which defines the difference between the maximum and minimum out of plane displacements of the silicon surface refers to the warpage of silicon. A minimum warpage value of 0.747 μm occurs among the performed 48 analyses when the ceramic thickness is 1.27 mm and the epoxy thickness equals to 0.4 mm for the case of 0.5 mm thick silicon (Figure 2.11).

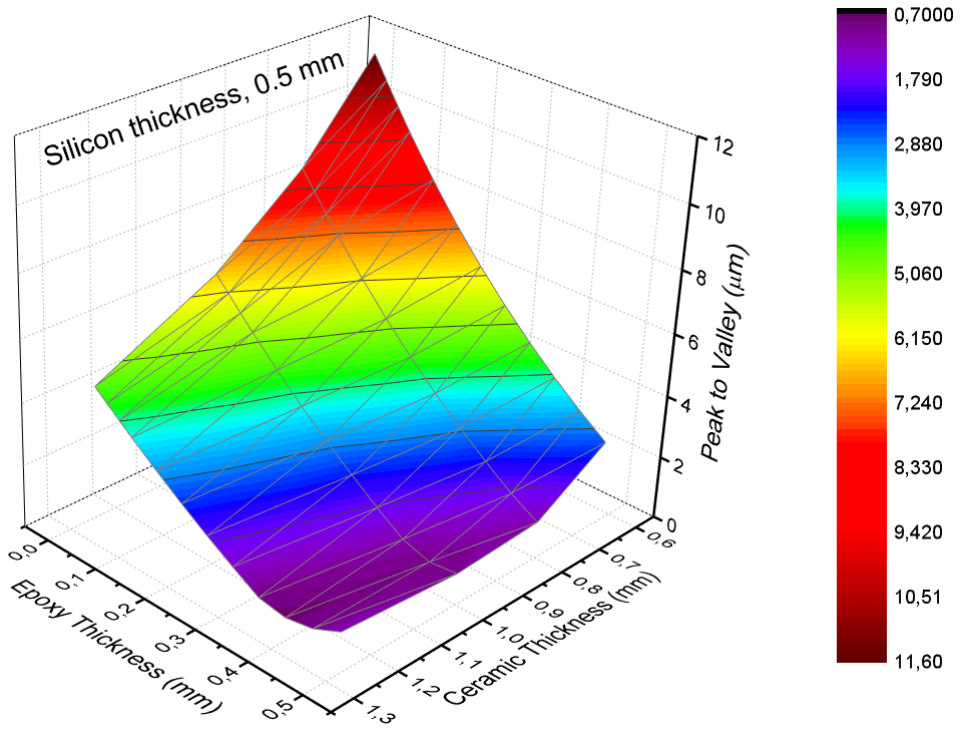

Figure 2.11: Warpage behavior of silicon, $t_{silicon}$ = 0.5 mm

A maximum warpage value of 11.597 μm has been obtained with 0.63 mm ceramic, 0.025 mm epoxy and 0.5 mm silicon thickness. Between these two extremes, when the epoxy thickness is 0.025 mm and the ceramic thickness increases, the warpage decreases. When the ceramic thickness is kept constant at 0.63 mm and the epoxy thickness increased, the warpage in this case also decreases. There exists a continuous behavior of warpage between the extremes. The peak to valley values in Figure 2.11 refers to the warpage of silicon.

The best three and worst three cases of warpage are given in Table 2.2. According to the results, the ceramic thickness is a key parameter affecting the warpage of 0.5 mm thick silicon. All of the low warpage cases contain 1.27 mm thick ceramic which is the thickest among the four ceramic thickness values whereas all of the high warpage cases include 0.63 mm thick ceramic, the thinnest value investigated.

The epoxy thickness is another critical parameter that affects the warpage of silicon. For the mentioned trimaterial assembly, the maximum warpage is observed with a very thin layer of epoxy. However, when epoxy thickness is increased without changing the ceramic thickness, warpage decreases as it is observed from Figure 2.11.

Table2.2: Highest and lowest warpage cases of 0.5 mm thick silicon

$t_{\mathbf{ceramic}}$ **(mm)**	$t_{\mathbf{epoxy}}$ **(mm)**	**PV** (μ**m**)
1.27	0.40	0.747
1.27	0.35	0.888
1.27	0.30	0.900
0.63	0.075	10.250
0.63	0.050	10.911
0.63	0.025	11.597

Moreover, as it is seen from Table 2.2 epoxy thickness can slightly affect the warpage behavior. The results show that the lowest warpage values for a particular silicon thicknesses can be achieved when the epoxy thickness is slightly smaller than defined silicon thickness.

2.3.2 0.4 mm silicon thickness

The procedure has been repeated for the constant silicon thickness of 0.4 mm. The same boundary conditions, material properties and thermal load as those for 0.5 mm thick silicon are used for this case. Analyses have been performed with the same ceramic and epoxy thicknesses which are used in the previous case. The general warpage characteristic is very similar to 0.5 mm thick silicon case. The maximum deflection occurs with a thin epoxy (0.025 mm) and thin ceramic (0.63 mm) which was also observed in previous case. The epoxy thickness effect is shown in Figure 2.12.

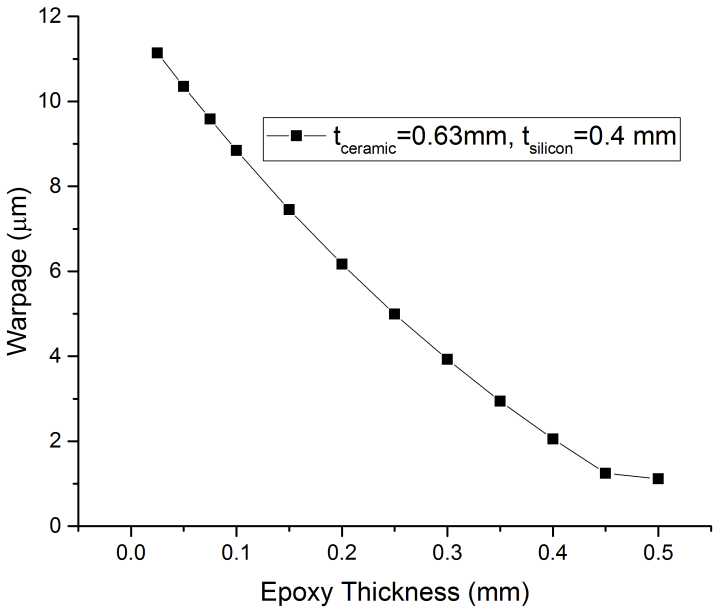

Figure 2.12: The effect of epoxy layer thickness on warpage of silicon, $t_{\text{silicon}} = 0.4$ mm

According to the FEA, the epoxy thickness is an important parameter to control the warpage of silicon. To observe this effect, the epoxy thickness should be controlled precisely during experiments.

The minimum deflection of 0.621 μm has been analyzed for 1.27 mm thick ceramic and 0.3 mm thick epoxy layers.

Table2.3: Highest and lowest warpage cases of 0.4 mm thick silicon

$t_{\mathbf{ceramic}}$ **(mm)**	$t_{\mathbf{epoxy}}$ **(mm)**	**PV** (μ**m**)
0.63	0.025	11.137
0.63	0.050	10.351
0.63	0.075	9.586
1.00	0.350	0.707
1.27	0.350	0.699
1.27	0.300	0.621

The results of the parametric analyses for 0.4 mm thick silicon warpage are given in Figure 2.13. According to this figure and Table 2.3, the minimum warpage for a 1.27 mm thick ceramic exists for 0.30 mm and 0.35 mm thick epoxy layer. If epoxy thickness is decreased below 0.3 mm or further increased, the warpage tends to increase. When ceramic thickness is equal to 1.00 mm, the minimum warpage occurs when the epoxy thickness is 0.35 mm.

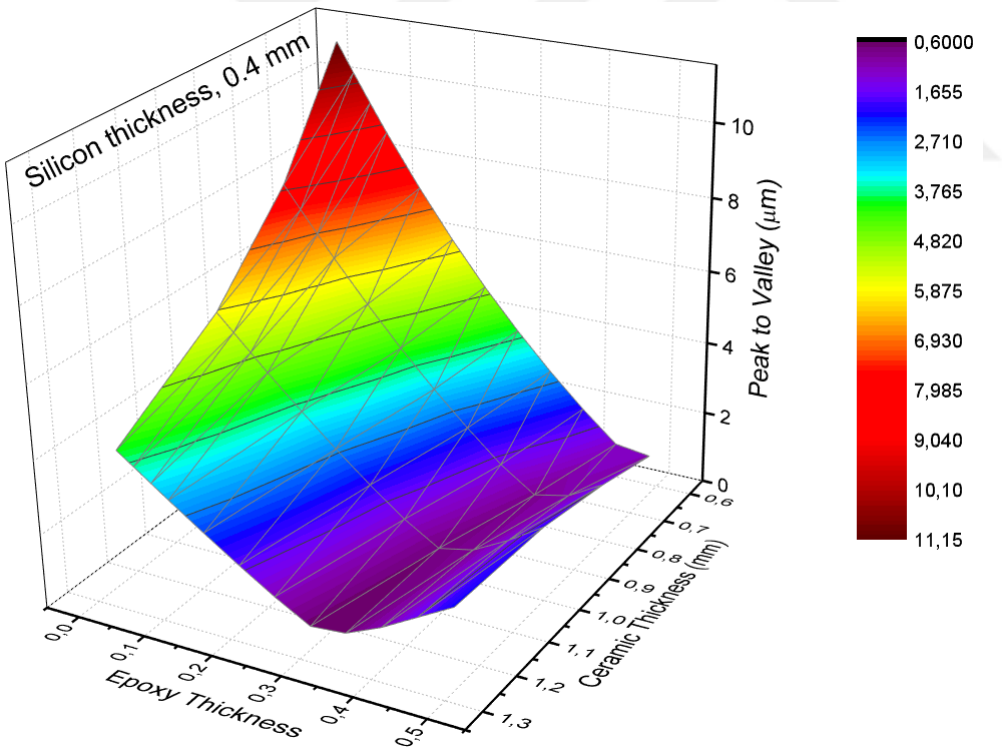

Figure 2.13: Warpage behavior of silicon, $t_{silicon}$ = 0.4 mm

2.3.3 0.3 mm silicon thickness

Although the silicon thicknesses are different, the maximum warpage of silicon is observed by using thin ceramic and thin epoxy layers, just as in the 0.4 mm and 0.5 mm thick silicon cases. The local maximum and minimum of silicon warpage in this case is obtained as 9.903 μm and 0.487 μm, respectively. The highest and lowest warpage cases of this section is given in Table 2.4

Table2.4: Highest and lowest warpage cases of 0.3 mm thick silicon

t_{ceramic} (mm)	t_{epoxy} (mm)	PV (μm)
0.63	0.025	9.903
0.63	0.050	9.003
0.63	0.075	8.116
0.80	0.300	0.625
1.00	0.250	0.586
1.27	0.250	0.487

The full field warpage behavior is also given in Figure 2.14. In this figure, there exists a valley for a medium thickness (0.25 - 0.30 mm) of the epoxy layer. For lower and higher epoxy thicknesses, the warpage of the silicon increases.

2.3.4 0.2 mm silicon thickness

A similar parametric analysis has also been performed for the 0.2 mm thick silicon material. The effects of epoxy and ceramic thickness have been analysed. For this case, the warpage graph stands like a valley as it is observed from Figure 2.15.

Although there exists a local maximum deflection for 0.025 mm thick epoxy and 0.63 mm thick ceramic, the global maximum deflection in the defined range is analysed for 0.5 mm thick epoxy and 0.63 mm thick ceramic. When the epoxy thickness is kept constant at these two values and the ceramic thickness is increased, there exists a decreasing trend in the warpage values (Figure 2.15).

The maximum and minimum warpage values of 0.2 mm thick silicon is given in Table

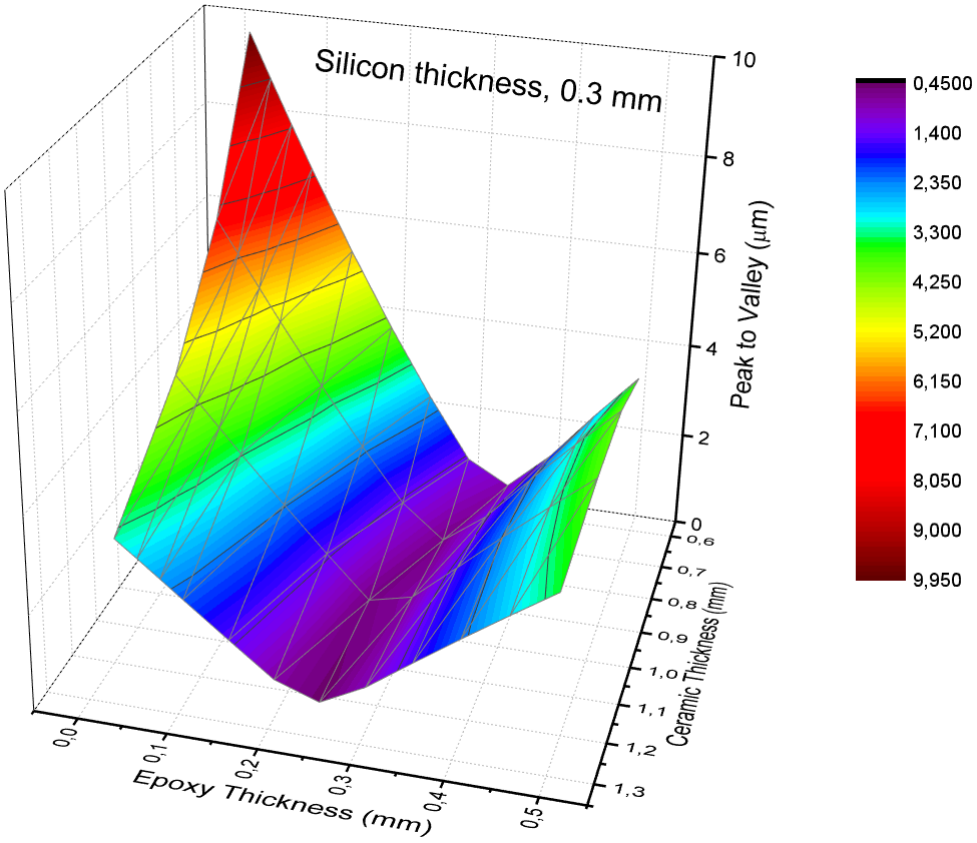

Figure 2.14: Warpage behavior of silicon, $t_{silicon}$ = 0.3 mm

2.5. A thin ceramic material integrated on 0.2 mm thick silicon by using a thick adhesive layer (0.45–0.50 mm) results in high warpage value for this case. According to the minimum warpage values of Table 2.5, it is possible to achieve very low warpage by using relatively thin ceramic and epoxy layers. Moreover, unlike the previous cases, having very thick epoxy layer dramatically increases warpage value of 0.2 mm thick silicon.

Table2.5: Highest and lowest warpage cases of 0.2 mm thick silicon

$t_{\mathbf{ceramic}}$ **(mm)**	$t_{\mathbf{epoxy}}$ **(mm)**	**PV** (μm)
0.63	0.500	9.127
0.80	0.500	8.002
0.63	0.450	7.883
0.80	0.200	0.573
0.63	0.200	0.420
1.27	0.150	0.253

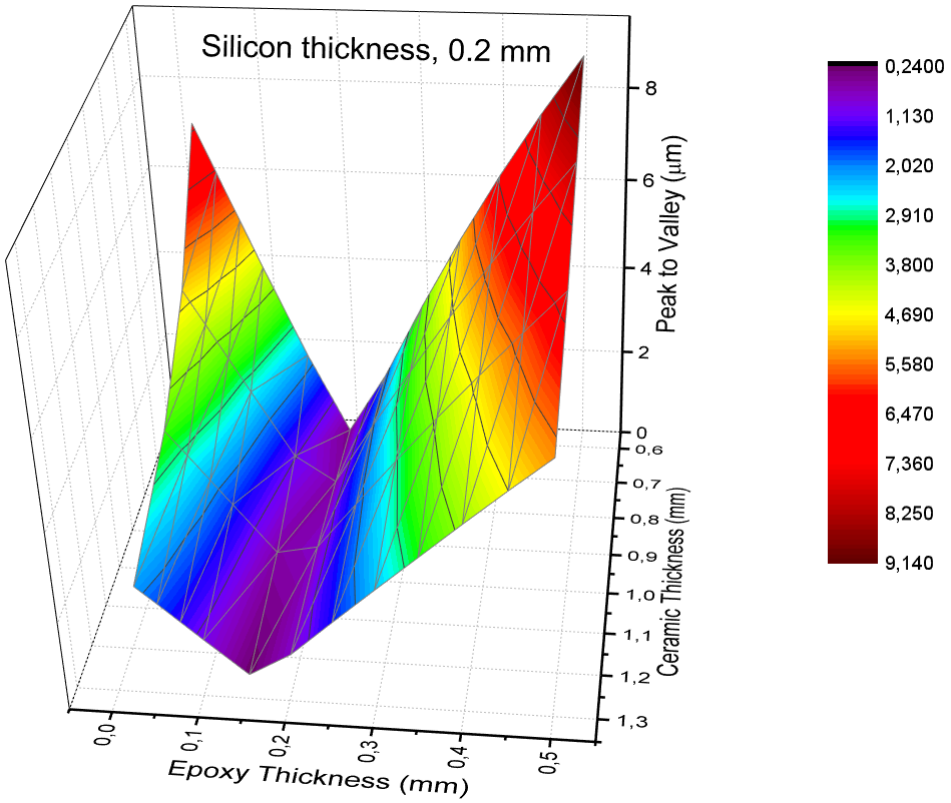

Figure 2.15: Warpage behavior of silicon, $t_{\text{silicon}} = 0.2$ mm

2.3.5 0.1 mm silicon thickness

The thinnest silicon material is defined as 0.1 mm. Even if obtaining such thickness of silicon in real life is not a trivial task, the FEA have also been performed for this case. Just like the 0.2 mm thick silicon case, the maximum warpage value (20.595 μm in this case) is observed when 0.63 mm thick ceramic and 0.5 mm thick epoxy layer is used (Table 2.6).

Table2.6: Highest and lowest warpage cases of 0.1 mm thick silicon

t_{ceramic} (mm)	t_{epoxy} (mm)	PV (μm)
0.63	0.500	20.595
0.63	0.450	18.613
0.63	0.400	16.465
0.80	0.075	0.371
1.00	0.075	0.181
1.27	0.075	0.134

A global minimum warpage value of 0.134 μm has been observed in this case by using a 1.27 mm thick ceramic and a 0.075 mm thick epoxy layers. For the same epoxy and silicon thickness as the ceramic thickness increases, the warpage decreases.

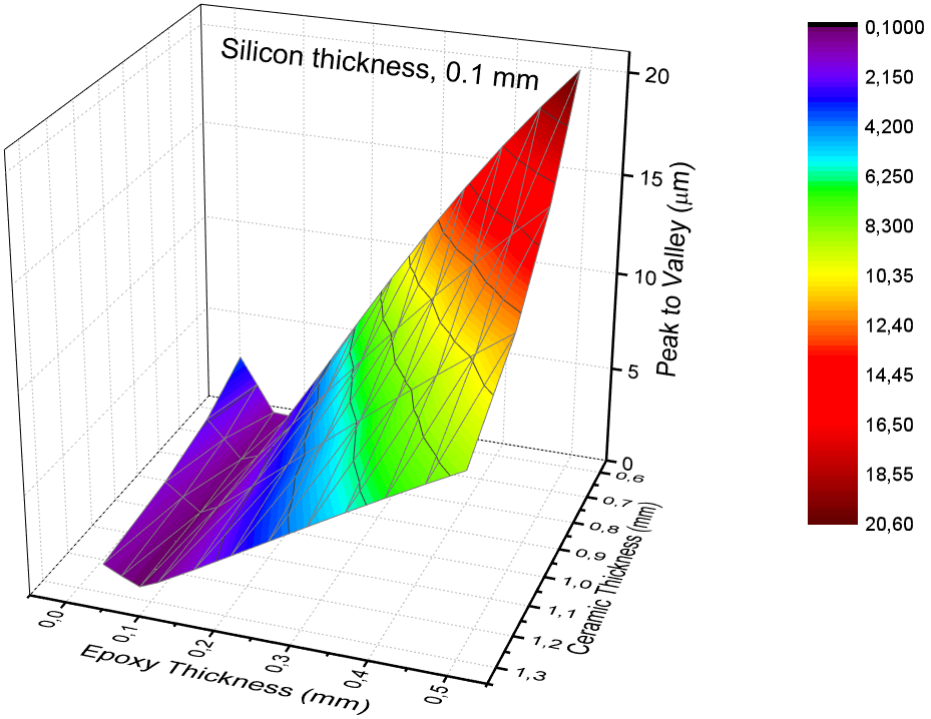

Figure 2.16: Warpage behavior of silicon, $t_{\text{silicon}} = 0.1$ mm

For minimum warpage, obtaining 0.075 mm thick epoxy layer seems feasible. However, the thinning process of silicon material down to 0.1 mm thickness is a challenging task. The handling and integration process of such a thin silicon layer might be another issue. If the silicon can be thinned to 0.1 mm and successfully integrated on the ceramic, the global minimum deflection value which is observed in the FEA can also be observed experimentally.

The deflection behavior of silicon is analysed for totally 240 different cases. In reality, obtaining some of these cases might not be easy under current production and integration methods and processes. The main aim of this study is to define the warpage behavior of both currently producable and not producable integrated structures. During selection of samples for experiments, the production capabilities as well as results of FEA will be taken into account, as detailed in Chapter 4.

In addition to the performed parametric analysis, a critical thickness ratio between the silicon and ceramic layers in terms of warpage has been analysed. The defined material thickness for silicon is in the range of 0.1 mm to 0.50 mm whereas the ceramic thickness is in the range of 0.6 mm to 3.4 mm. According to defined matrix, thickness ratio ($TR = \frac{t_{\text{ceramic}}}{t_{\text{silicon}}}$) values between 1.07 and 33.94 have been covered in these analyses. The main goal of these analyses is to observe a particular or critical thickness ratio for predefined values of individual layer thicknesses. The full field critical thickness ratio results are provided in Figure 2.17. For all the critical thickness ratio analyses, the uniform epoxy material thickness is defined as 0.05 mm

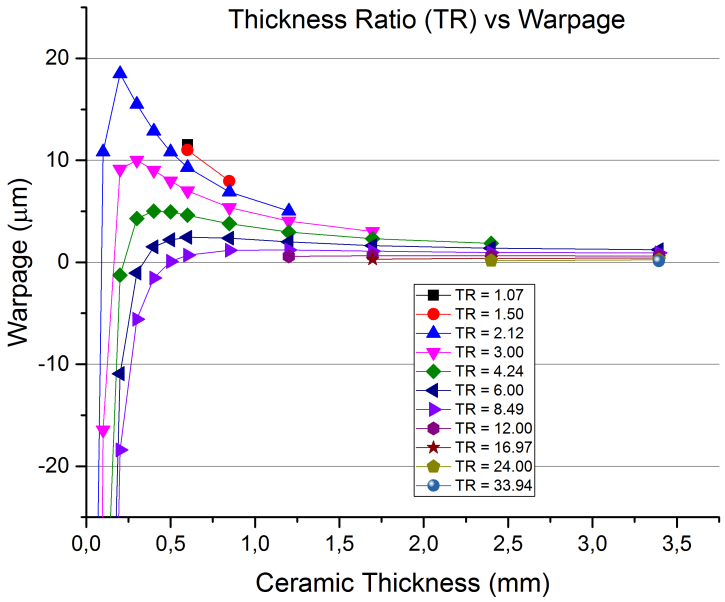

Figure 2.17: Critical thickness ratio, $TR = \frac{t_{\text{ceramic}}}{t_{\text{silicon}}}$

For low thickness ratios ($TR \leq 6.00$), there exist a maximum warpage at around 0.25 mm thick ceramic layer. For a constant thickness ratio, further decreasing of ceramic thickness results in dramatically decreasing warpage to negative values. The minus sign indicates that surface profile has changed from convex to concave or concave to convex. Obtaining high thickness ratios ($TR > 8.49$) with thick ceramic material ($t_{\text{ceramic}} > 1.00$ mm) results in stable and very low warpage values.

Generally, a ceramic layer thickness between 0.5 mm to 3.0 mm can be appropriate for cold region design. A closer look for low warpage cases ($w < 10$ μm) is given in Figure

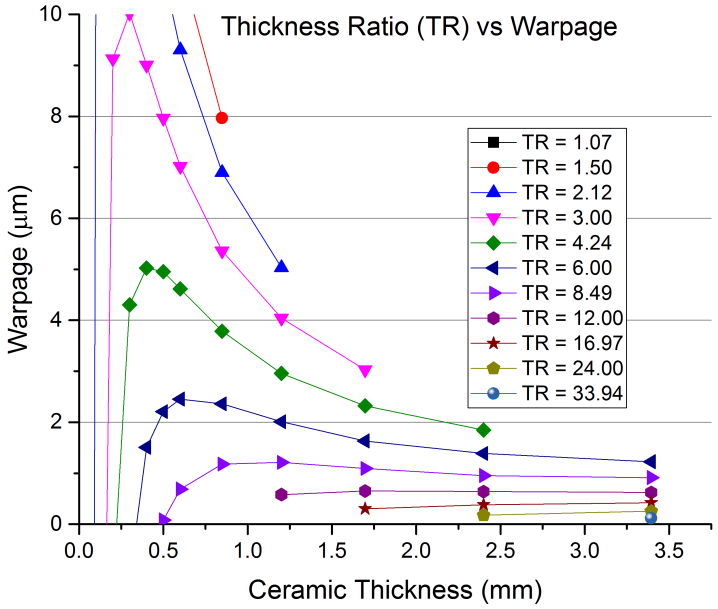

Figure 2.18: A closer look for critical thickness ratio, $TR = \frac{t_{\text{ceramic}}}{t_{\text{silicon}}}$

2.18. A high thickness ratio indicates that the silicon material should be excessively thinned which may result in activation of different failure mechanisms caused by the thinning process of material [4]. According to the FEA results represented in Figure 2.18, having a thickness ratio greater than 8.49 results in less than 1 μm warpage. When a low thickness ratio is chosen such as 2.12, the warpage may increase up to 18.5 μm.

In Figure 2.19, the effect of silicon thickness on warpage is clearly seen. These results are for 0.05 mm thick epoxy layer. Three different thicknesses of the ceramic have been considered in this figure. According to the FEA results, decreasing silicon thickness decreases the warpage for all ceramic thicknesses. If the silicon material is thinned beyond 0.06 mm, its deflection behavior changes and the warpage results move towards negative values. At a given silicon thickness, increasing the ceramic thickness results in a decrease in the warpage value.

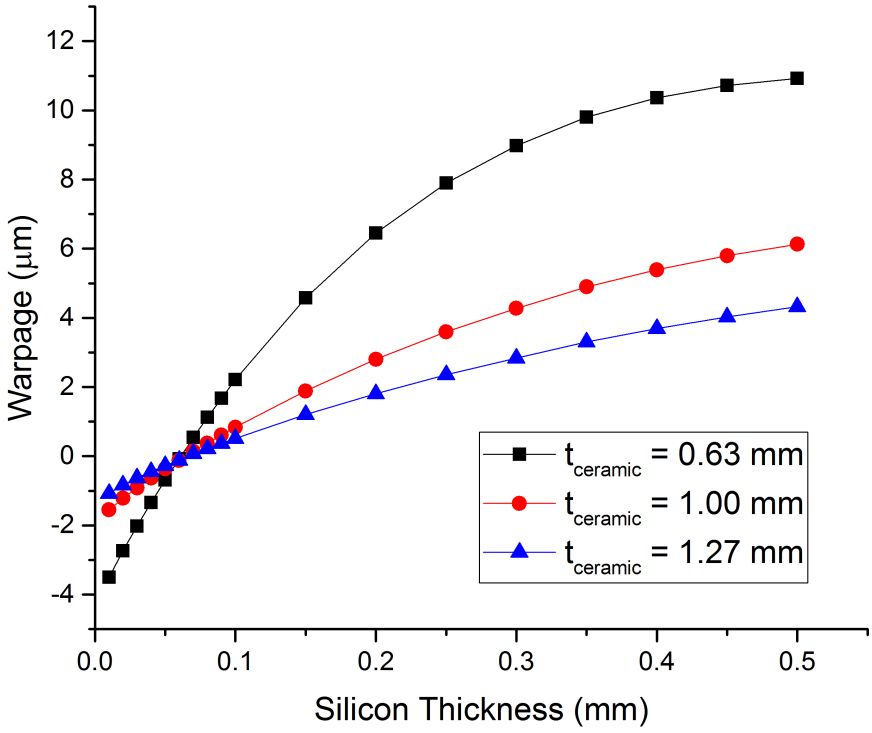

Figure 2.19: The effect of the silicon thickness on warpage

CHAPTER 3

TEST SETUP

In the first section of this chapter, the measurement method is explained. To measure the out of plane deformations of the silicon, two different setup designs have been prepared. The features, advantages and disadvantages of these two designs have been stated. Possible measurement error sources have been defined for both designs and the contribution of each individual error source has been determined both experimentally and numerically. To utilize any test setup, possible measurement error sources must first be determined. Moreover, the effect of investigated parameters on warpage measurements should be analysed before starting experimental studies so that one can specify the error margin of experimental results caused by the test setup.

3.1 Test Method

Warpage was defined in Chapter 2 as the vertical displacement difference on a surface between maximum and minimum displacement points (Figure 3.1). In addition to the FEA described in Chapter 2, experimental studies have also been performed to obtain a test sample design leading to minimum warpage. The proper test setup should employ a non-contact method. Because the sample which will be tested stays in vacuum environment and it is enveloped by metal parts. So, using contact measurement method to define warpage behavior of the sample may not be useful. Interferometric measurement methods meet this expectation.

For this purpose, a phase shifting Fizeau laser interferometer system has been used to measure surface deformations at cryogenic temperatures as well as at room temperature.

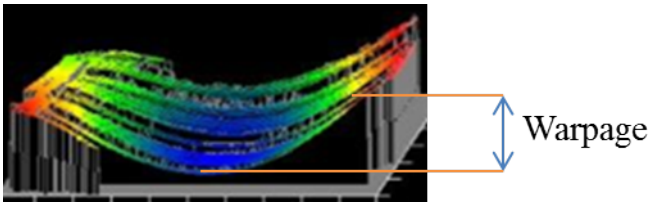

Figure 3.1: Representation of warpage

Representation of warpage using the employed interferometer is given in Figure 3.2. In phase shifting Fizeau laser interferometer system, a 632.8 nm wavelength He – Ne laser is used.

As illustrated in Figure 3.2, from the laser source, the He – Ne laser goes through

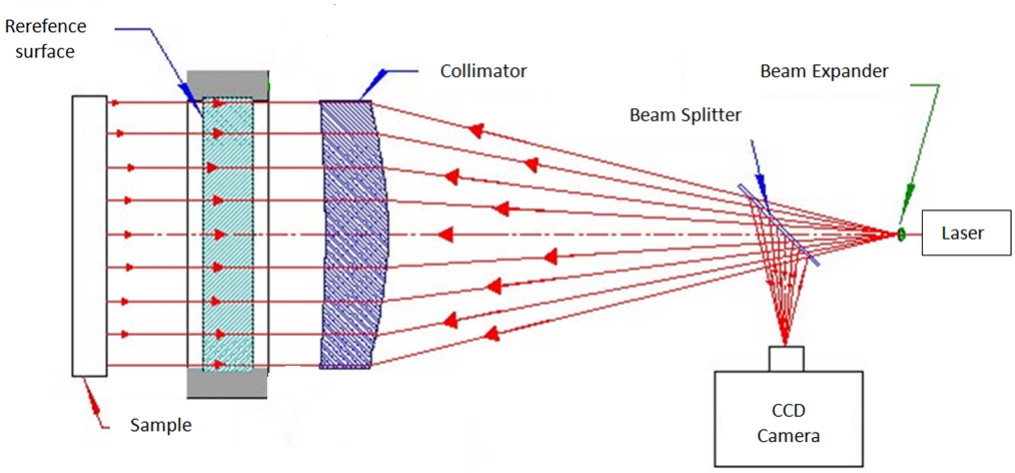

Figure 3.2: Phase shifting Fizeau laser interferometer system

a beam splitter and using a collimator, the laser beams are aligned. A part of the laser beam is reflected from the reference surface whereas the remaining part gets reflected from the sample surface. The reflected beams from the reference surface and the sample come back through the collimator and a portion of them get reflected via the beam splitter. The laser beams reflected from the reference surface and the sample are collected at CCD camera. Two reflected laser beams interfere at the CCD camera. As a result of this interference, an interference pattern occurs. In the interferometer, a piezo phase shifter is used which simply is a piezo transducer which moves the reference surface slightly. As a consequence of this movement, fringe pattern slightly changes. When the interferometer software processes this movement, peaks and valleys on the measured area can be defined very precisely. A sample fringe pattern is presented in

Figure 3.3.

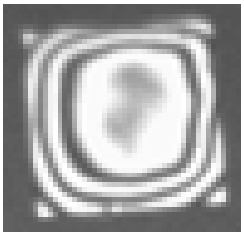

Figure 3.3: Fringe pattern

3.2 Test Setup Design

There are some common features that a warpage measurement test setup must have. First of all, the setup must have a vacuum chamber. Samples will be placed in it so that convection heat loss is minimized and achieving cryogenic temperatures is easier. Secondly, there must be an optical window so that 632.8 nm He - Ne laser can pass through it and reach the sample surface. A temperature feedback should be received from the cold region. This way, temperature dependent out of plane surface deformations can be analyzed. To transfer temperature data from the vacuum envelope to the outer environment, the test setup should have electrical feed through features. And finally, the test setup should be equipped with an interferometer, a phase shifting Fizeau laser interferometer.

3.2.1 First Design of Test Setup

In the first design of the test setup, a rotary type Stirling engine cryocooler has been used to achieve cryogenic temperatures. There is no need to use any cryogenic fluid while using a cryocooler. Moreover, controlling and stabilizing the sample temperature is easier when a cryocooler [8], [9] is used. Borosilicate glass (BK7) which has high transmittance (> 0.96) for 632.8 nm wavelength has been used as the optical window. A copper pumping tube has been utilized as the vacuum port. In the setup design, a turbo molecular pump and a dry pump equipped pumping station has been used to obtain vacuum inside the housing. The dry pump works as a backup pump and it satisfies the vacuum level inside the housing so that the turbo molecular pump can

start to operate. Viton o-ring material has been used in between metal parts to obtain vacuum integrity. Standart QF flange features have been used for metal parts which are o-ring sealed. Standart metal clamps have been used to hold metal parts together. Torr seal, an adhesive type material, which has a low elastic modulus has been used to integrate the optical window to the metal part. The assembly of this first setup is given in Figure 3.4. After the integration, He leak test is applied on the integrated structure. The He leak rate has been measured less than 10^{-8} mbar·lt/sec which is considered as hermetic sealing. The samples that will be tested are placed on a cold finger cap, named as Cold Head in Figure 3.4b. The temperature sensor which is placed on the sample surface is connected to electrical pads via wirebonds. Electrical pads are placed on a multilayer ceramic. There exist a few layers inside this ceramic which are used to connect electrical pads to the outer world pins. This way, signal transmittance from the sample to the outer world is realized.

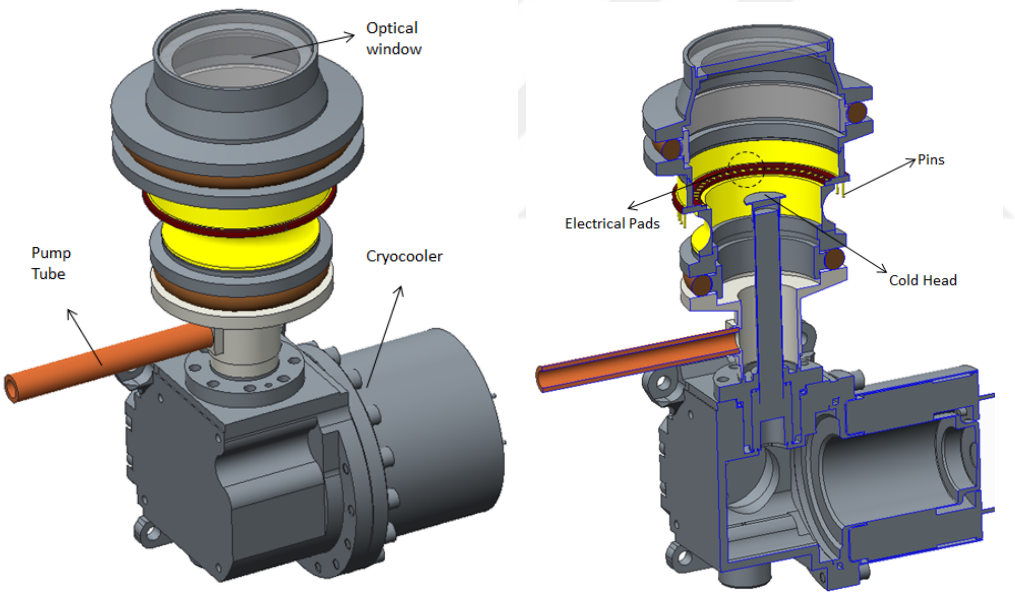

(a) Oriented view (b) Cross section view

Figure 3.4: First design of the test setup

Advantages of this setup can be defined as follows;

• Active temperature control of the sample by adjusting the cryocooler operating temperature

• Ease of sample mounting or dismounting obtained by using standart QF flanges and clamps

• Changing optical window, if needed, without disintegrating any other part

Although this first setup had several advantages, there existed a problem which may eliminate the advantages. It is the vibrational effects caused by active pumping and cryocooler's operating frequency itself. Mechanical vibrations can affect interferometer measurements and fringe pattern. Hence it may not be possible to obtain stable, reliable and repeatable results. Because of the probable effect of mechanical vibrations on interferometric measurements, a second design is utilized.

3.2.2 Second Design of Test Setup

Although the first design had good capabilities of temperature control and ease of sample integration, an alternative second design was needed to eliminate the mechanical vibrations caused by cryocooler operation and active pumping.

In the second design, liquid nitrogen has been used as the coolant. The usage of cryocooler has been eliminated so that mechanical vibrations caused by the cryocooler has been removed. In this case, there exists only the vibration caused by liquid nitrogen boiling which can be neglected. Moreover, the pumping tube has been replaced with special type of insert. The second design is illustrated in Figure 3.5. By using this equipment, it had been possible to dismount the turbo molecular pump hose from test setup interface without losing vacuum integrity in the envelope. The vibrations caused by active pumping could be eliminated by dismounting the vacuum interfaces after achieving the desired vacuum level inside the envelope.

The sample is placed on the cold head. The temperature sensor is placed on a ceramic which is placed on the cold head. There are electrical connections between the temperature sensor and pins on the cold head as well as cold head pins and feedthrough pins. The optical window on the aluminum plate is integrated via Torr seal material. O-ring sealing is used between the metal housing and aluminum plate. The integrated sample and the front view of the second design are given in Figure 3.6.

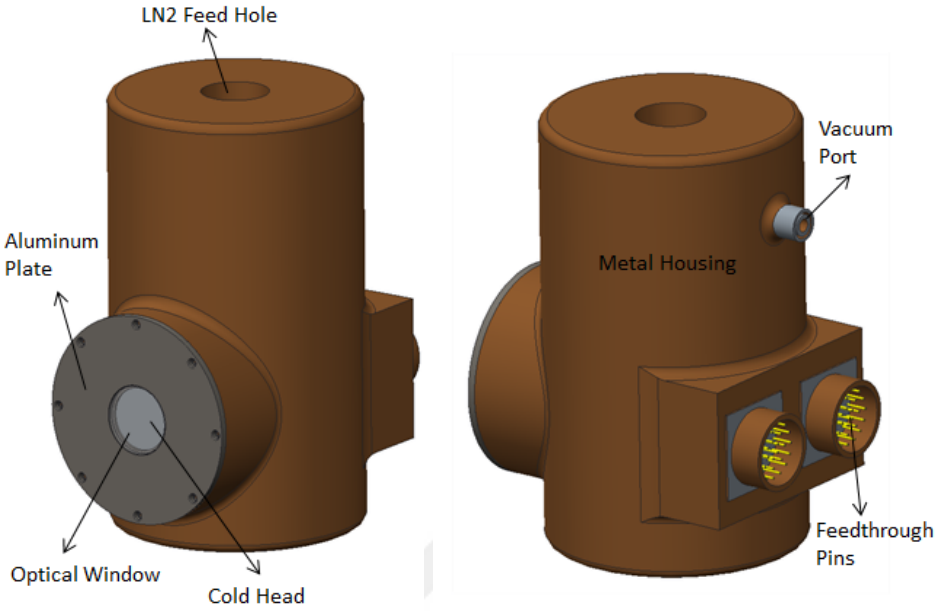

(a) Oriented view (b) Oriented view 2

Figure 3.5: Second design of the test setup

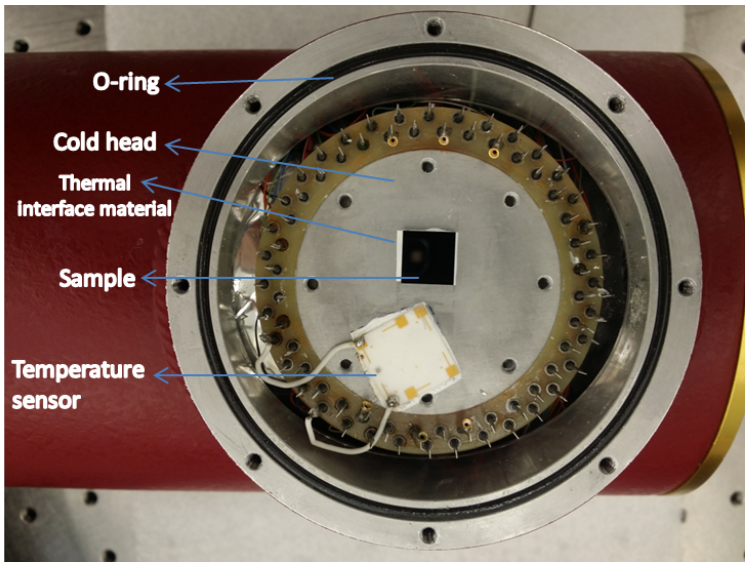

Figure 3.6: Test setup

3.2.3 Measurement Error Sources

As mentioned in the beginning of this chapter, the test setup is equipped with a phase shifting Fizeau laser interferometer system. Depending on the design of the test setup, there may be several possible error sources which can affect the measurement results. There exists an optical window for both designs. Introducing an extra layer on the optical path of the laser has some drawbacks, of course. Using a high transmittance optical flat at 632.8 nm wavelength is the first requirement to obtain surface topology data from sample. However, there are some error sources caused by the existence of the optical window. A total number of four reasons has been defined for possible measurement errors with such a test setup:

1. When the temperature of the sample is stabilized around 77 K, the effect of change in the optical path of the laser;
2. Effect of the surface topology of the optical window on warpage measurements of the sample;
3. Effect of optical window tilt angle;
4. Effect of the difference between the pressures on the top and bottom surfaces of the optical window;

The mentioned effects have been analyzed by experiments and numerical studies.

3.2.3.1 Effect of change in optical path, (Effect 1)

When the temperature of the cold region materials reaches a steady state value, BK7 optical window temperature changes mainly due to radiative heat transfer. The optical path of the laser also differs in response to change in the thickness of BK7 due to its decreasing temperature.

FEA has been performed to determine the effect of temperature change of the optical window for both designs. Then, the optical path lengths and optical path difference have been found.

For the first design of test setup, the geometry has been simplified. O ring connections have been eliminated and vacuum port has been excluded. Electrical pin connections have also been removed. Kovar which is a Fe-Ni-Co alloy has been used as outer

body material whereas the cold finger was made of stainless steel. BK7 which was the optical window material and a commercially available ceramic was defined as the carrier ceramic (Figure 3.7).

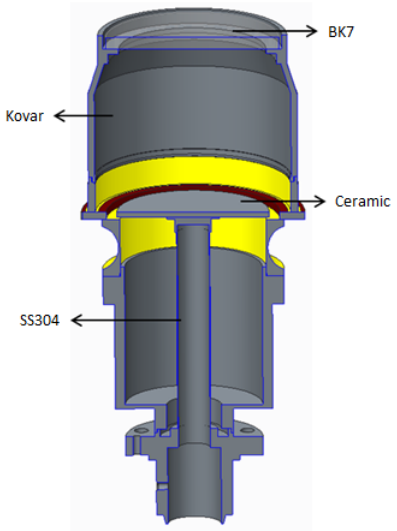

Figure 3.7: Simplified model of test setup 1

The boundary conditions on this structure have been defined as follows;

- Ceramic temperature, 77 K;
- Natural convection coefficient between the outer surfaces of the test setup and the ambient, 7 W/m^2K;
- Surface emissivity value for cold outer surfaces of SS304 cold finger, 0.3;
- Surface emissivity value of black ceramic, 0.85;
- Surface emissivity value of BK7 optical window, 0.80;
- Surface emissivity value of Kovar, 0.05;

Figure 3.8 illustrates the boundary conditions for the first design.

The optical path length is multiplication of the distance of light travels through the involved media, namely air, BK7 and vacuum and index of refraction of this medium.

The given optical path lengths (OPL_i and OPL_f) for the initial and final conditions, are respectively found as follows;

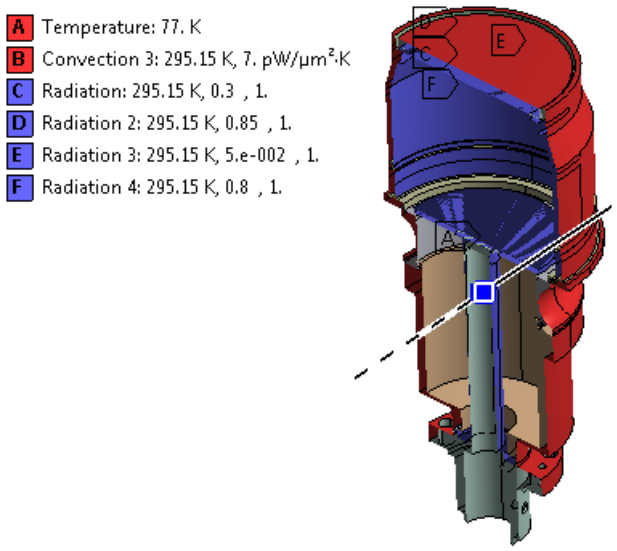

Figure 3.8: Boundary conditions for the first design

$$(OPL)_i = n_{\text{air}}\, L_{\text{air}} + n_{\text{BK7}}\, t_{\text{BK7}} + n_{\text{vacuum}}\, L_{\text{vacuum}} \tag{3.1}$$

$$(OPL)_f = n_{\text{air}}\, (L_{\text{air}} + x) + n_{\text{BK7}}\, (t_{\text{BK7}} - x) + n_{\text{vacuum}}\, L_{\text{vacuum}} \tag{3.2}$$

where n_{air}, n_{BK7}, n_{vacuum}, are the refractive indices of air, optical window and vacuum, respectively; L_{air}, t_{BK7} and L_{vacuum} are the respective lengths of the three media. The change in the medium length due to contraction of the optical window is shown by x. When the cryogenic temperatures are achieved, the optical window also cools down. Because of this temperature difference on the BK7 optical window, it contracts. Hence, the thickness of the BK7 window is lowered with an amount of x whereas the distance travelled by the laser in air increases with the same amount.

The optical path difference is the difference between the two optical path values;

$$\text{OPD} = (OPL)_f - (OPL)_i = x\,(n_{air} - n_{BK7}) \tag{3.3}$$

where $n_{air} = 1.00027$ and can be approximated as 1 and $n_{BK7} = 1.515$, so

$$\text{OPD} = 0.515\, x \tag{3.4}$$

and x depends on how much BK7 window contracts due to the exposed temperature difference, ΔT. Please note that refractive index for air is given as 1.00027 whereas it

is 1.00 for vacuum. Hence, the refractive index difference between air and vacuum can be neglected.

The FEA results on the first design indicated maximum and minimum temperatures of 292.05 K and 289.79 K, respectively, for the optical window. The temperature distribution is shown in Figure 3.9.

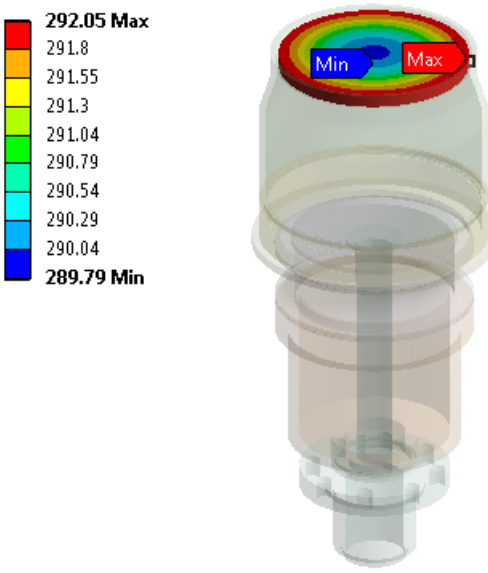

Figure 3.9: Optical window temperature distribution for the first test setup

The mentioned analysis has been performed with 1000 μm optical window mesh size. The mesh sensitivity of BK7 temperature is given in Figure 3.10. A total number of 34186 elements and 107141 nodes have been used in this FEA.

The initial temperature has been defined as 295.15 K, and the average temperature at the final state is 290.92 K, so there exists 4.23 K difference on optical window temperature between the initial state and the final state. This temperature difference yields a contraction of BK7 window with an amount of

$$\begin{aligned} x &= \alpha\, t_{\mathrm{BK7}}\, \Delta T \\ x &= 7.1 \times 10^{-6}\, \frac{1}{K}\, \times 2.35 \times 10^{-3}\,\mathrm{m}\, \times 4.23\,\mathrm{K} \\ x &= 70.6 \times 10^{-9}\,\mathrm{m} = \ 70.6\,\mathrm{nm} \end{aligned} \tag{3.5}$$

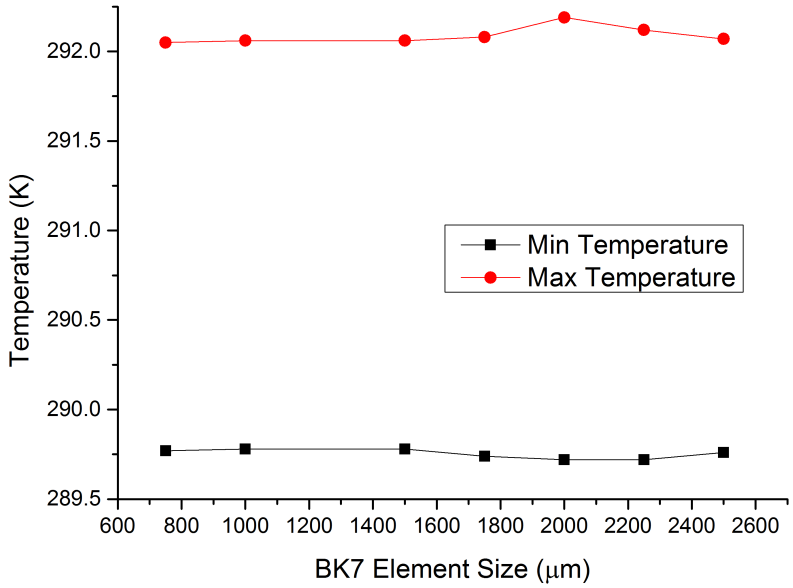

Figure 3.10: BK7 mesh sensitivity of temperature output

From equation 3.4 optical path difference is found as

$$OPD = 0.515x = 36.4\,\text{nm} \tag{3.6}$$

The same procedure is also followed for the second design of the test setup in the end of this section.

3.2.3.2 Effect of surface topology of optical window, (Effect 2)

Manufacturing process based surface finish of the optical window may affect the measurement results slightly. To determine the contribution of this effect on measurement results, an experiment has been performed. The test structure is given in Figures 3.11 and 3.12. In Figure 3.11, diced silicon piece is integrated on ceramic by using epoxy material. BK7 optical window is integrated on Kovar part by using an adhesive material.

In the experiments, the surface topology of the silicon sample has been measured for four different orientations of the optical window. Before each measurement, the optical window has been rotated clockwise with 90° steps. Surface topology characteristics

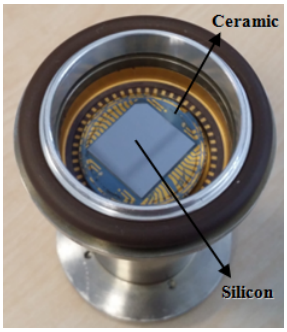

Figure 3.11: Test structure for testing optical window effect,top view

of the silicon and deflection difference between the maximum and minimum points on a vertical axis have been compared. In all of the measurements, characteristic of the deformed silicon surface has been found the same.

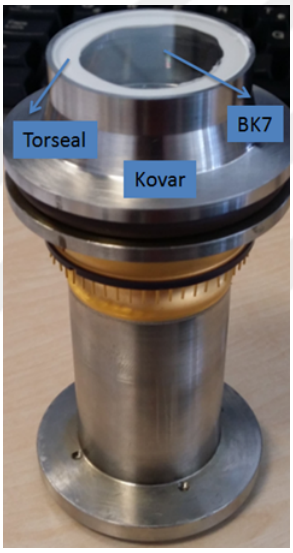

Figure 3.12: Test structure for testing optical window effect,side view

According to Table 3.1 there exists 27.2 nm difference of PV values in between these four measurements. The PV values do not increase or decrease in sequence with rotation. The main aim in this subsection was to observe the optical window topology effect on the sample by conducting multiple measurements.

Table3.1: PV values for different orientations of the optical window

Optical Window Orientation	Peak to Valley (nm)
0°	1847.4
90°	1863.2
180°	1844.6
270°	1836.0

3.2.3.3 Effect of optical window tilt angle, (Effect 3)

Although BK7 glass has a high transmittance (> 96%) at 633 nm wavelength, a fraction of incoming light is reflected. To prevent the measurement of the reflected light by the CCD camera, the optical window has been tilted with angles of 2° and 5° as shown in Figure 3.13. In addition to horizontal optical window measurements, the deflection of the same silicon sample has been measured with these two tilted orientations of the optical window.

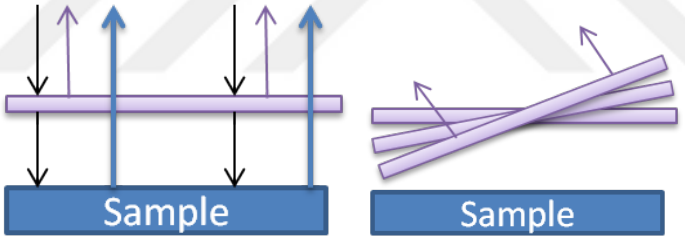

(a) Horizontal optical window (b) Tilted optical windows

Figure 3.13: Optical window positions

Table 3.2 represents the effect of optical window tilt angle on warpage measurements.

Table3.2: PV results for different tilt angles of optical flat

	Flat Optical Window	2° tilt	5° tilt
PV (μm)	1.09 ±0.01	1.06 ±0.01	1.06 ±0.01

When the sample is investigated without an optical window, the PV value is found as 1.13 ± 0.01 μm. Then, the optical window is integrated in the setup in horizontal orientation and the PV value is measured as 1.09 μm, on the other hand, the same

PV value of 1.06 μm has been measured for 2° and 5° tilted orientations of the optical window. Hence, a significant difference has not been observed between these three measurements. In all three cases, the surface deformation characteristics are also the same as observed from Figure 3.14. In the end of these experiments, it has been concluded that the tilt angle of optical window did not have a substantial effect for 2° and 5° tilt angles. Between the horizontal and tilted optical window orientations, a 30 nm measurement difference has been observed. The PV value of the horizontal optical window yielded slightly lower PV value than the case with no optical window.

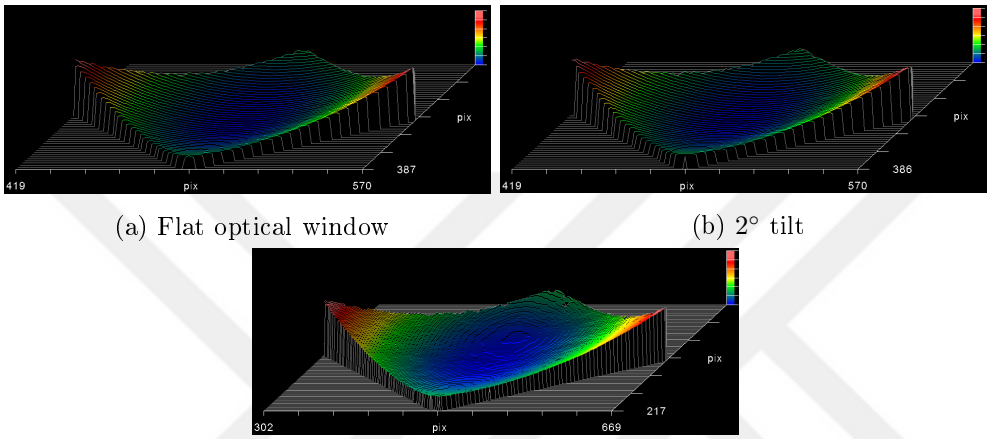

(a) Flat optical window (b) 2° tilt

(c) 5° tilt

Figure 3.14: Warpage characteristics of different orientations of optical window

3.2.3.4 Effect of different pressures on top and bottom surfaces of optical window, (Effect 4)

To achieve cryogenic temperatures, the sample is placed in vacuum environment. There exists a difference between the pressures exerted on the bottom and top surfaces of optical window which bends the optical window slightly. This effect is illustrated in Figure 3.15. Because of the bending, the measurement results can be affected. The effect of the bending of the optical window on warpage has been determined by performing another experiment. In this experiment, two measurements have been taken using the same sample. During the first measurement, the chamber was under atmospheric pressure and the second measurement is taken under vacuum. The vacuum level during the second measurement was less than 1 mTorr.

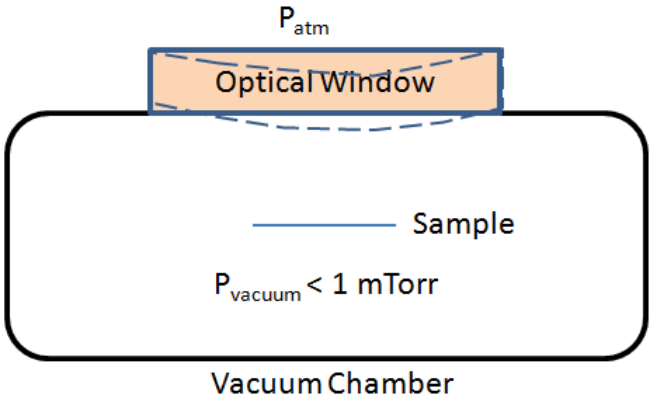

Figure 3.15: Pressure difference on optical window

Between these two measurements, the PV values differ from each other by an amount of 65.5 nm. The surface deformation characteristics did not change because of the pressure change on optical window.

3.2.3.5 Overall assessment of measurement error sources

For the first design of the test setup, the effects of defined four parameters on warpage measurements have been investigated by experiments and FEA. The measurement error caused by the optical path difference has been determined to be 36.4 nm whereas the optical window surface topology caused 27.2 nm measurement difference. Adding a horizontal optical window introduced 40 nm measurement difference whereas 2° and 5° tilted orientations caused approximately 70 nm PV difference with respect to the no optical window case. Finally, the difference between the pressures on the top and bottom surfaces of the optical window caused 65.5 nm PV difference.

The mentioned results are presented for test setup design 1. However, the error caused by the optical window tilt angle and the surface topology are essentially the same for both design 1 and design 2, as these effects are independent from the setup design.
In the second design, firstly, the effect of different pressures on each side of the optical window on warpage has been re-evaluated. For this purpose, BK7 glass material has been mounted on an aluminum part by using a commercial, vacuum use epoxy, as it was the case for the first design. Although the surface deformation characteristics was the same for vacuum and ambient pressure environments, there existed 15 nm

measurement difference on the PV value of the same sample between atmospheric pressure and vacuum environment (< 1 mTorr).

Secondly, the effect of the optical path difference in the second design which is different than that for the first design has been assessed. The temperature distribution on the optical window will probably be different because of the totally different geometry of the second design of test setup compared to the first one. This difference results in different heat fluxes through the components so that the steady state temperatures of the corresponding optical windows will differ. To determine the temperature difference between the initial and final states of the optical window, a FEA has been performed for the second design of the test setup.

In this new design, the geometry has also been simplified. The o ring connections have been eliminated and the vacuum port and the electrical connection pin details have also been excluded (Figure 3.16).

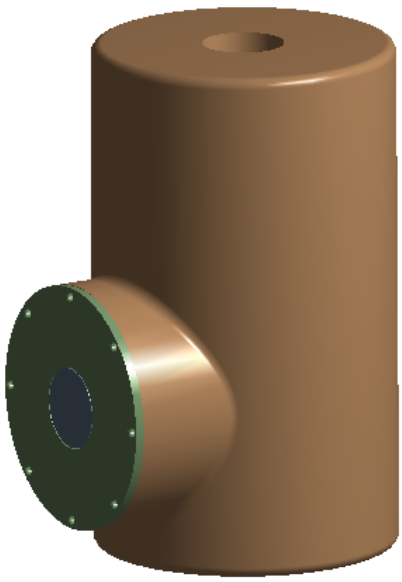

Figure 3.16: Simplified model of test setup 2

The boundary conditions defined for this structure are as follows:

• Cold head temperature at the final state, 77 K

• Natural convection coefficient between the outer surfaces of the test setup and the ambient, 7 W/m^2K

• Surface emissivity value for cold outer surfaces of liquid nitrogen inlet pipe which is coated by a multi layer insulation material (MLI), 0.005

- Surface emissivity value of BK7 optical window, 0.80
- Surface emissivity value of stainless steel (SS304) vacuum envelope body, 0.3

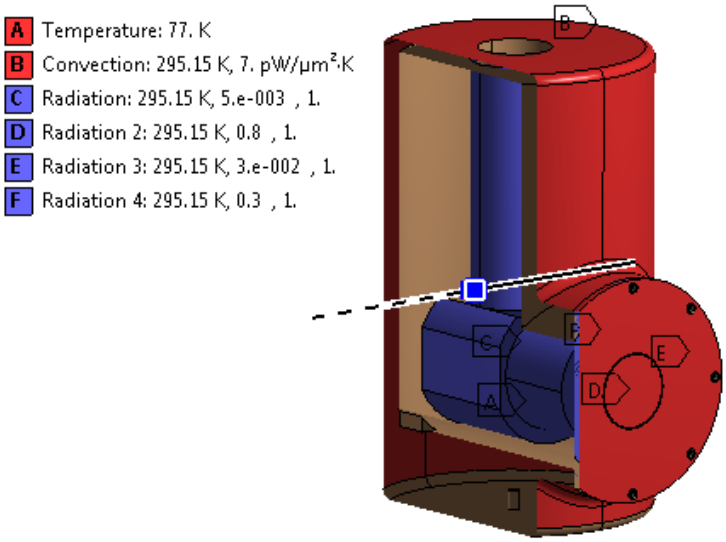

Figure 3.17: Boundary conditions for the second design of test setup

The temperature distribution on the optical window is given in Figure 3.18.

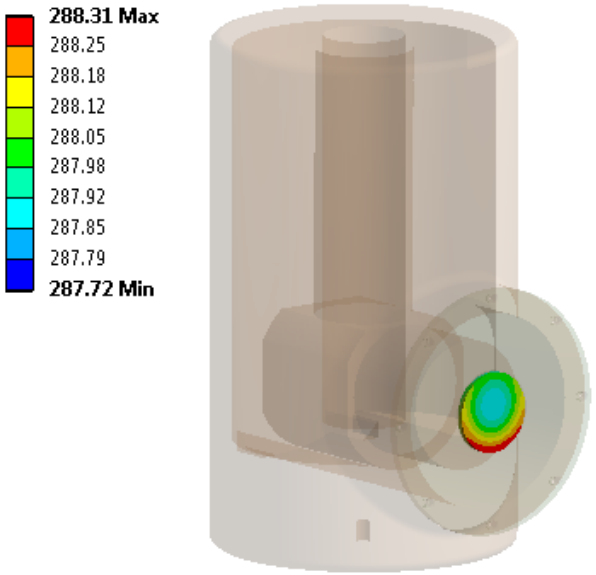

Figure 3.18: Temperature distribution on optical window for the second design

According to FEA, the maximum and minimum temperatures on optical window oc-

cured to be 288.31 K and 287.72 K , respectively. So an average temperature of BK7 at steady state has been found as 288.02 K which means that there exists 7.13 K temperature difference between the initial and final states of BK7. The contraction of the optical window due to this difference is

$$x = \alpha\, t_{\mathrm{BK7}}\, \Delta T \tag{3.7}$$

$$= 7.1 \times 10^{-6} \frac{1}{K} \times 2.35 \times 10^{-3}\,\mathrm{m} \times 7.13\,\mathrm{K} \tag{3.8}$$

$$x = 118.96 \times 10^{-9}\,\mathrm{m} = 118.96\,\mathrm{nm} \tag{3.9}$$

and the optical path difference caused by this contraction is found from equation 3.4,

$$\mathrm{OPD} = 0.515x = 61.3\,\mathrm{nm} \tag{3.10}$$

The found error values are listed in Table 3.3. The surface topology and the tilt angle effects of the optical window did not differ from the first design in the second design (see effect 2 and 3 in Table 3.3). The optical path change effect, effect 1 in Table 3.3, is larger for the second design because of the greater temperature difference on the optical window for this case. However, the pressure difference effect is less for the second design. A measurement difference of 15.0 nm has been obtained for the second design whereas it was 65.0 nm for the first design. It should be remembered that during experimental measurements the first measurement is taken at room temperature by using a horizontal optical window and under satisfied vacuum conditions of the chamber. The final measurement is taken under same conditions but at 80 K. The warpage difference between the room temperature and 80 K has been used as the experimental output. Hence, the effect numbers 2, 3 and 4 exist both for the measurements at room temperature and 80 K. Only the optical path change effect exists between the initial and the final measurements.

Table3.3: Error contributions of each effect for the two setup designs

Effect No	Setup 1	Setup 2
Effect 1	36.4 nm	61.3 nm
Effect 2	27.2 nm	27.2 nm
Effect 3	30.0 nm	30.0 nm
Effect 4	65.5 nm	15.0 nm

It is important to note that there are also interactions between these four effects in reality. For example, the optical window bends at first because of pressure difference on inner and outer surfaces of it (effect 4). Then, changing optical window temperature mainly because of the radiative heat transfer results in optical path change (effect 1). Fortunately, the influence of these combined effects on warpage is much smaller than individual influences of each effect. Hence, the combined effects has not been determined as quantitatively.

CHAPTER 4

EXPERIMENTAL STUDIES

4.1 Experimental Procedure

As a result of the FEA, the most and least promising trimaterial samples have been identified for further investigation. During selection of trimaterial assembly structure, the fabrication process capabilities have also been taken into account. These samples have been fabricated and experimentally tested. A comparison of the experimental results with those obtained by FEA has been made.

For the experiments, establishing a clear experimental procedure and sample preparation steps are vital. In this chapter, this procedure and preparation steps are provided. Experimental results for eight different samples are presented. Moreover, some process effects on warpage are discussed at the end of this chapter.

4.1.1 Preparation of trimaterial assembly

In this section, the construction of integrated assembly structures is described. The layer thicknesses of the trimaterial assembly are defined in accordance with the results of FEA. To achieve the defined layer thicknesses and for the integration, the performed processes can be sequenced as follows;

• Dicing

Dicing [34] is simply the process of slicing a bulk material into multiple pieces. In this study, dicing is used to obtain 10×10 pieces of silicon and ceramic materials out of 3

inch bulk materials.

• **Grinding**

Grinding [35] which is a pure mechanical process is used for thinning of diced silicon samples in our case, if needed. During this process, a rotating wheel is used for thinning the sample which is placed on a stationary chuck. During the grinding process, while the wheel rotates at a certain feedrate, the sample keeps its position and water is used as the lubricating fluid in the process.

• **Epoxy preparation**

A two component commercial epoxy has been used as the adhesive material. After mixing the two components with a defined volume or mass ratio, bubble removing is performed in a vacuum chamber (Figure 4.1).

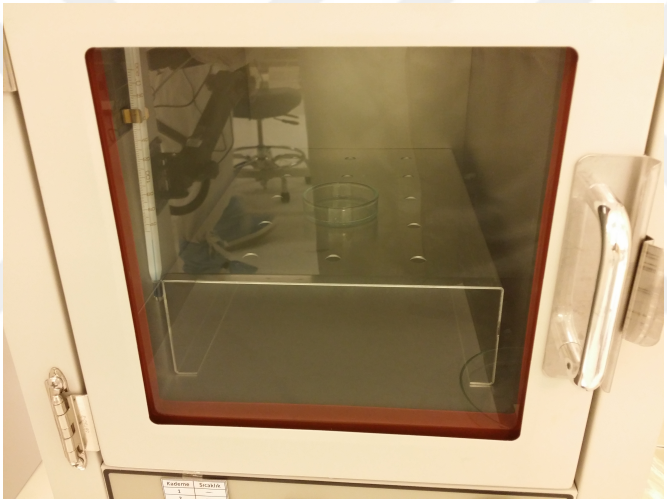

Figure 4.1: Removing of epoxy bubbles in a vacuum chamber

The bubble removal is very important to have perfect adhesion between the ceramic and silicon parts. The bubbles may be introduced during the mixing of the two epoxy components. Unless the bubbles are removed, obtaining a perfect and continuous adhesion layer will be quite impossible. Because of these random imperfections, the warpage behavior of the samples may change.

• **Cleaning of the components**

For cleaning the sample components, at first, the ceramic and silicon parts are exposed to isopropanol in a glass container. Then acetone is applied on both materials (Figure 4.2a. After these liquid cleaners, dry nitrogen is applied as shown in Figure 4.2b. This

is the last step before assemble of individual layers.



(a) Solution cleaning (b) Nitrogen cleaning

Figure 4.2: Cleaning of individual components

• **Construction of the trimaterial assembly**

After applying epoxy on ceramic layer manually, the silicon layer is integrated on ceramic using a pick and place equipment. The pick force and time and the place force and time are kept constant for all of the samples. After obtaining the trimaterial assembly, epoxy curing is performed at room temperature for 48 hours.

4.1.2 Construction of the test setup

After the trimaterial assembly is prepared, a test setup has been constructed to conduct warpage measurements. The followed steps before taking surface topology data of silicon sample are given below;

• **Integration of the sample to the test setup**

The prepared trimaterial assembly is integrated on the cold head of the test setup using a thermal joint compound which is suitable for use at cryogenic temperatures. This thermal joint compound is also used to integrate a separate ceramic material on top of which a temperature sensor is integrated to measure the time dependent temperature variation of the cold head temperature. On this ceramic part, four different locations can be used to integrate the temperature sensor. Wirebonding [36–38] is used to connect temperature sensor and gold layers which are built on ceramic by thick film coating. The other end of the gold layer is soldered and connected with flexible cables so that signals are transferred to the outer world connectors on the test setup (Figure 3.6).

• **Cleaning of BK7 glass and silicon surface**

Cleaning of BK7 optical window is performed using acetone and q-tips so that dusts or any other particles on the glass surface is cleaned. After the integration of the trimaterial assembly, a final cleaning of the silicon surface is performed by acetone and q-tip (Figure 4.3a and Figure 4.3b. Beyond this point, no other cleaning process is applied on the components.

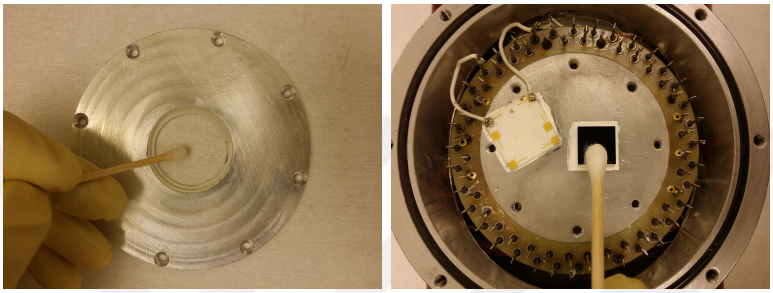

(a) BK7 glass cleaning (b) Sample cleaning

Figure 4.3: Final cleaning of silicon surface and BK7 glass

• **Obtaining vacuum environment in the test chamber**

After integrating the aluminum plate on the test chamber by using standard countersunk screws, vacuum environment should be established in the test chamber. To provide a vacuum level greater than 1 mTorr, a turbomolecular pump which has a dry pump as the backpump is utilized. At first, the dry pump is operated and after achieving vacuum level of 10^{-1} to 10^{-2} Torr, turbomolecular pump is operated. After satisfying the mentioned vacuum level, the pumping port can be dismounted without breaking vacuum in the test chamber. The test chamber and vacuum establishment are shown in Figure 4.4.

Finally, electrical connections between a source measurement control unit and the test chamber are made. After observing successive room temperatures value at the user interface of the temperature measurement software, warpage measurements on the silicon surface can be taken on an optical table bench. A flat transmission sphere which has $\frac{\lambda}{20}$ surface flatness over 4 inch surface area is used during the measurements.



(a) Test chamber (b) Vacuum port and pumping hose

Figure 4.4: Test chamber and providing vacuum environment

4.2 Measured Samples and Warpage Results

All of the samples used in measurements have the same planar dimensions of 10×10 mm. However the material thicknesses differ among these samples. In the light of FEA results, eight different integrated structures have been constructed with dimensions given in Table 4.1.

Table4.1: Sample dimensions in mm

Sample No	**1**	**2**	**3**	**4**	**5**	**6**	**7**	**8**
Ceramic	1.00	1.00	1.00	1.00	1.00	0.63	1.27	1.27
Silicon	0.1	0.2	0.3	0.4	0.5	0.5	0.3	0.5
Epoxy	AR	AR	AR	AR	AR	AR	AR	AR

In the prepared samples, the ceramic thickness is in the range of 0.63 mm to 1.27 mm. Because of the manual application of the adhesive layer, it is hard to control the epoxy thickness. For all experimentally studied cases, the same sample integration procedure has been followed. Thus, the epoxy thickness is denoted by AR (as required). However as it is experienced from earlier studies, an epoxy layer thickness in the range of 30 - 60 μm is achieved by the manual application of epoxy and pick and place integration of silicon with the same parameters. The silicon layer is thinned with 0.1 mm increments from 0.5 mm to 0.1 mm to observe the effect of silicon thickness on warpage as depicted in Figure 2.19.

Although there are initial warpages on the silicon and ceramic materials, the warpage difference on silicon between room temperature and 80 K is analyzed. The initial warpage may be caused by the dicing and grinding, epoxy curing processes and also

natural surface topology of the sample. Moreover, careless handling of the samples may change the surface topology. Considering that very small deflections should be measured precisely, handling of the samples should be done gently. For all of experimentally studied cases, the same sample integration procedure has been followed as described in Section 4.1.1

4.2.1 Measurements on Sample 1

The thinnest silicon layer among the eight integrated structures is 0.1 mm. In this study, such a thin silicon has been obtained by using only a mechanical grinding process which may have introduced extra deformations or cracks.
The first and only measurement on this sample has been taken at room temperature. The obtained fringe structure and surface topology are given in Figure 4.5 As it

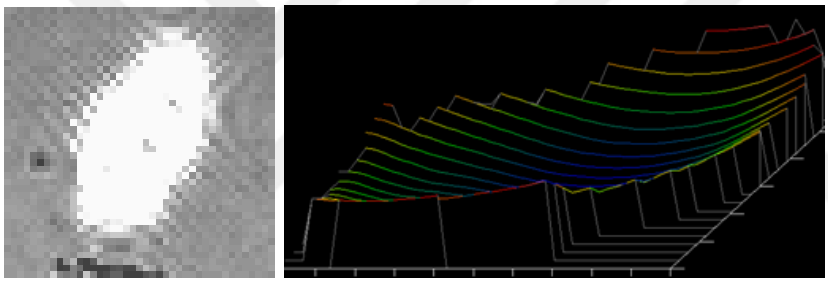

(a) Fringe structure (b) Surface topology

Figure 4.5: Warpage measurement result at room temperature for $t_{\text{silicon}} = 0.1$ mm

is observed from the fringe structure in Figure 4.5, the entire silicon surface area (10×10 mm) could not be seen hence, a proper surface topology data could not be generated either. This may be caused by excessive deformation on silicon surface. This excessive deformation may have occured during the grinding process as mentioned earlier. The silicon ceramic interface has been controlled using Scanning Electron Microscopy (SEM) to observe thickness and uniformity of the epoxy layer.

From the SEM measurements, initially the trimaterial assembly (Sample 1), which has 10×10 mm planar dimensions has been diced along two diagonal axes as seen in Figure 4.6a. A triangular slice out of this assembly has been taken and the epoxy interface has been examined along the two edges using SEM. During the SEM analyses, it has been observed that the uniform epoxy layer thickness assumption in the FEA is

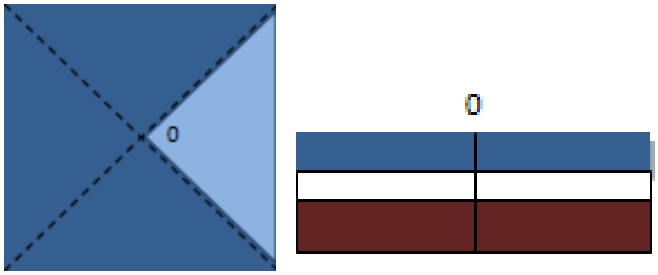

(a) Dicing path (b) Cross section view

Figure 4.6: Diagonal dicing of the sample and cross sectional view

totally violated for this sample. The epoxy layer thickness varied between 7.5 μm to 90.5 μm. Moreover, there did not exist any epoxy material in one end as observed in Figure 4.7c. This may also cause excessive and non uniform warpage of silicon sample regardless of the epoxy curing effect or material handling issues.

After having the SEM pictures in Figure 4.7, there was no need to cool the sample 1



(a) $t_{epoxy} = 7.59$ μm (b) $t_{epoxy} = 90.52$ μm (c) Unfilled epoxy area

Figure 4.7: SEM images of Sample 1

and analyse its warpage behavior. Due to the effects of non uniform epoxy layer, voids between the ceramic and silicon parts, Sample 1 was deformed excessively. Moreover grinding and epoxy curing processes of such a thin sample may have affected the initial warpage value. Besides, due to the process difficulties in obtaining a very thin silicon sample, Sample 1 will have very low flexural rigidity even when it is successively thinned. The low flexural rigidity may be a reason of failure when thermal stresses increase during cooling.

4.2.2 Measurements on Sample 2

For sample 2, 1.00 mm thick ceramic and 0.2 mm thick silicon layers have been integrated using epoxy material. Similar to the first sample, the second sample has high initial surface deformation with 1.816 μm PV at 295 K as seen in Figure 4.8

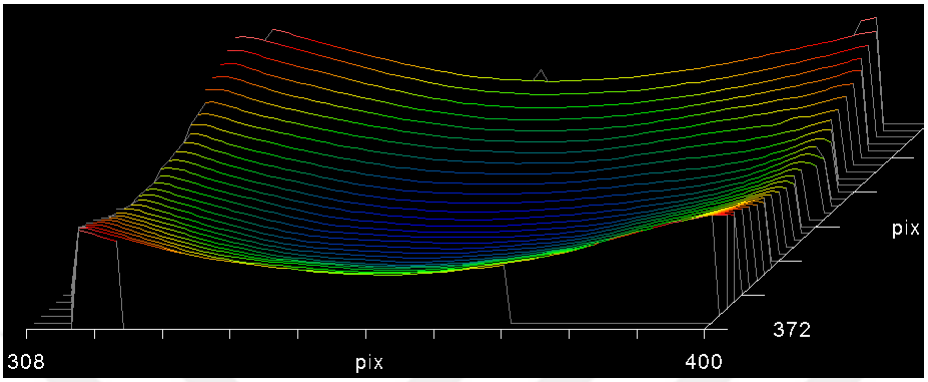

Figure 4.8: Warpage of silicon at room temperature for Sample 2

When the temperature starts to decrease, PV measurements were recorded at 260 K, 91 K and 80 K. The PV values at these temperatures are provided in Figure 4.9. The PV difference between 295 K and 80 K has been found as 2.646 μm.

To determine the epoxy thickness precisely, dicing and SEM analysis have also been applied to Sample 2. According to the results of 13 SEM images, an average thickness of the epoxy has been found as 58 μm. Some of the SEM images are represented in Figure 4.10.

The effect of bubble removal process from the epoxy layer is also observed from the SEM images. A perfect adhesion between the three layers has been obtained successfully according these images (Figure 4.10).

4.2.3 Measurements on Sample 3

For the third sample, the silicon layer had 0.3 mm thickness. The first measurement of this sample is taken at 295.7 K as 0.260 μm PV.
Although having similar material thicknesses, there exists 1.556 μm difference in the

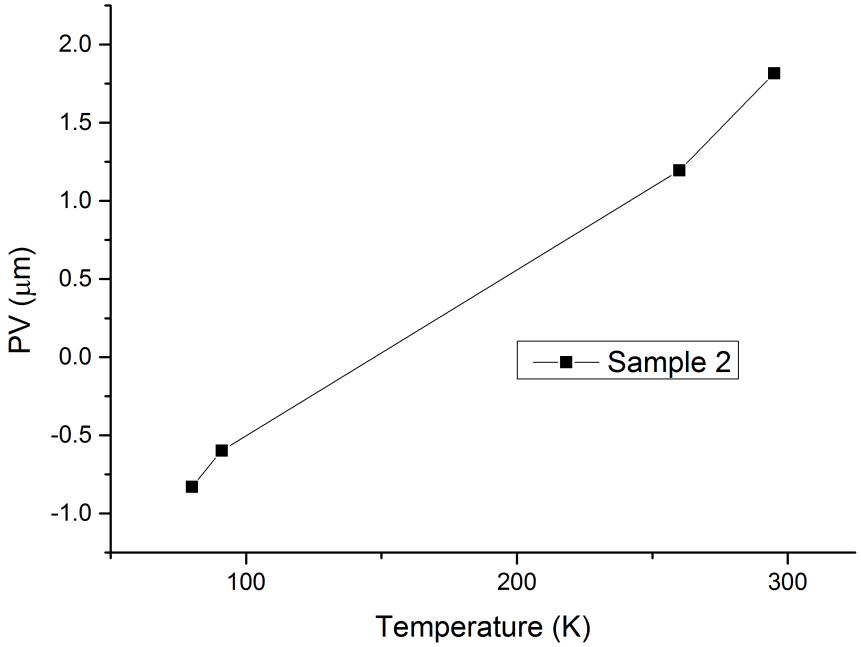

Figure 4.9: Temperature dependent PV values for Sample 2

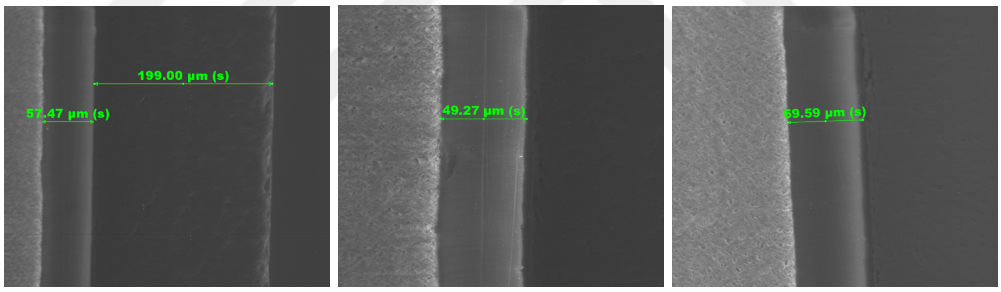

(a) Image 1 (b) Image 2 (c) Image 3

Figure 4.10: SEM images of Sample 2

initial PV values between Sample 2 and Sample 3. This may be caused by duration of grinding process on these two samples. Moreover, the epoxy curing process is more critical for thinner silicon in terms of warpage because of higher rigidity of thick silicon sample. The surface profile for Sample 3 at room temperature is given in Figure 4.11

Temperature dependent PV measurements have also been performed with Sample 3. Measurement results are provided in Figure 4.12. In this figure, a linear behavior of PV change with changing temperature is clearly observed. At 80 K, warpage is measured as -4.251 μm so that the warpage difference between room temperature

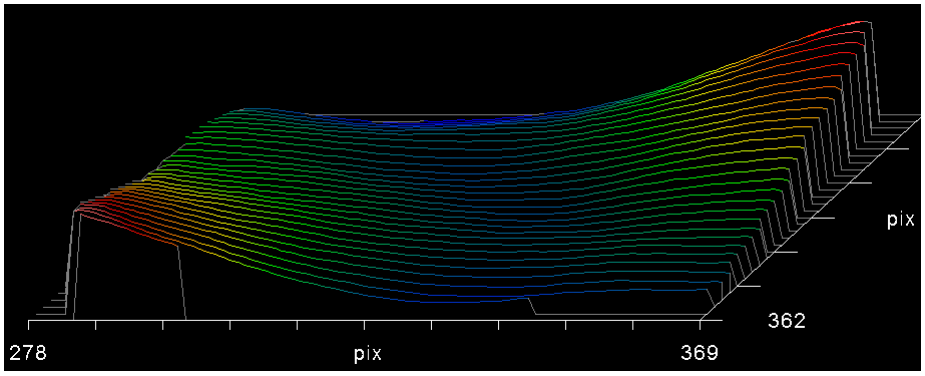

Figure 4.11: Warpage of silicon at room temperature for Sample 3

and 80 K has been found as 4.511 μm.

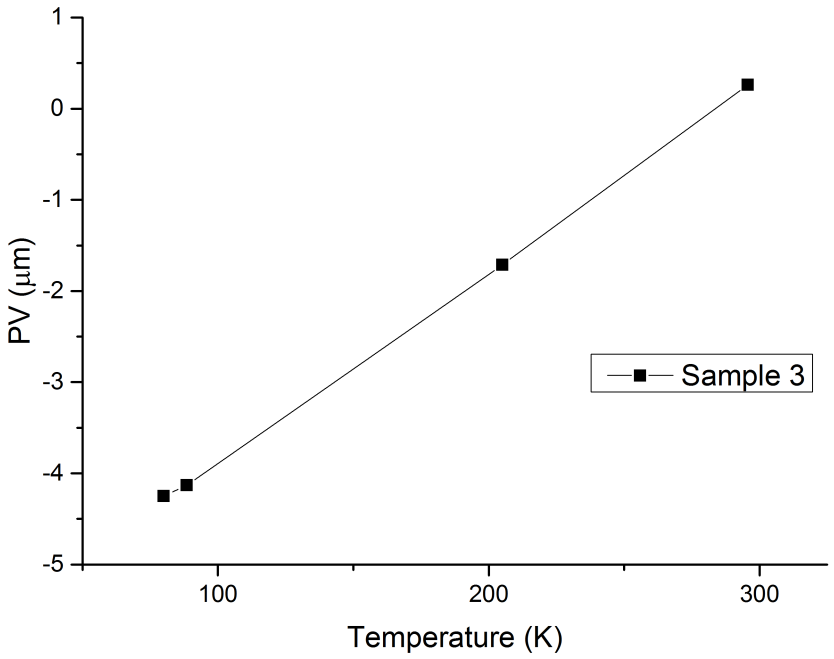

Figure 4.12: Temperature dependent PV values for Sample 3

To determine the realized epoxy material thickness, the same procedure has been followed as is done for the previous samples. After dicing and SEM measurement, the average thickness of epoxy has been determined as 32 μm for Sample 3. Some of the SEM images are given in Figure 4.13. In all of the SEM images, the epoxy thickness changed in the range from 27 μm to 37 μm which implies a uniform epoxy distribution.

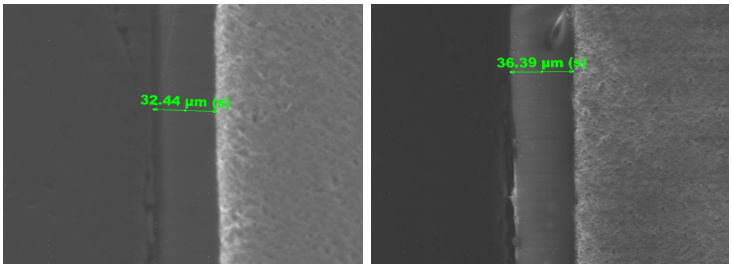

(a) Image 1 (b) Image 2

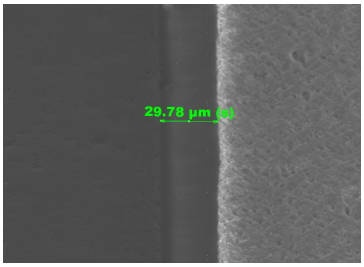

(c) Image 3

Figure 4.13: SEM images of Sample 3

4.2.4 Measurements on Sample 4

Sample 4 consisted of 1.00 mm thick ceramic, 0.4 mm thick silicon and epoxy material. Similar to previously performed tasks, the first measurement was taken at 295.5 K with a PV value of -0.241 μm.

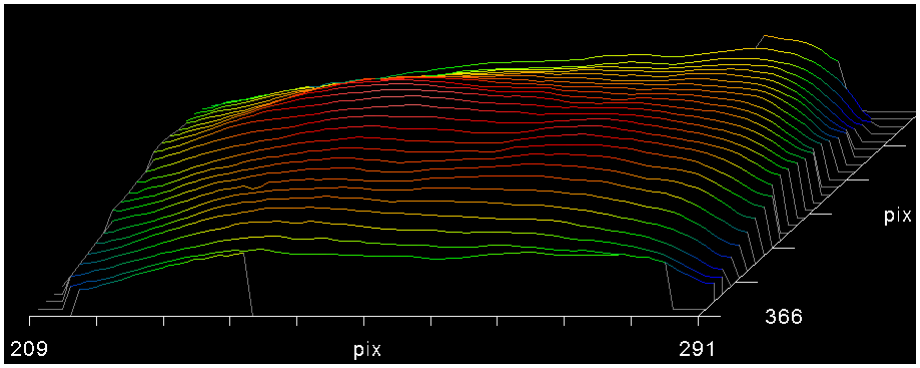

Figure 4.14: Warpage of silicon at room temperature for Sample 4

The warpage distribution for Sample 4 is presented in Figure 4.14. Unfortunately, temperature dependent PV values couldn't be obtained for this sample because having lower temperatures on this trimaterial assembly resulted in excessive deformation of the sample. Due to excessive deformation, the fringe formation could not observed on the entire surface area of silicon, especially for temperatures lower than 160 K.

Although micrometer level surface deflections have been dealt with in the present study, an interferometer with flat transmission sphere has been used to determine these deflections. Generally, spherical transmission spheres are preferably used to obtain surface topology data of curved surfaces. In our cases, the most of the samples had nearly flat surfaces at room temperature whereas they bend at cryogenic temperatures because of the coefficient of thermal expansion mismatch of their constituents. For some samples, the radius of curvature of the surface at cryogenic temperature was so small that the surface topology could not be characterized with a flat transmission sphere. Some of the reflected laser beams from the sample surface, especially from highly curved regions of the surface i.e. corners, did not come back to the CCD camera. Hence, dark regions have been observed on the silicon surface as shown in Figure 4.15d and 4.15e. However, fringe formation over all the surface area has been observed at higher temperatures.

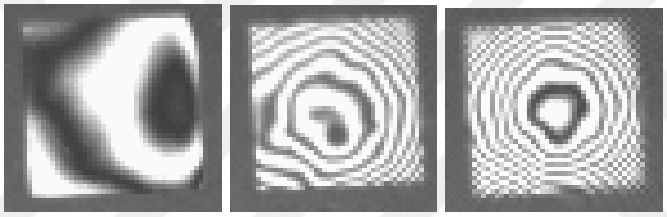

(a) $T = 295.5$ K (b) $T = 209.5$ K (c) $T = 170$ K

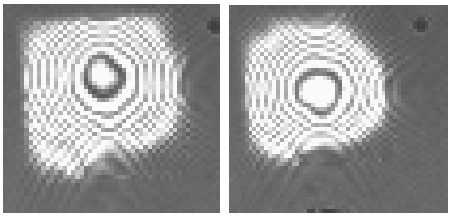

(d) $T = 145$ K (e) $T = 80$ K

Figure 4.15: Temperature dependent fringe structures on Sample 4

The non formation of a complete fringe pattern has also been analysed using a curved sample with a known radius of curvature. Sample 4 had approximately 4600 mm radius of curvature at 145 K and the observed fringe pattern is given in Figure 4.15d. The curved sample, which is actually an objective lens, has 2350 mm radius of curvature. Its surface topology has been measured at room temperature and under atmospheric pressure. The obtained fringe structure is given in Figure 4.16.

From Figure 4.16, the effect of radius of curvature on the fringe pattern is clearly ob-

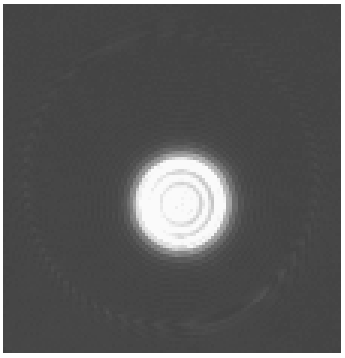

Figure 4.16: Fringe pattern of the objective lens that has 2350 mm radius of curvature

served. After a careful look at the fringe pattern, it is observed that there exists one bright circle which contains circular fringes and another dark circle with a larger diameter. Although the sample had larger diameter of bright fringe circle in the middle, the fringe pattern was not observed on the entire surface area as some of the reflected laser beams from the sample surface could not reach the CCD camera of the interferometer. This is actually the proof of excessive bending on sample 4 and also on some other experimentally studied samples.

To predict the warpage on highly deformed surfaces, spherical bending assumption has been used with a known value of radius of curvature at measurement temperatures. For example, Sample 4 had 4470 mm radius of curvature at 80 K. This measurement has been taken from part of the observed fringe pattern on Sample 4 (Figure 4.17). When the radius of curvature of 4470 mm has been extrapolated on 10×10 mm silicon surface, the PV value for the entire field has been found as -5.56 μm. DIFFSYS Version 3.92 AZ software has been used for warpage extrapolation calculations. The same procedure has also been followed with other excessively deformed silicon surfaces for which a full fringe formation could not be observed.

The temperature dependent PV graph has also been provided for Sample 4. However, the last point has been extrapolated at 80 K and labelled with a red circular dot in Figure 4.18. The interferometric measurement has been combined with spherical bending assumption and calculations for 80 K data point.

When warpage measurements are completed, this sample is also diced to determine the epoxy layer thickness using the SEM. As a result of thickness measurements of

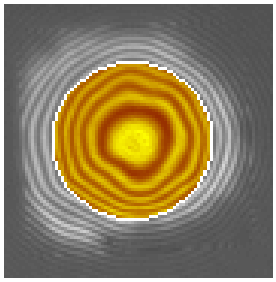

Figure 4.17: Surface topology and radius of curvature data taken from a limited portion of Sample 4 at 80 K

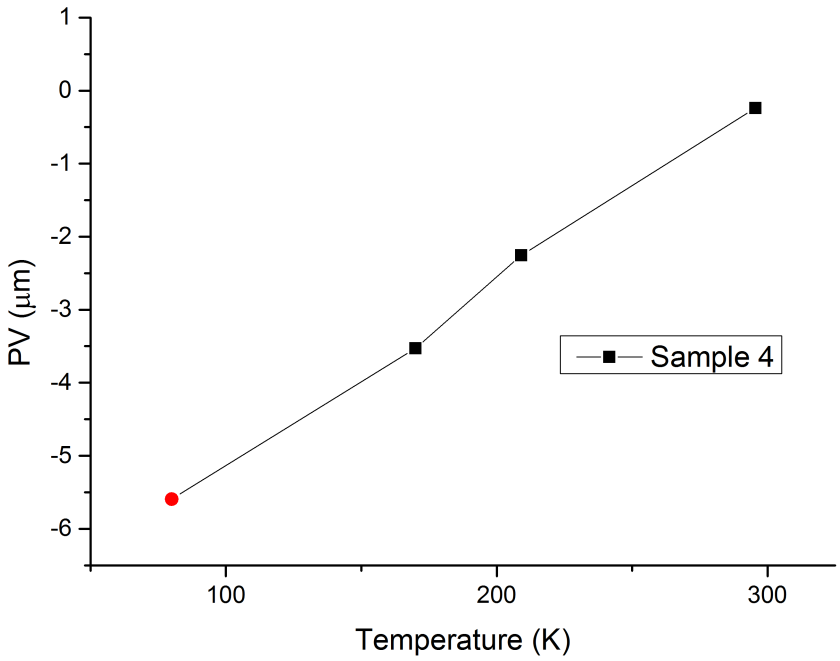

Figure 4.18: Temperature dependent PV values for Sample 4

epoxy from 13 datapoints, the average thickness has been found as 34 μm. Some SEM images are given in Figure 4.19. As it is seen from the figure, any void or discontinuity has not been observed throughout the epoxy layer.

4.2.5 Measurements on Sample 5

Sample 5 is the last sample with 1.00 mm thick ceramic layer. The initial deformations for Sample 3 and Sample 4 have been measured as 0.260 and -0.241 μm, respec-

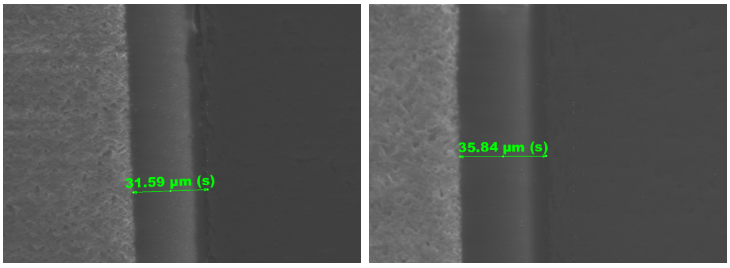

(a) Image 1 (b) Image 2

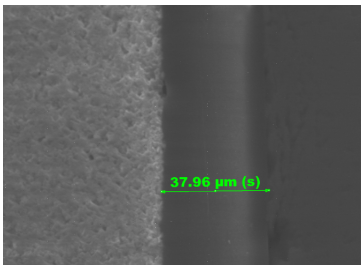

(c) Image 3

Figure 4.19: SEM images of Sample 4

tively. Although slightly lower initial deformation was expected for Sample 5 because of thicker silicon layer, the initial warpage for Sample 5 was measured as -1.251 μm at 295.7 K, (a lot higher compared to Sample 3 and 4). The warpage distribution for Sample 5 at room temperature is given in Figure 4.20.

In this case, full formation of the fringe pattern could not be initially observed around 187 K. When the temperature of the sample was lower, the fringe structure has been observed over a smaller portion of the silicon surface. Figure 4.21 represents temperature dependent fringe formation on the silicon surface of Sample 5.

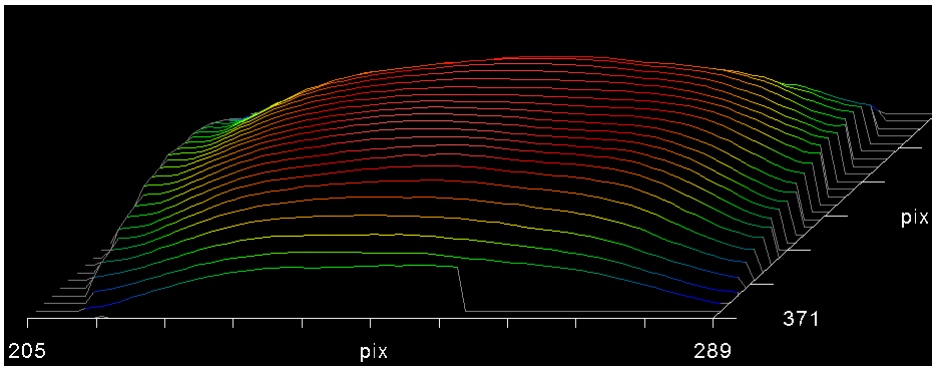

Figure 4.20: Warpage of silicon at room temperature for Sample 5

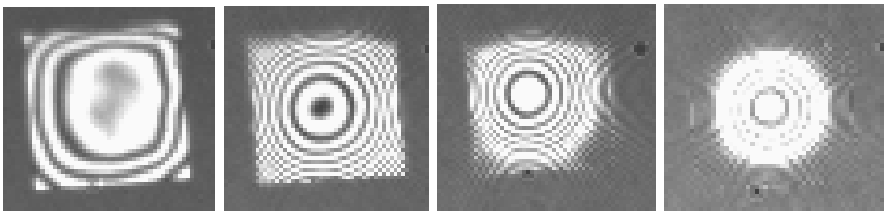

(a) $T = 295.7$ K (b) $T = 224$ K (c) $T = 187$ K (d) $T = 80$ K

Figure 4.21: Temperature dependent fringe structures on Sample 5

Similar to the previous case, the fringe data at 80 K has been masked using the sofware and the radius of curvature value of the defined area has been found as 3400 mm. The circular behavior of interfering fringes in Figure 4.22 also show that the sample has been exposed to spherical bending so the application of the same radius of curvature for the entire silicon surface was a reasonable assumption.

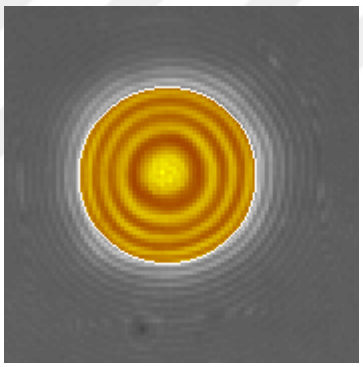

Figure 4.22: Surface topology and radius of curvature data taken from a limited portion of Sample 5 at 80 K

When the found radius of curvature is extended along the 10×10 mm silicon surface, the PV value has been found as -7.35 μm.

With the estimated PV value from the measurements at 80 K, a temperature dependent PV graph is given in Figure 4.23. Similar to the previous case, 80 K data point has been labeled with a circular red marker because this data point is not directly measured but it is an estimation from the measurement results. Warpage of this sample between room temperature and 80 K is found as 6.10 μm.

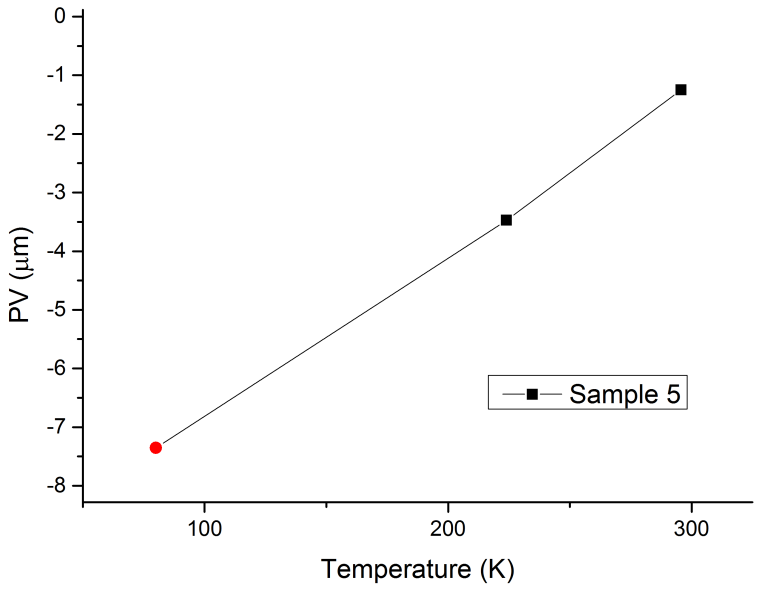

Figure 4.23: Temperature dependent PV values for Sample 5

4.2.6 Measurements on Sample 6

Sample 6 consisted of 0.63 mm thick ceramic and 0.5 mm thick silicon. Contrary to the previous cases, the silicon and ceramic layers had closer thicknesses. The expectation based on the FEM results was that bending of this sample would be excessively high at cryogenic temperatures. This expected result is also observed from the temperature dependent fringe formation given in Figure 4.24. A full field fringe formation could not be observed approximately below 240 K whereas the temperature limit was 185 K and 145 K for Sample 5 and Sample 4, respectively. This result alone also implied that deformation at 80 K of Sample 6 will be higher than those for Sample 5 and Sample 4.

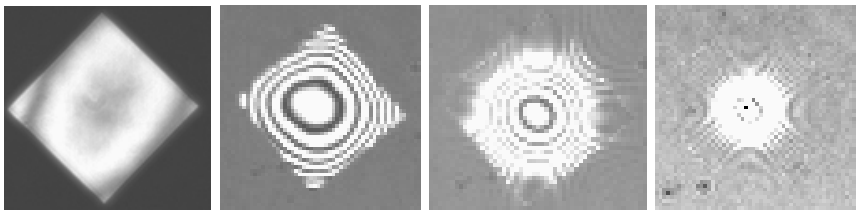

(a) $T = 295$ K (b) $T = 277$ K (c) $T = 225$ K (d) $T = 80$ K

Figure 4.24: Temperature dependent fringe structures on Sample 6

As it is observed in Figure 4.24, when the temperature of the trimaterial assembly goes down, the fringe structure is defocused and they are not observed on some portion of the silicon surface. This especially happens at the corners. The initial deflection of this sample has been measured as 0.31 μm with the given surface topology in Figure 4.25.

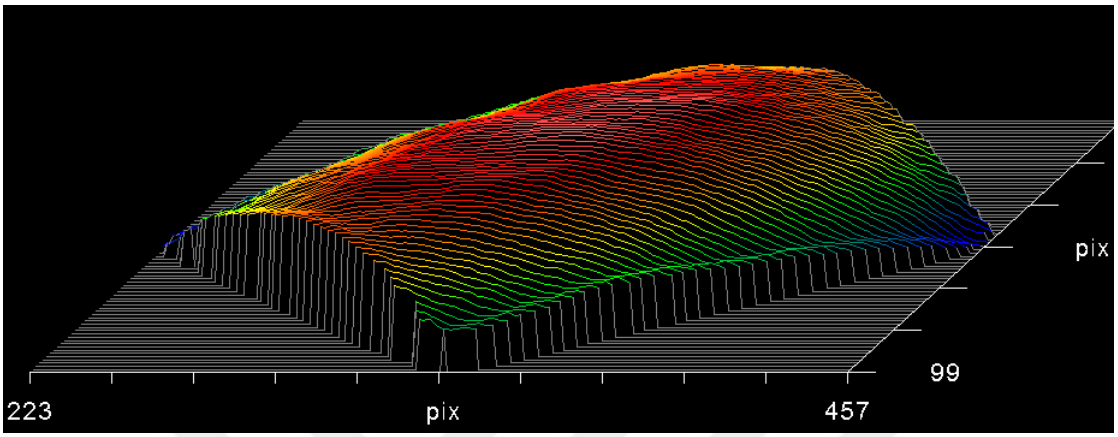

Figure 4.25: Warpage of silicon at room temperature for Sample 6

The radius of curvature for Sample 6 at 80 K has been found as 2400 mm. As it is expected, the radius of curvature of Sample 6 is much smaller than any other cases. The found radius of curvature results in 10.42 μm PV for 10×10 mm or $\varnothing$14.142 mm surface area. A warpage difference of 10.11 μm has been achieved between 295 K and 80 K.

4.2.7 Measurements on Sample 7

Sample 7 had 0.3 mm thick silicon and 1.27 mm thick ceramic parts. An initial warpage value of 1.18 μm has been measured at 295 K. The warpage has been found as -1.62 μm at 80 K. Surface topologies at mentioned temperatures are given in Figure 4.26 and 4.27. The concave surface topology at 295 K is turned to convex form at 80 K. All of the experimentally studied samples have convex shape when they were cooled down. This behavior is caused by the greater coefficient of thermal expansion of ceramic with respect to silicon material as given in Table 2.1. So with decreasing temperature, the ceramic part tends to contract more than silicon resulting in a convex shape. The warpage difference between room temperature and 80 K has been found as 2.80 μm. For Sample 7, having low warpage values at room temperature and 80 K enabled fringe

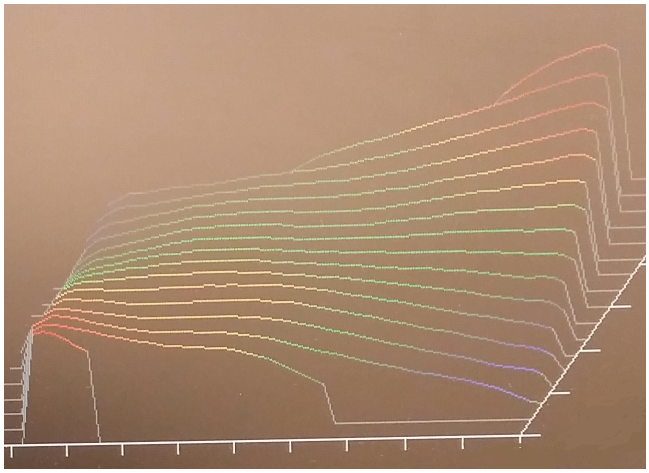

Figure 4.26: Warpage of silicon at room temperature for Sample 7

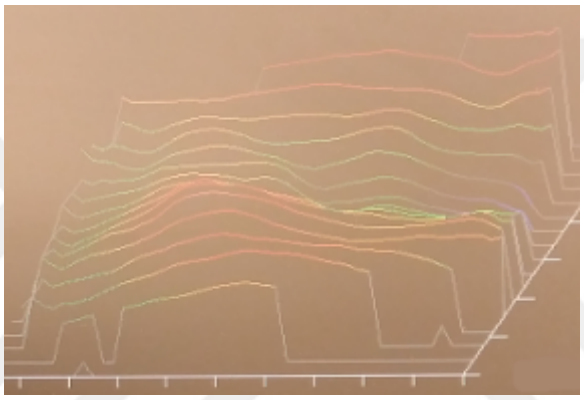

Figure 4.27: Warpage of silicon at 80 K for Sample 7

formation over the entire silicon surface. Hence, there was no need to calculate the radius of curvature value at 80 K and extrapolate it. The provided warpage values for Sample 7 have directly been measured at the mentioned temperatures.

4.2.8 Measurements on Sample 8

Sample 8 had 1.27 mm thick ceramic with 0.5 mm thick silicon. Room temperature surface topology is given in Figure 4.28. The PV value at the initial state, 294 K was -0.12 μm. The minus sign indicated that this sample had already a convex profile at room temperature.

At 80 K, small regions around the corners of the sample are shaded because of previously mentioned excessive bending problem. However, the radius of curvature of

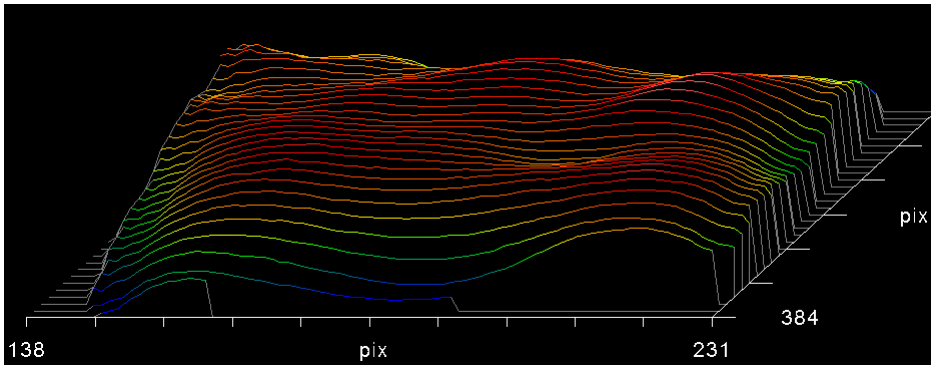

Figure 4.28: Warpage of silicon at room temperature for Sample 8

Sample 8 at 80 K could be determined from experimental measurements and has been found as 4900 mm. Hence, the whole field PV value has been determined as 5.10 μm on 10×10 mm sample. As a result, the difference between 294 K and 80 K measurements has been 4.98 μm.

The fringe structures for Sample 8 for three different temperatures are given in Figure 4.29

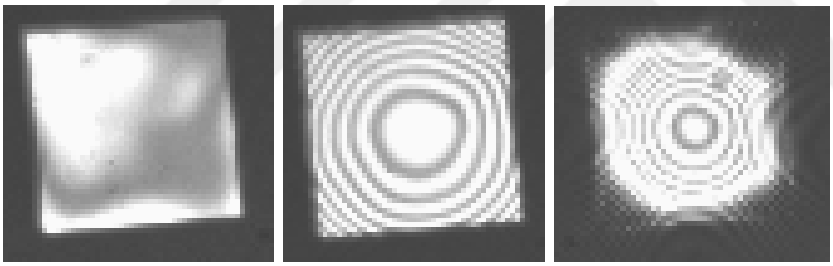

(a) $T = 294$ K (b) $T = 206$ K (c) $T = 80$ K

Figure 4.29: Temperature dependent fringe structures on Sample 8

As observed from the fringe structures, the deflection at 80 K for Sample 8 was not as large as the deflection of Sample 6 at the same condition. This was just because of the increased ceramic thickness effect as indicated in Chapter 2.

The temperature dependent PV value is given in Figure 4.30. This graph together with the previous temperature dependent PV graphs show very similar behavior. The PV values of Sample 8 have been -0.12, -2.48 and -5.10 μm at temperatures of 294 K, 206 K and 80 K, respectively.

The first data point of Figure 4.30 is again labelled with red circular marker which is different than two other data points because of extrapolation. On the other hand, the remaining data points are obtained by only direct measurements.

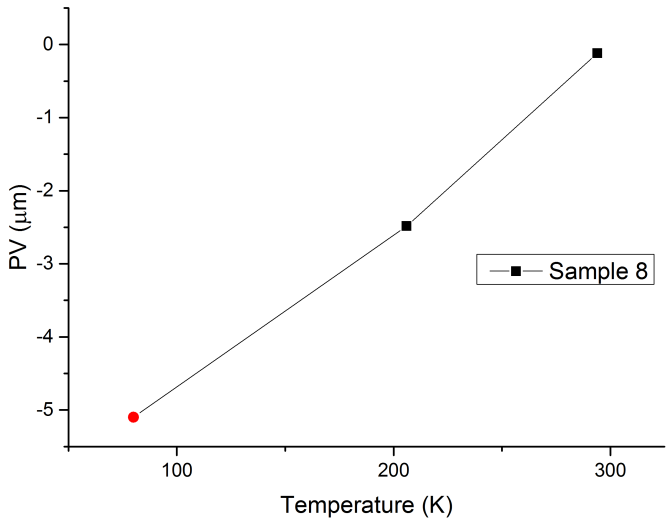

Figure 4.30: Temperature dependent PV values of Sample 8

4.2.9 Comparison of warpage measurements

To sum up the experimental results, the difference between room temperature and 80 K warpage values of the eight samples are given along with material thicknesses in Table 4.2. For Sample 1, expressing an average epoxy thickness and warpage difference are not necessary because a uniform epoxy layer without voids could not be achieved.

Table4.2: Experimental warpage results

No	$t_{\textbf{ceramic}}$	$t_{\textbf{silicon}}$	$t_{\textbf{epoxy}}$	W
1	1.00	0.1	*	*
2	1.00	0.2	0.058	2.67
3	1.00	0.3	0.032	4.51
4	1.00	0.4	0.034	5.32
5	1.00	0.5	0.061	6.10
6	0.63	0.5	0.029	10.11
7	1.27	0.3	0.027	2.80
8	1.27	0.5	0.032	4.98

According to Table 4.2, increasing silicon thickness, while keeping the ceramic thickness constant increases warpage. This is the observed case among Sample 2, 3, 4, 5. When Samples 5, 6 and 8 are analyzed it was concluded that increasing ceramic thickness for constant silicon thickness decreases warpage.

4.3 Grinding Effect on Warpage

For Sample 1, it is thought that the grinding process may be primarily responsible for the excessive deformation of this sample. To prove this effect, three different silicon materials are prepared without grinding ($t_{\text{silicon}} = 0.5$), and with grinding process ($t_{\text{silicon}} = 0.4, 0.3$ mm). Among these three samples, the grinding effect is obviously seen from Figures 4.31 and 4.32 indicating that the grinding indeed increases warpage of the silicon.

In the preparation of the samples, firstly, all three samples have been diced from the same silicon wafer and the ungrinded sample was characterized at room temperature

and under atmospheric pressure conditions. The PV value has been measured as 0.07 μm for the ungrinded silicon sample.

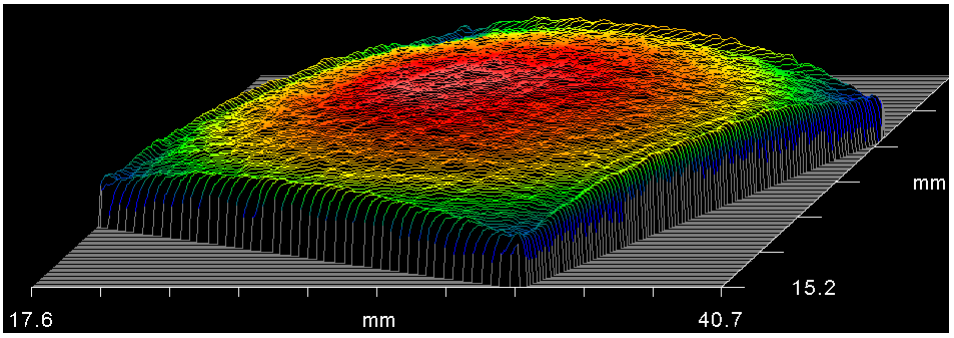

Figure 4.31: Ungrinded silicon surface topology at room temperature

Secondly, the other samples have been grinded to 400 μm and 300 μm thicknesses and the surface topology measurements are given in Figure 4.32. For these two grinded

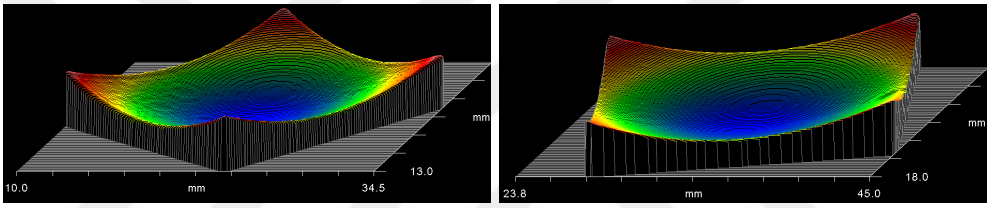

(a) Grinded to 400 μm, $PV = 0.68$ μm (b) Grinded to 300 μm, $PV = 1.35$ μm

Figure 4.32: Grinded samples with measured warpage values at room temperature

samples, a concave surface topology has been obtained with 0.68 μm and 1.35 μm PV values for the silicon thicknesses of 0.4 mm and 0.3 mm, respectively. These results clearly represent the grinding effect on silicon warpage. If the thickness is further reduced, a dramatic increase in warpage values can be expected which was an issue for Sample 1.

4.4 Comparison of Numerical and Experimental Results

After obtaining experimental results, a comparison of the FEA results with experimental ones has been performed to validate the numerical model. FEA is repeated with more precisely known values of the epoxy thickness. It is better to compare experimental results with the updated finite element results listed in Table 4.3. In this table, results for Samples 2-8 are provided in pairs, the only difference being the

estimated (0.05 mm) and realized epoxy thicknesses.

Table4.3: Updated FEA results

No	$t_{\textbf{ceramic}}$ **(mm)**	$t_{\textbf{silicon}}$ **(mm)**	$t_{\textbf{epoxy}}$ **(mm)**	**W** (μ**m**)
1	1.00	0.2	0.050	2.78
2	1.00	0.2	0.058	2.60
3	1.00	0.3	0.050	4.30
4	1.00	0.3	0.032	4.65
5	1.00	0.4	0.050	5.38
6	1.00	0.4	0.034	5.67
7	1.00	0.5	0.050	6.12
8	1.00	0.5	0.061	5.93
9	0.63	0.5	0.050	10.92
10	0.63	0.5	0.029	11.48
11	1.27	0.3	0.050	2.86
12	1.27	0.3	0.027	3.17
13	1.27	0.5	0.050	4.31
14	1.27	0.5	0.032	4.55

In Table 4.3, FEA results are provided for all of the experimentally studied samples except Sample 1 because, at cryogenic temperature, the warpage could not be examined with this sample. As observed from this table, epoxy thickness parameter is one of the critical factors which can affect warpage results dramatically. For a fair comparison with results, FEA had to be revised by using a better approximation for the epoxy material thickness. Without exception, indicated results which increased epoxy thickness reduces warpage.

The revised FEA results and experimental ones for all eight samples are given in Table 4.4.

Table4.4: Revised FEM results versus experimental results

Sample	$t_{\mathbf{ceramic}}$	$t_{\mathbf{silicon}}$	$t_{\mathbf{epoxy}}$	**FEM, W (μm)**	**Exp, W(μm)**	**Diff (%)**
1	1.00	0.1	*	*	*	*
2	1.00	0.2	0.058	2.60	2.67	2.5
3	1.00	0.3	0.032	4.65	4.51	-2.9
4	1.00	0.4	0.034	5.67	5.32	-6.2
5	1.00	0.5	0.061	5.93	6.10	2.9
6	0.63	0.5	0.029	11.48	10.11	-12.0
7	1.27	0.3	0.027	3.17	2.80	-11.7
8	1.27	0.5	0.032	4.55	4.98	9.5

Numerical and experimental results for integrated samples with 1.00 mm thick ceramic layer are plotted in Figure 4.33. The percentage differences between the FEA results and experimental ones for Samples 2-8 are presented in Table 4.4.

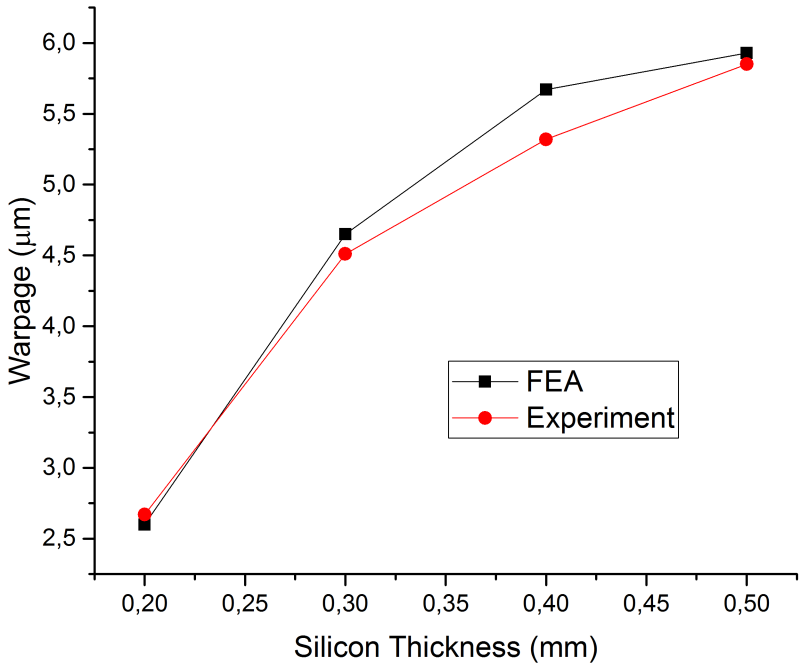

Figure 4.33: Warpage results of Samples 2, 3, 4, 5

Among the tested samples with 1.00 mm thick ceramic layer, the maximum difference between numerical and experimental results has been obtained as 6.2% for Sample 4 which has a 0.4 mm thick silicon layer. The remaining three data points show good coherence according to numerical estimations and experimental verification. The best coherence has been achieved for Sample 2 with a 2.5% difference whereas the difference has been 2.9% for Sample 3 and Sample 5. For samples 4, 5, 6 and 8, the warpage at cryogenic temperature had been estimated by extrapolation. Because of the highly bended silicon layer, fringe formation could not be observed near the four edges of the assembly. In these cases, a spherical bending of the trimaterial assembly is assumed as done in reported analytical [11], [3] and FEM [22] studies. Radius of curvature values at 80 K have been estimated by using the measurements at this temperature. However the surface topology data has been taken from a limited portion of the silicon surface. With known value of radius of curvature, warpage for the entire field has been calculated based on spherical bending assumption. Hence, in addition to the error margins for these samples, given in earlier in Table 3.3, there also exists error caused by spherical bending assumption and radius of curvature calculations.

Three out of eight samples had 0.5 mm thick silicon with different ceramic thicknesses. Both experimental and numerical results for these samples are plotted in Figure 4.34. According to provided results the best coherence has been observed for Sample 5 with 2.9% error.

Moreover, it has been shown that some fabrication and assembly processes may introduce additional deformations on the samples. During the experimental studies, it has been observed that obtaining a thin silicon layer results in high initial deformations on the sample caused by the grinding process. In addition to grinding, epoxy curing process may also be affecting because of the very low flexural rigidity of such a thin silicon sample. Although epoxy curing effect has not been validated by experiments, the effect of the grinding process has clearly been expressed in Section 4.3. Non fringe formation for some of the samples is associated with excessive bending. As a result of the excessive bending of the sample, some of reflected laser beams from the sample surface could not reach the CCD camera in the phase shifting Fizeau laser interferometer system where the fringe pattern originates. To prove this claim, the

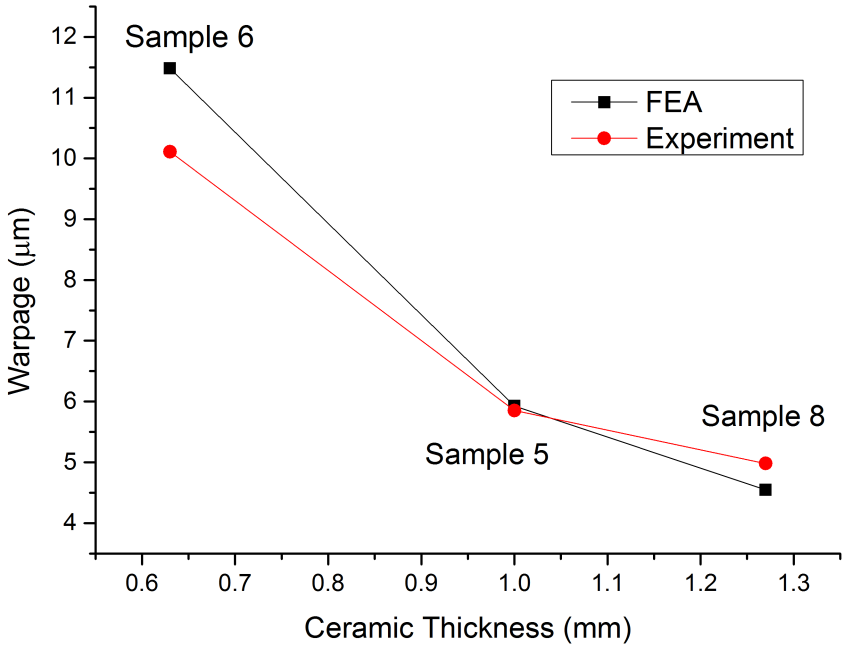

Figure 4.34: Warpage results for $t_{\text{silicon}} = 0.5$ mm, Samples 5, 6 and 8

surface topology of an objective lens which had a radius of curvature of 2350 mm has been measured without using the optical window at room temperature and under atmospheric pressure so that possible experimental setup effects could be eliminated. The fringe pattern has been observed only on a portion of the lens surface as given in Figure 4.16. According to this observation, one can conclude that when excessive bending and small radius of curvature exist on a sample, fringe pattern could not be observed for the entire surface area of the sample.

In addition to warpage measurements and predictions on the mentioned trimaterial assemblies, equivalent maximum stress predictions on silicon material are provided in Table 4.5 by post processing of FEA.

Table4.5: Equivalent maximum stress on the silicon

Sample No	**2**	**3**	**4**	**5**	**6**	**7**	**8**
Equivalent max stress (MPa)	79.4	58.1	68.4	88.4	65.5	58.1	69.6

The maximum equivalent thermal stress is observed on Sample 5 with a value of 88.4 MPa, whereas the minimum has occured for Sample 3. According to thermal stress

outputs, equivalent maximum thermal stress on the silicon sample can be decreased approximately 34.3% by changing only silicon thickness. Thermal stresses caused by coefficient of thermal expansion mismatch should be studied in detail. In this study, equivalent maximum stress values on silicon material are shared to express the approximate thermal stress level on the silicon material.

To sum up the comparison between the FEA and experimental results, it should be noted that linear homogeneous isotropic material behavior represents the warpage of experimentally studied trimaterial assembly in the defined temperature range. During the experiments, elastic deformation on the silicon material is observed when the sample is heated to the room temperature from cryogenic temperatures. Hence, a simple FEM can represent the behavior of trimaterial assembly which is vital for the good coherence of numerical and experimental results. Another important factor of this good coherence was the controlling of the samples which are produced with a series of processes like epoxy injection, curing, grinding etc. For example, controlling the continuity and thickness of epoxy layers or grinding process effects prevented to make serious mistakes. Hence, the success of the good match between the FEA and experiments is obtained by many parameters.

CHAPTER 5

CONCLUSIONS AND FUTURE WORK

5.1 Summary and Conclusions

The main aim of this study was to utilize a test setup to measure out of plane deformations of trimaterial assemblies at room temperature as well as at cryogenic temperatures. Two test setups with different coolant techniques and different features have been designed. The first design has not been employed because of the usage of cryocooler and active pumping during the measurements. The operation frequency of cryocooler and vibrations on pumping port caused by active pumping may lead to disturbances on the fringe pattern. To eliminate such risks, the second design has been made in which liquid nitrogen is used as a coolant instead of a cryocooler. In this configuration, vibrations caused by the operating frequency of the cryocooler has been eliminated. It has been observed that even the boil off of liquid nitrogen affects the fringe pattern. Hence, it is very important to take measurements when the temperature is stabilized i.e. boil off rate of liquid nitrogen is decreased. Moreover, the pumping port in the second design can be separated from the vacuum envelope after obtaining vacuum inside this chamber so that vibrational effects caused by active pumping is fully eliminated. Four different parameters which affect warpage measurements have been defined and the effect of each on the warpage measurements has been examined.

At the beginning of this study, a literature search has been performed to obtain correct material properties of the constituents, which is one of the vital parts to complete

this thesis. The material properties which are used in FEA must cover temperature dependent changes in the range from room temperature to cryogenic temperatures, in our case it is 77 K. Although a few cryogenic material properties such as Poisson's ratio of epoxy material could not be obtained precisely, experimental results show good coherence with those of FEA. Please remember that temperature dependent material properties are not used in this study.

Analytical solutions as well as finite element analyses are widely used to predict warpage of an electronic package or stress level on a sensor caused by thermal mismatch. In this study, FEA is preferred but analytical solutions could also be used to obtain the predictions. However, when the warpage result of a trimaterial assembly with a thin adherent layer is desired, very thin adhesive layer with respect to adherent thicknesses assumption of analytical solution may be violated. This situation is depicted in Figure 1.26 and 1.27. In FEA predictions, homogeneous isotropic and linear elastic behaviour has been assumed. Moreover, the elastic deformation on trimaterial assembly due to changing temperature was observed via many experiments. Parametric analyses have been performed on ceramic, epoxy, silicon integrated structure. According to the defined thermal load and boundary conditions, the warpage of the silicon has been determined for numerous combinations of constituting material thicknesses of the trimaterial assembly. After determining the effect of each layer thickness, samples have been prepared for the experiments. Some of the important preparation steps can be stated as cleaning of the samples and the setup features, the integration of the trimaterial assembly to the test setup and removing the bubbles from the epoxy.

Experimental results for Samples 2-5 indicated that increasing silicon thickness by using the same ceramic thickness clearly increases warpage. On the other hand, if the silicon thickness is kept constant and the thickness of the ceramic is increased, the warpage dramatically decreases according to the results for Samples 5, 6 and 8. The experimental results for all of the samples except Sample 1 showed good coherence with FEA results. The worst match exists for Sample 6 with 12.0% difference. With the experimental studies, it has been observed that the grinding process had a significant effect on the warpage of silicon. If an extremely thin silicon layer is obtained by only using grinding process, the component will most probably be extremely deformed. This is one of the probable reasons of highly deformed silicon surface of Sample 1. Moreover, handling problems or a large amount of deformation due to

epoxy curing for such a thin silicon may exist for Sample 1. As a result of excessive surface deformation of this sample, cryogenic temperature measurements could not be obtained. In addition to grinding process, it is observed that a non uniform epoxy distribution affects natural deformation behaviour of the sample. It happens not only for Sample 1 but also for some other samples which are not presented in this study. A minimum difference of 2.5% has been obtained between the experimental and FEA results for Sample 2 with 2.60 μm numerical prediction and 2.67 μm measurement result for warpage. The effect of mechanical vibrations has been clearly observed during the measurements. Fortunately, the test setup design eliminated mechanical vibrations as much as possible. Moreover, temperature stabilization was waited before taking the measurements so that drifts in fringe patterns could disappear.

5.2 Recommendations for Future Work

For future work, warpage analysis may be performed on the entire assembly given in Figure 1.23 for which surface deformations and thermal stresses play a critical role. This is crucial for ending up with reliable products. In this study, warpage on a generic trimaterial assembly which was composed of commonly used materials in electronic packaging such as ceramic, silicon and epoxy has been considered. However, for a specific application such as infrared sensor applications, space applications or any other application which contains coefficient of thermal expansion mismatch problem, the entire realistic structure should be modelled. Besides warpage prediction, the thermal stresses on the structure should also be evaluated. By changing the design, for example inserting new materials with more suitable material properties or by changing the geometry of the device, thermal stress and warpage behavior can be optimized.

REFERENCES

[1] Zhang Haiyan and Lu Huajie. Analysis of thermal stress of IRFPA assembly using fem. In *Proceedings of SPIE, the International Society for Optical Engineering*, pages 68350J–1. Society of Photo-Optical Instrumentation Engineers, 2008.

[2] Wen Wu, Yonghong Wu, and Dafu Liu. Research of thermal stress between long linear MCT arrays and lead board using fem. In *Photonics Asia 2010*, pages 78471U–78471U. International Society for Optics and Photonics, 2010.

[3] Milena Vujoševic. Thermally induced deformations in die-substrate assembly. *Theoretical and Applied Mechanics*, pages 305–322, 2008.

[4] Dongfeng Geng, Kelin Zheng, and Yingjie He. Fracture analysis of InSb focal plane arrays chip under thermal shock. In *International Symposium on Optoelectronic Technology and Application 2014*, pages 93002I–93002I. International Society for Optics and Photonics, 2014.

[5] Eyup Can Baloglu, Tuba Okutucu Ozyurt, and Zafer Dursunkaya. Investigation of warpage behavior of silicon semiconductor on a silicon-adhesive-ceramic integrated structure at cryogenic temperatures. volume 2016, pages 001751–001772. International Microelectronics Assembly and Packaging Society, 2016.

[6] A. Daniels. *Field Guide to Infrared Systems*. SPIE field guides. Society of Photo Optical, 2007.

[7] G Ventura and L Risegari. *The Art of Cryogenics: Low Temperature Experimental Techniques*. Elsevier, 2008.

[8] G Walker. *Cryocoolers Part 2: Applications*. Plenum Press, 1983.

[9] Patrick J. Kelley. *Applications of Cryogenic Technology*, volume 10. Springer Science and Business Media, LCC, 1991.

[10] R Ciupa and A Rogalski. Performance limitations of photon and thermal infrared detectors. *OPTOELECTRONICS REVIEW*, pages 257–266, 1997.

[11] E. Suhir. Stresses in bimaterial thermostat. *Journal of Applied Mechanics*, 53:657–660, 1986.

[12] R Szilard. *Theories and Applications of Plate Analysis*. John Wiley and Sons Inc., 2004.

[13] E Ventsel and T Krauthammer. *Thin Plates and Shells, Theory, Analysis and Applications.* Marcel Dekker, Inc., 2001.

[14] Ming-Yi Tsai, Yi-Chieh Lin, Chen-Yu Huang, and Jenq-Dah Wu. Thermal deformations and stresses of Flip Chip BGA packages with low and high Tg underfills. *IEEE Transactions on Electronics Packaging Manufacturing*, 28:328–337, 2005.

[15] MY Tsai, CY Chiang, CY Huang, and SS Yang. Determination of residual strains of cured adhesives and their effects on warpages in electronic packaging. In *International Conference on Electronic Materials and Packaging*, pages 1–7. IEEE, 2006.

[16] Haiyan Zhang and Huajie Lu. Analysis of the thermal stress of IRFPA assembly using fem. In *Photonics Asia 2007*, pages 68350J–68350J. International Society for Optics and Photonics, 2007.

[17] Qingduan Meng, Junxian Li, Yanqiu Lv, and Weiguo Su. Structural stress analysis of 32 x 32 InSb infrared focal plane array with underfill. *Open Electrical & Electronic Engineering Journal*, 5:19–23, 2011.

[18] GZ Wang, ZN Cheng, K Becker, and J Wilde. Applying Anand model to represent the viscoelastic deformation behavior of solder alloys. *Journal of Electronic Packaging*, 123(3):247–253, 2001.

[19] Jurgen Wilde, Klaus Becker, Markus Thoben, Wolfgang Blum, Thomas Jupitz, Guozhong Wang, and Zhaonian N Cheng. Rate dependent constitutive relations based on Anand model for 92.5Pb5Sn2.5Ag solder. *IEEE Transactions on Advanced Packaging*, 23(3):408–414, 2000.

[20] Sudook Kim and Hassel Ledbetter. Low temperature elastic coefficients of polycrystalline indium. *Material Science and Engineering: A*, 252:139–143, 1998.

[21] Xing Chen, Kai He, Jian-xin Wang, and Qin-yao Zhang. Thermal cycling reliability of indirect hybrid HgCdTe infrared detectors. In *ISPDI 2013-Fifth International Symposium on Photoelectronic Detection and Imaging*, pages 890749–890749. International Society for Optics and Photonics, 2013.

[22] Xing Chen, Fengmei Dong, Kai He, Jianxin Wang, and Qingyao Zhang. Warpage and thermal stress analysis of hybrid infrared focal plane assembly. In *6th International Symposium on Advanced Optical Manufacturing and Testing Technologies (AOMATT 2012)*, pages 84191B–84191B. International Society for Optics and Photonics, 2012.

[23] P. Hariharan. *Basics of Interferometry.* Academic Press Inc., 1992.

[24] F. Trager. *Springer Handbook of Lasers and Optics.* Springer, 2012.

[25] Bongtae Han. Thermal stress in microelectronics subassemblies: Quantitative characterization using photomechanics methods. *Journal of Thermal Stresses*, 26(6):583–613, 2003.

[26] T. Yoshizawa. *Handbook of Optical Metrology, Principles and Applications*. Taylor and Francis Group, 2015.

[27] K Verma and B Han. Real time observation of thermally induced warpage of flip-chip package using FIR Fizeau interferometry. *Experimental Mechanics*, 44(6):628–633, 2004.

[28] Ming-Yi Tsai, Hsing-Yu Chang, and Michael Pecht. Warpage analysis of flip-chip PBGA packages subject to thermal loading. *IEEE Transactions on Device and Materials Reliability*, 9(3):419–424, 2009.

[29] Yinyan Wang and Patrick Hassell. On line measurement of thermally induced warpage of bgas with high sensitivity shadow moire. *International Journal of Microcircuits and Electronic Packaging*, 21:191–196, 1998.

[30] YY Wang and Patrick Hassell. Measurement of thermally induced warpage of bga packages/substrates using phase stepping shadow moire. In *Electronic Packaging Technology Conference, 1997. Proceedings of the 1997 1st*, pages 283–289. IEEE, 1997.

[31] Tsrong-Yi Wen and Shih-Chang Ku. Validation of warpage for small form factor flip-chip bga by experimental and numerical methodology. In *2008 58th Electronic Components and Technology Conference*, pages 1587–1592. IEEE, 2008.

[32] W. Greig. *Integrated Circuit Packaging, Assembly and Interconnections*. Springer, 2007.

[33] K. Varadan, K. J. Vinoy, and S. Gopalakrishnan. *Smart Material Systems and MEMS*. John Wiley and Sons Inc., 2006.

[34] M. Tilli, T. Motooka, V. Airaksinen, S. Franssila, M. Kröckel, and V. Lindroos. *Handbook of Silicon Based MEMS Materials and Technologies*. Elsevier, 2015.

[35] M Tilli, T. Motooka, V. Airaksinen, S. Franssila, M. Kröckel, and V. Lindroos. *Handbook of Silicon Based MEMS Materials and Technologies, Second Edition*. Elsevier, 2015.

[36] Y. Liu. *Power Electronic Packaging Design, Assembly Process, Reliability and Modelling*. Springer, 2012.

[37] G. Harman. *Wirebonding in Microelectronics*. The McGraw Hill Companies Inc., 2010.

[38] Shankara K. Prasad. *Advanced Wirebond Interconnection Technology*. Kluwer Academic Publishers, 2004.